Multi-Frequency GNSS/RNSS Reflectometry Receiver Design

A THESIS

SUBMITTED IN PARTIAL FULFILLMENT OF THE REQUIREMENTS FOR THE DEGREE OF

DOCTOR OF PHILOSOPHY

BY

BUSHRA ANSARI

(PHD18103)

ELECTRONICS AND COMMUNICATION ENGINEERING

INDRAPRASTHA INSTITUTE OF INFORMATION TECHNOLOGY DELHI

NEW DELHI- 110020

August 27, 2025

Dedicated to my parents, brother and coco

Thesis Certificate

This is to certify that the thesis titled **Multi-Frequency GNSS/RNSS Reflectometry Receiver Development**, submitted by **Bushra Ansari**, to the Indraprastha Institute of Information Technology (IIIT), Delhi, for the award of the degree of **Doctor of Philosophy**, is a bonafide record of the research work done by her under my supervision. The contents of this thesis, in full or in parts, have not been submitted to any other Institute or University for the award of any degree or diploma.

Sanat Kumar Biswas
Thesis Supervisor
Assistant Professor
Dept. of Electronics and Communication
IIIT Delhi, 110020

Place: New Delhi

Date: August 27, 2025

Acknowledgement

Pursuing a PhD has been an incredible journey filled with challenges, learning, and growth. It would not have been possible without the support, guidance, and encouragement of numerous individuals and institutions, to whom I owe a deep sense of gratitude.

In the first place, I would like to express my heartfelt gratitude to my supervisor, Dr. Sanat Kumar Biswas, for his trust in me and for providing me an opportunity to join him as his first PhD student. He has provided me with invaluable guidance, mentorship and support throughout my PhD journey. His deep insights into the field of space research and his unwavering enthusiasm for scientific discovery have been a constant source of inspiration. I will forever be thankful to Dr. Biswas for providing me PhD assistantship and the opportunity to attend various conferences and workshops during my PhD, which have greatly enriched my research experience. Dr. Biswas's encouragement to think critically and his patience throughout my PhD have shaped my academic and professional development.

I am equally indebted to my collaborator Dr. Debidas Kundu. He has guided me specifically in the antenna designing part, which was a very crucial part of my PhD thesis work. Without his enthusiasm and readiness to support me, it would have been impossible to carry out the field experimentation part, which is one of the important aspects of this PhD thesis. I am highly grateful to Dr. Kundu for all the enlightening discussions and his invaluable guidance.

I would also like to thank my yearly review panel members, Dr. Shobha Sundar Ram and Dr. Vivek Ashok Bohara, for their constructive feedback and valuable suggestions, which have greatly enriched my research and improved the quality of this thesis.

I am incredibly grateful to my colleagues and friends at IIIT Delhi for their encouragement, and for creating a collaborative and supportive environment. I have been fortunate to form lifelong friendships during this journey. I will always cherish the time I spend with my friends Yogesh, Kamlesh, Rajan and Kshitij, from coffee breaks to our parties celebrating my every little success in life. I am equally grateful to Ardra, Harsha, Deep Shikha, Akanksha Sneh and Rouf for their unwavering support during the hard times and for the joy they brought into my life. The countless brainstorming sessions, coffee breaks, and shared moments of joy and frustration have made this journey memorable and fulfilling.

I would like to express my gratitude to my alma mater Banasthali University, Rajasthan and BARC Mumbai, where my academic journey began and my interest in research was nurtured. These experiences laid the foundation for my passion for scientific research and motivated me to explore the research field further.

I would like to acknowledge the financial support provided by funding agencies and institutions that made this research possible. This PhD thesis work is partially supported by the Institute Research Grant, IIIT Delhi, DST-SERB Early Career Research Award (ECR/2018/001492) and the Infosys Centre of Artificial Intelligence, IIIT Delhi. Their contributions allowed me to focus on my work and explore the depths of GNSS-R. I extend my sincere gratitude to IIIT Delhi for providing me with the infrastructure and resources necessary for my research. I am deeply grateful to the faculty members, administrative staff, and technical teams for their support and assistance.

Last but not least, my deepest gratitude goes to my family, whose unwavering love and support have been my anchor throughout this journey. I am eternally thankful to my parents, Shahnaz Bano and Mohd. Yameen, who instilled in me the values of perseverance, curiosity, and hard work. I owe my decision to pursue a PhD to my brother, Mohd. Zaki, who inspired and motivated me to embark on this path. His belief in my abilities and constant encouragement have been a source of strength, helping me reach this milestone.

To all who have contributed to this journey, directly or indirectly, I offer my heartfelt thanks. This thesis is as much a result of your support as it is of my efforts.

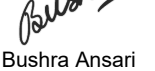

Bushra Ansari

August 27,2025

Abstract

The developments in Global Navigation Satellite Systems (GNSS) and Regional Navigation Satellite Systems(RNSS) have given rise to various application areas beyond the conventional Positioning, Navigation and Timing (PNT) services. The GNSS L-band frequency signals can be used as an inexpensive and a passive remote sensing technique called GNSS Reflectometry (GNSS-R). Several satellite mission, ground-based and spaceborne experiments have demonstrated the practicality of retrieving the Earth's geophysical parameters using the GNSS-R technique. The application of the GNSS-R technique is expanded to soil moisture estimation, vegetation cover, snow depth measurement, wind speed retrieval, and many more.

Over the last few years, the use of GNSS signals in passive bistatic or multi-static radar configurations has been researched for Earth surface remote sensing and hence capitalizing on the availability of freely accessible GNSS signals to observe various Earth-surface characteristics. The existing research on GNSS-R research is primarily focused on the use of GPS, Galileo, BeiDou and GLONASS signals. Expanding upon this foundation, the present research aims to utilize signals from the Indian Regional Navigation Satellite System (NavIC) alongside GPS-L1 signals to advance remote sensing applications. The PhD thesis is focused on developing and assessing the capability of a Software Defined Radio (SDR) based GNSS-R receiver for studying the multi-constellation and multi-frequency direct and reflected GNSS and RNSS signals for remote sensing applications. The thesis broadly addresses three research problems related to GNSS-R. Firstly, this thesis addresses the compression of large GNSS-Reflectometry (GNSS-R) datasets which is a critical step to minimize the onboard storage resources required by the payload. Secondly, this thesis explores target tracking using the GNSS-R techniques from the state estimation perspective

and the analysis of Doppler frequency bound for NavIC-L5 multipath signals. These calculations are crucial for signal acquisition and the accurate determination of reflection points, enhancing the precision of surface property measurements and other geophysical parameters derived from GNSS-R data. Lastly, this research includes the design of an antenna tailored for GNSS-R applications, as well as the development of a Software-Defined Radio (SDR)-based receiver for GNSS-R reflectometry. The commercial off-the-shelf (COTS) GNSS/RNSS receivers cannot perform the necessary computations and do not provide flexibility in customization for reflectometry as per the user's needs. Therefore, developing a custom antenna and receiver capable of processing reflected signals is essential.

This work is also a proof-of-concept of using NavIC-L5 signals for reflectometry. The proposed receiver's functionality is demonstrated through field experiments and verified using numerical simulation and a HIL simulator testbed. The field experiments are performed using the designed receiver to obtain the DDM using the GPS-L1 and NavIC-L5 signals. The field experiment results show that the proposed receiver is capable of receiving both direct (RHCP) and reflected (LHCP) GPS-L1 and NavIC-L5 RF signals and processing them into DDMs for performing reflectometry. The proposed receiver has a compact size and low power requirement and hence is suitable for performing remote sensing by using it as an air-borne or spaceborne GNSS-R receiver if radiation hardened.

Contents

List of Figures

List of Tables

List of Abbreviations

BPDN	Basis Pursuit Denoising
COTS	Commercially Off-The-Shelf
CYGNSS	Cyclone Global Navigation Satellite System
DCT	Discrete Cosine Transform
DDM	Delay Doppler Map
DWT	Discrete Wavelet Transform
ECV	Essential Climate Variable
FDM	Frequency Domain Acquisition
FFT	Fast Fourier Transform
GEO	Geostationary Orbit
GLONASS	GLObalnaya NAvigatsionnaya Sputnikovaya Sistema
GNSS	Global Navigation Satellite system
GNSS-R	GNSS-Reflectometry
GPS	Global Positioning System
GSO	Geosynchronous Orbit
HIL	Hardware-in-Loop
IGSO	Inclined Geosynchronous Orbit

LEO	Low Earth Orbit
LHCP	Left Hand Circular Polarised
LNA	Low Noise Amplifier
NavIC	NAVigation using Indian Constellation
NavIC-R	NavIC-Reflectometry
NMSE	Normalised Mean Square Error
PNT	Positioning, Navigation and Timing
PRN	Pseudo Random Number
RF	Radio Frequency
RHCP	Right Hand Circular Polarised
RNSS	Regional Navigation Satellite System
SDG	Sustainable Development Goals
SDR	Software Defined RadiO
SNR	Signal to Noise Ratio
TDS-1	TechDemo Satellite-1
UAV	Unmanned Aerial Vehicle
WAF	Woodward Ambiguity Function
QZSS	Quasi Zenith Satellite System

Chapter 1

Introduction

Contents

The advancements in Global Navigation Satellite Systems (GNSS) and Regional Navigation Satellite Systems (RNSS) have significantly expanded their applications beyond the conventional domain of Positioning, Navigation, and Timing (PNT) services. GNSS is a generalized term that encompasses both global and regional satellite constellations, which collectively provide critical PNT services for a wide range of applications. The GNSS constellation is broadly classified into global and regional systems, as shown in Fig. 1.1. The global satellite constellations include the Global Positioning System (GPS) operated by the United States, Galileo developed by the European Union, Russia's GLONASS, and China's BeiDou system. Operated by the United States, GPS is the most widely used GNSS system, with a constellation consisting of 31 operational satellites in Medium Earth Orbit (MEO). These satellites are arranged in six orbital planes to ensure continuous global coverage. Galileo is another state-of-the-art system developed by the European Union. It is designed for civilian and commercial applications, offering high-precision positioning. It currently has 24 operational satellites, with plans to expand to a total of 30 satellites, including in-orbit spares. GLONASS is the second-oldest GNSS system and serves both civilian and military users. It comprises of 24 operational satellites, distributed in three orbital planes, providing global coverage. BeiDou constellation is developed by China and it offers global coverage with a diverse satellite network comprising 35 operational satellites, including satellites in geostationary orbit (GEO), inclined geosynchronous orbit (IGSO), and MEO. These constellations are designed to provide seamless signal coverage across the globe. On the other hand, the regional satellite constellations cater to specific geographical areas and include India's Navigation with Indian Constellation (NavIC) and Japan's Quasi-Zenith Satellite System (QZSS), which are optimized for their respective regions and hence provide regional coverage only. NavIC is developed and operated by the Indian Space Research Organisation (ISRO). It consists of 7 operational satellites in GEO and IGSO, primarily providing coverage over India and surrounding regions. An expansion plan is underway to enhance its capabilities. On the other hand, QZSS is designed to enhance GPS performance in the Asia-Pacific region, particularly in Japan. It currently comprises 4 operational satellites in highly inclined geosynchronous orbits, with plans to expand to a total of 7 satellites by 2025.

The signals transmitted by GNSS satellites, primarily in the L-band frequency range [1],

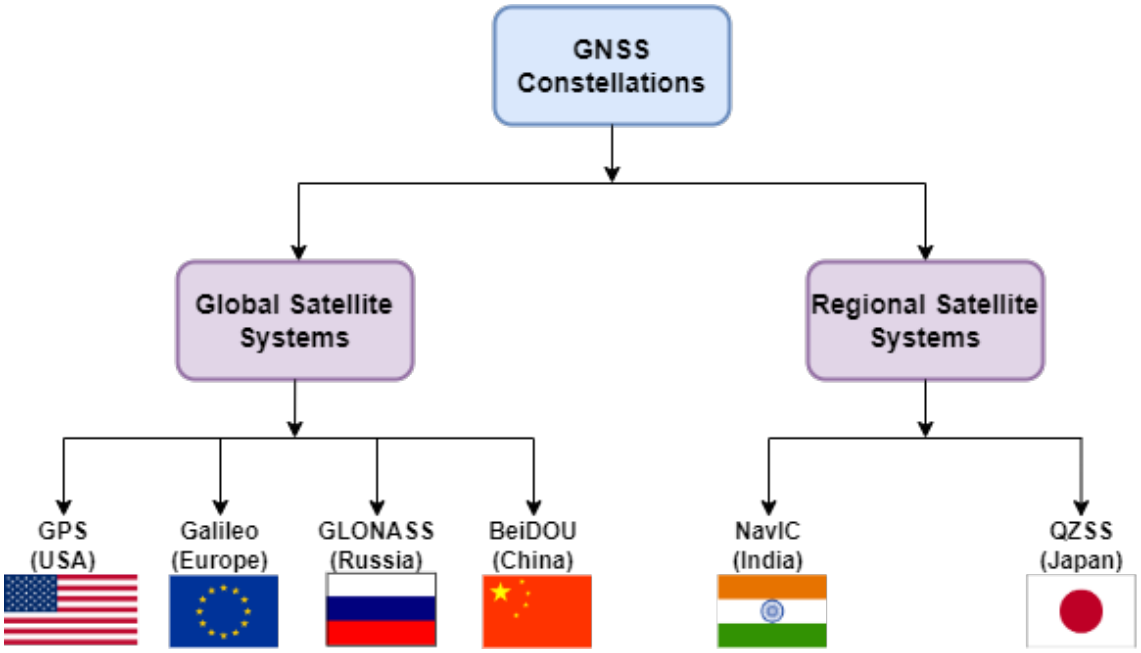

Figure 1.1: GNSS Constellations

have paved the way for innovative and cost-effective remote sensing techniques such as GNSS Reflectometry (GNSS-R) [2, 3]. GNSS-R leverages these existing navigation signals in a bistatic radar configuration, utilizing the satellite as the transmitter and a separate receiver, typically positioned on a platform such as a Low Earth Orbit (LEO) satellite [4, 5], Unmanned Aerial Vehicle (UAV) [6, 7], or drone. This passive sensing approach eliminates the need for dedicated transmitter equipment, making it a cost-effective alternative to traditional radar [8] and imaging [9] techniques that rely on active transmitter-receiver configurations. The increasing number of satellites in GNSS and RNSS constellations has resulted in enhanced signal availability, with navigation signals accessible globally [2] and continuously throughout the day. This continuous availability provides a robust foundation for leveraging GNSS signals for remote sensing applications. Over the past few decades, GNSS-R has emerged as a promising tool for Earth observation, complementing traditional remote sensing techniques and manual field measurements. The use of GNSS signals in bistatic radar configurations [10, 11] has been extensively researched for Earth surface remote sensing. Originally, GNSS-R research was primarily focused on altimetry applications [12, 13], such as measuring sea surface height. However, the scope of GNSS-R has expanded significantly, now encompassing a diverse range of applications. These include snow depth retrieval [14, 15], soil moisture estimation [16, 17], sea surface variation monitoring, wind speed [18] and direction measurement, wetland studies [19], sea-target detection [20, 21], and many others. The ability to repurpose existing GNSS

signals for remote sensing offers numerous advantages, such as cost-efficiency, global coverage, and passive operation, making it a valuable addition to Earth observation methodologies.

The GNSS-R technique has been validated through numerous airborne [22, 6] and spaceborne [23, 24] experiments, demonstrating its effectiveness in deriving geophysical parameters of the Earth's surface [25]. Traditional remote sensing techniques, such as synthetic aperture radar (SAR) and imaging systems, often involve high operational costs due to the need for dedicated transmitter systems and complex infrastructure. In contrast, GNSS-R relies solely on a receiver to capture and analyze reflected GNSS signals, leveraging the already deployed navigation satellites as transmitters. This simplicity and cost-effectiveness make GNSS-R an attractive alternative, particularly for applications requiring frequent and extensive data collection. With the proliferation of GNSS and RNSS constellations, the GNSS-R method is well-positioned to play a critical role in addressing contemporary challenges in Earth observation, including monitoring climate change, managing natural resources, and enhancing disaster response mechanisms. In conclusion, the developments in GNSS and RNSS have not only enhanced PNT services but have also unlocked innovative applications in remote sensing, such as GNSS-R. The widespread availability of navigation signals, coupled with the cost-effective and passive nature of GNSS-R, has made it a transformative tool for Earth observation. Its growing range of applications underscores its potential to complement and, in some cases, surpass traditional remote sensing techniques, solidifying its position as a pivotal technology for studying and understanding the Earth's geophysical processes.

1.1 Importance of Earth's Surface Remote Sensing

1.1.1 What is Remote Sensing?

Remote sensing is a powerful and versatile technique for acquiring data and information about a phenomenon or territory without the need for direct contact. It involves observing and measuring various characteristics of the Earth and other planetary bodies through remote sensors mounted on satellites, aircraft, or emerging platforms such as drones. These sensors detect and record reflected, emitted, or scattered energy, primarily electromagnetic radiation (EMR), from the target

of interest. Remote sensing enables the collection of high-resolution spatial and temporal data across vast areas, offering a unique perspective that is difficult to achieve through traditional in-situ observation methods. The growing adoption of drone-based remote sensing systems highlights its capability to provide high-resolution data in real time, facilitating rapid and precise monitoring of localized phenomena. At its core, remote sensing revolves around the detection and analysis of EMR across various wavelengths, including visible light, infrared, microwave, and other regions of the spectrum. This radiation carries valuable information about the physical, chemical, and biological properties of the observed object or area. For instance, vegetation health can be monitored by analysing the reflection of visible and near-infrared radiation, while thermal sensors can detect heat signatures to study land surface temperature or urban heat islands. By translating these measurements into actionable insights, remote sensing has become an indispensable tool in numerous scientific, industrial, and societal domains.

Remote sensing provides a critical alternative to in-situ [26] observation methods by offering a global perspective and the ability to monitor inaccessible or hazardous regions. Unlike traditional ground-based approaches, which can be time-consuming, costly, and limited in spatial extent, remote sensing provides comprehensive coverage that transcends geographical and political boundaries. This capability is especially valuable for applications such as disaster management, where timely and accurate data is essential for effective response and recovery. For example, satellite imagery can be used to assess flood extent, wildfire damage, or earthquake impacts, enabling authorities to allocate resources efficiently and mitigate risks. Similarly, remote sensing is widely employed in environmental monitoring to track deforestation, glacier retreat, urban expansion, and air pollution levels. The scope of remote sensing spans a wide range of disciplines, including geography, hydrology, ecology, meteorology, oceanography, geology, and agricultural sciences [27]. In geography, remote sensing is used to map land use and land cover changes, while in hydrology, it supports the monitoring of water resources, including surface water dynamics and groundwater depletion. In ecology, it aids in tracking biodiversity, habitat loss, and ecosystem health. Meteorological applications include weather prediction and climate monitoring, while oceanography benefits from remote sensing techniques to study sea surface temperature, ocean currents, and marine ecosystems. In geology, it is used for mineral exploration, seismic risk assessment, and

mapping geological structures. One of the most significant advantages of remote sensing lies in its ability to provide timely, accurate, and cost-effective information, which is critical for informed decision-making in various fields. By offering a synoptic view of the Earth's surface and beyond, remote sensing facilitates large-scale monitoring, assessment, and management of natural and anthropogenic systems. For instance, agricultural monitoring using remote sensing allows farmers to optimize crop yields by assessing soil moisture, nutrient content, and plant health. Similarly, urban planners rely on remote sensing data to analyse urban growth patterns, manage infrastructure, and plan sustainable development.

The societal impact of remote sensing is profound, as it supports scientific research, policy formulation, and sustainable development goals. For instance, remote sensing plays a key role in climate change research by monitoring carbon emissions, greenhouse gas concentrations, and the impacts of global warming on ecosystems. It also fosters innovation by enabling the development of advanced algorithms, machine-learning techniques, and geospatial technologies for data processing and analysis. Furthermore, remote sensing promotes international collaboration by providing a shared platform for addressing global challenges, such as disaster risk reduction, food security, and environmental conservation. In conclusion, remote sensing is a transformative technology that has revolutionized the way we observe, understand, and manage the Earth and its resources. Its ability to collect high-resolution, multi-spectral, and real-time data over vast areas makes it an indispensable tool for scientific research, policy-making, and societal progress. As advancements in sensor technology, data processing, and analytical methods continue to evolve, remote sensing will play an even more pivotal role in addressing emerging global challenges and fostering a sustainable future.

1.1.2 Importance of Space-based Remote sensing

Climate change is an urgent and long-term challenge that humanity faces, demanding immediate attention and innovative solutions. Space technology, particularly Earth observation systems, plays a pivotal role in comprehending and addressing this global crisis [28, 29]. These technologies have enabled a more precise understanding of climate change and its underlying drivers, while also

fostering innovations that benefit the environment and help mitigate its impacts. Satellite-based data has become a cornerstone for studying global climate change trends, which are worsening at an alarming rate. This data provides invaluable insights into Essential Climate Variables (ECVs) [30], which encompass atmospheric, land, and oceanic parameters that exhibit spatial and temporal variations. By monitoring these ECVs, scientists can gain a deeper understanding of the dynamics driving climate change and its cascading effects on ecosystems and human societies. Earth observation and meteorological data are indispensable for analyzing and monitoring climate change, as well as for developing predictive models and actionable strategies. With advancements in imaging and microwave remote sensing technologies [31, 32, 33], a wealth of satellite data is now available to monitor key indicators of climate change. These datasets offer detailed, frequent, and global coverage, enabling a more comprehensive analysis of soil conditions, crop health, water resources, land use, and climate patterns. Such insights are vital for evidence-based decision-making in critical sectors like agriculture, forestry, marine studies, and urban planning. Additionally, satellite observations [34] facilitate better understanding of shifting weather patterns and provide early warnings for natural disasters such as floods, droughts, tsunamis [35] and cyclones [36], helping communities prepare and respond effectively.

Traditional ground-based observation methods and emerging remote-sensing technologies both contribute to climate change research. However, ground-based observations are often limited by their point-based nature and sparse spatial coverage, restricting their ability to provide a holistic view of the Earth's changing climate. In contrast, spaceborne remote sensing, including GNSS-Reflectometry (GNSS-R), offers significant advantages. Spaceborne GNSS-R provides wide-area coverage and the ability to monitor medium- and large-scale phenomena such as ocean eddies, hurricanes, and tsunamis. Unlike ground-based systems that collect data at fixed intervals, satellite systems enable continuous, global-scale monitoring, significantly enhancing the understanding of climate processes and their interactions. Despite these advancements, satellite data is not without limitations. Sensor biases, retrieval algorithm errors, and inconsistencies across different satellite missions can introduce uncertainties in the data. These challenges underscore the need for continuous improvement in data processing techniques and calibration methods. Nonetheless, satellite remote sensing has revolutionized climate science by enabling the quantification of spatio-temporal

changes in the atmosphere, land, and oceans. This has provided a critical foundation for studying climate change and developing adaptive measures to address its impacts, ensuring that society can respond more effectively to this pressing global issue.

1.2 Various Remote Sensing Technique

Over the years, remote sensing technology has evolved into a critical tool for scientific exploration and practical applications across diverse fields such as agriculture, meteorology, environmental monitoring, disaster management, and urban planning. By providing high-resolution spatial and temporal data, remote sensing has enabled more precise analysis and decision-making in these domains. Advanced satellite missions, such as RADARSAT [37], TerraSAR-X [38], SRTM, EOSDA, ERS, Sentinel [39], and LANDSAT [40], have been pivotal in generating reliable datasets for Earth observation. These missions have contributed significantly to a wide range of applications, including crop health monitoring, climate modeling, biodiversity conservation, and mapping land-use changes. For instance, LANDSAT data has been instrumental in detecting deforestation trends, while TerraSAR-X and RADARSAT provide high-resolution radar imagery for applications like flood mapping and ice monitoring in polar regions.

Remote sensing techniques can be broadly categorized into three approaches [41]: active, passive, and bistatic. Each of these techniques offers unique capabilities and serves specific scientific and practical applications. Active remote sensing systems, such as synthetic aperture radar (SAR), emit their own electromagnetic signals and measure the reflected energy from the Earth's surface. Passive remote sensing systems, on the other hand, rely on natural sources of radiation, such as sunlight, to detect reflected or emitted energy from the Earth's surface. Bistatic remote sensing is a relatively newer approach that involves using separate transmitter and receiver systems, which may be located on different platforms. This technique is particularly advantageous for applications requiring high sensitivity to surface properties and scattering characteristics. The basic idea of these three remote sensing techniques is shown in Fig. 3.1 and is explained in detail in the next section.

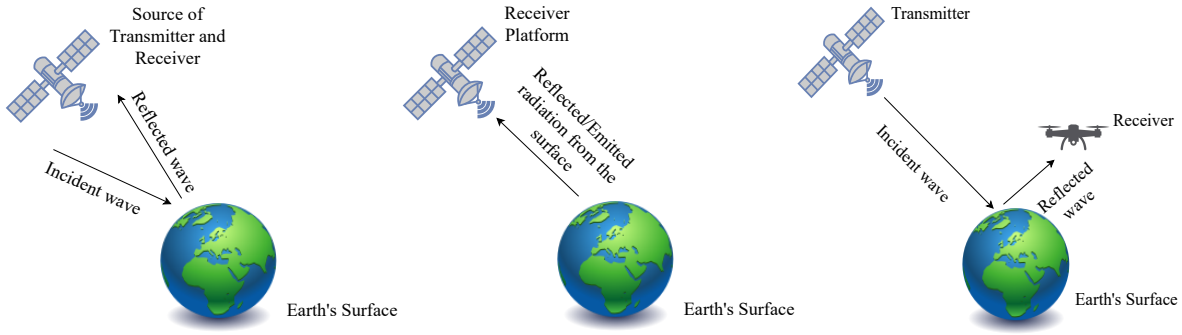

(a) Active (b) Passive (c) Bistatic

Figure 1.2: Different remote sensing technique

1.2.1 Active Remote Sensing

Active remote sensing is a powerful and versatile remote sensing technique in which sensors actively emit their own energy towards a target and measure the energy reflected or backscattered from it. This method, as illustrated in Fig. 1.2a, differs significantly from passive remote sensing, which relies on naturally occurring energy sources such as sunlight. Active remote sensing operates independently of natural light conditions, making it highly effective for data collection during the day or night. This capability makes active sensors invaluable in environments with low visibility or limited natural illumination, such as polar regions or during nighttime operations. Active sensors encompass a range of advanced technologies, including radar systems, laser altimeters, and scatterometers, each tailored for specific applications and offering unique capabilities.

Radar (Radio Detection and Ranging) is one of the most widely used active remote sensing technologies. It operates by emitting radio frequency signals toward a target and measuring the time delay and strength of the returned signal. By analyzing these parameters, radar can determine the range, location, and motion of objects with high precision. Radar systems are particularly useful for mapping terrain, monitoring land deformation, and detecting moving objects such as vehicles or ships. Synthetic Aperture Radar (SAR), an advanced form of radar, provides high-resolution imaging capabilities and is extensively used for Earth observation, disaster management, and environmental monitoring. Laser altimeters are another important type of active remote-sensing sensor. These instruments emit laser pulses and measure the time taken for the light to travel to a target and back. Laser altimeters are frequently used in topographic mapping, glacier

and ice sheet monitoring, and vegetation canopy height estimation. For example, NASA's ICESat missions use laser altimetry to monitor changes in polar ice thickness, contributing to a better understanding of climate change and its impacts. Scatterometers, on the other hand, are active sensors designed to measure the backscattered radiation from a target. These sensors are primarily used to analyze surface roughness and monitor ocean surface winds.

The significant advantage of active sensors is their resilience to adverse weather conditions. Many active remote sensing systems, particularly radar, can penetrate through clouds, rain, and fog, enabling data collection even in challenging atmospheric conditions. Active remote sensing has a wide range of applications across various domains. In agriculture and forestry, active sensors provide vital data for managing crops, forests, and remote or difficult-to-access areas.

1.2.2 Passive Sensors

Passive remote sensing sensors operate by detecting the natural electromagnetic radiation emitted or reflected by the Earth's surface, as illustrated in Fig. 1.2b. Unlike active sensors, passive sensors do not emit their own energy but instead rely on external sources, such as sunlight or thermal radiation, to gather information about the target. These sensors are designed to measure radiation across specific wavelengths, including visible, infrared (IR), and microwave regions of the spectrum, enabling the study of various geophysical properties of the Earth's surface. A prominent technology in passive remote sensing is the radiometer, which measures the intensity of radiation emitted or reflected by a target within particular spectral bands. Radiometers are broadly categorized into two types: hyperspectral radiometers and imaging radiometers. Hyperspectral radiometers operate with high spectral resolution, capturing data across numerous narrow and contiguous spectral bands. This detailed spectral information allows for the precise identification and analysis of a target's composition, properties, and condition. In contrast, imaging radiometers are designed to scan surfaces and generate images based on the intensity of the radiation detected. These images provide spatial information about the distribution and variation of surface properties over large areas. Imaging radiometers are commonly used in weather monitoring, land use mapping, and environmental surveillance.

Passive remote sensing sensors offer several advantages that make them indispensable for environmental monitoring and scientific research. By capturing data across the visible, infrared, and microwave spectra, passive sensors enable the study of a wide array of natural phenomena, including vegetation health, land surface changes, and atmospheric conditions. For instance, the Normalized Difference Vegetation Index (NDVI), a widely used metric derived from passive remote sensing data, is used to assess plant health and monitor agricultural productivity. Another significant advantage of passive remote sensing is its ability to operate without the need for active energy emission, which reduces operational complexity and energy requirements. This makes passive sensors ideal for long-term monitoring missions on satellites, where energy efficiency is a critical consideration. Additionally, passive sensors are often less expensive to develop and deploy compared to active systems, making them a cost-effective solution for large-scale environmental monitoring.

1.2.3 Bistatic Remote Sensing Sensors

Bistatic remote sensing [42] is a powerful remote sensing technique that leverages the principle of bistatic radar. In this configuration, the transmitter and receiver are located on two separate platforms, as opposed to monostatic radar systems where both components are co-located. A basic bistatic remote sensing technique [42, 43, 44, 45] is shown in Fig. 1.2c. In the context of bistatic remote sensing, navigation satellites such as GPS, Galileo, GLONASS, NavIC, and BeiDou act as transmitters. These satellites continuously broadcast radio-frequency signals across the Earth, primarily intended for Positioning, Navigation, and Timing (PNT) services. However, these signals can also interact with the Earth's surface, where they are scattered, reflected, or absorbed. A receiver located on a separate platform, such as an aircraft, drone, or Low Earth Orbit (LEO) satellite, captures both the direct signal (transmitted from the satellite to the receiver) and the reflected signal (transmitted from the satellite and scattered by the Earth's surface before reaching the receiver). The fundamental principle of bistatic remote sensing is to analyze the differences between the direct and reflected signals to extract meaningful information about the reflecting surface. These differences are assessed in terms of amplitude, phase, polarization, and time delay, all of which provide insights about the physical and electromagnetic properties of the surface.

Specifically, bistatic remote sensing techniques enable the estimation of critical surface parameters, such as: Surface Permittivity, Surface Roughness and Reflectivity and Scattering Coefficients.

The technique of GNSS-Reflectometry (GNSS-R) is a practical application of bistatic remote sensing. GNSS-R utilizes signals from Global Navigation Satellite Systems (GNSS) for passive bistatic remote sensing. This approach capitalizes on the continuous and global availability of GNSS signals, making it a cost-effective and efficient remote sensing method. Since GNSS satellites are already operational and transmitting signals, the only additional component required is the development and deployment of a GNSS-R receiver, which simplifies the system and reduces costs. GNSS-R systems operate by capturing both direct signals and signals reflected from the Earth's surface. The direct signal acts as a reference, while the reflected signal contains information about the surface it interacted with. By comparing the two signals, GNSS-R systems can derive various geophysical parameters of the surface. One of the key advantages of GNSS-R is its ability to provide 24-hour coverage. GNSS satellites transmit signals continuously, ensuring round-the-clock availability for remote sensing. This capability is particularly beneficial for monitoring dynamic and time-sensitive phenomena, such as ocean waves, river flow, or snowmelt. Additionally, GNSS satellites operate on multiple frequency bands, such as L1, L2, and L5, which enhance the signal penetration capability and improve spatial resolution. The applications of bistatic remote sensing, particularly GNSS-R, are diverse and span multiple scientific and operational fields including: Oceanography, Hydrology, Forestry and Vegetation Studies, Surface Altimetry, and Disaster Monitoring. A more detailed exploration of the GNSS-R technique, including its underlying principles, signal processing methods, and application case studies, is presented in Chapter 2.

Hence, we see that the diverse range of remote sensing technologies, from active sensors like radar and LiDAR to passive sensors such as radiometers and spectrometers and bistatic remote sensing techniques, provides a robust toolkit for collecting and analyzing data from the Earth's surface. These technologies enable a broad spectrum of applications, from agricultural management and environmental monitoring to disaster response and scientific research, each offering unique advantages based on the specific requirements of the observation and analysis tasks.

1.3 Motivation and Objectives

Global Navigation Satellite Systems (GNSS) and Regional Navigation Satellite Systems (RNSS) play a pivotal role in providing positioning, navigation, and timing (PNT) services, with their applications now extending far beyond traditional domains into innovative fields such as Earth observation through GNSS-Reflectometry (GNSS-R) [46]. GNSS-R leverages signals reflected from the Earth's surface to derive critical information about environmental parameters, including soil moisture, sea state, and vegetation health. Currently, most GNSS-R systems are developed using signals from the Global Positioning System (GPS) [47, 48], Galileo [49, 50], GLONASS [51], and BeiDou [52, 53] satellite constellations. However, this research focuses on exploiting the Indian Regional Navigation Satellite System (NavIC) and GPS-L1 signals for advanced remote sensing applications. NavIC, being a regional system with enhanced signal availability over the Indian subcontinent, holds immense potential for localized GNSS-R applications, especially in agriculture, environmental monitoring, and disaster management.

Compared to GPS and Galileo, which offer global coverage, NavIC is specifically designed for regional performance, and this regional optimization brings distinct advantages for GNSS-R use in the Indian region. NavIC offers higher satellite visibility and signal strength over India due to its orbital configuration, where geostationary and inclined geosynchronous satellites are positioned to maximize elevation and coverage over the subcontinent.

Existing research in NavIC-based reflectometry primarily involves the analysis of multi-path signals acquired using commercial NavIC navigation receivers [54]. However, such commercial off-the-shelf (COTS) receivers lack the flexibility to perform advanced computations or customize signal processing as per user requirements, thereby limiting their scope for research-driven applications. To address these limitations, this study proposes the development of a custom-designed receiver tailored for GNSS-R applications. The primary objective is to design and implement a Software-Defined Receiver (SDR)-based NavIC-Reflectometry (NavIC-R) system capable of real-time data acquisition and processing. The proposed system will receive both the direct Right-Hand Circularly Polarized (RHCP) signals and the reflected Left-Hand Circularly Polarized (LHCP) signals from NavIC-L5 and GPS-L1 satellites. It will process these signals to generate Delay-Doppler

Maps (DDMs), which are crucial for analyzing reflected signal power as a function of the reflecting surface properties. These DDMs will provide valuable insights into surface parameters, enabling applications such as soil moisture estimation and sea-state observations. Furthermore, the research delves into the detailed analysis of DDMs for both direct and reflected GNSS signals, with a focus on using these outputs for GNSS-R applications. The ultimate goal is to establish a robust system that facilitates real-time monitoring and on-demand estimation of essential climate variables. This capability will enable more efficient agricultural management, enhanced climate studies, and comprehensive environmental monitoring. By harnessing the potential of NavIC for advanced GNSS-R applications, this research aims to push the boundaries of regional reflectometry and establish NavIC as a critical tool in remote sensing.

Beyond the scientific and technical contributions, this research also aligns with broader global objectives. It supports the United Nations' Sustainable Development Goals (SDGs), specifically SDG-12, which emphasizes sustainable agriculture and natural resource management, and SDG-13, which advocates for urgent action to combat climate change and mitigate its impacts. Through the development of specialized receivers and processing techniques, this work not only addresses critical environmental challenges but also contributes to global efforts in achieving sustainable and resilient ecosystems. This research highlights the transformative potential of NavIC in advancing GNSS-R applications and sets the stage for its future role in supporting global climate resilience initiatives.

1.4 Contributions

This dissertation makes several novel contributions, which are highlighted below, along with their respective research objectives and significance:

1. **Compression of GNSS Reflectometry Data for Transmission:** The objective is to develop an algorithm to compress the large volume of GNSS-R data for efficient storage onboard and transmission. The GNSS-R data, even for short durations, can be extremely large (e.g., 100,000 samples in 2 minutes 20 seconds). Large data size makes wireless transmission

time-consuming and impractical for real-time applications. Compression reduces the data size, facilitating faster transmission and processing in GNSS-R applications. The proposed algorithm is designed to compress GNSS datasets while preserving the essential information needed for accurate reflectometry analysis. The proposed algorithm is implemented on both GPS-L1 and NavIC-L5 signals to illustrate its adaptability on different datasets.

2. **Target localisation using GNSS-R and Doppler Frequency Bound for NavIC-L5 Multipath Signals:** This work examines the utility of GNSS-R based observations for target localisation, using the difference between the direct path length and the multipath range obtained from the multiple GNSS transmitters and a single receiver as a set of key observations. The four sets of bistatic ranges are optimised using the least square estimation technique in order to estimate the target location. Also, efficient signal acquisition is crucial for both PNT and remote sensing applications. This work also performs a grid-based analysis to calculate Doppler frequencies for various surface target points within the NavIC service region, leading to a significant reduction in signal acquisition time for the NavIC-L5 multipath signal.

3. **Antenna Design for Receiving Multi-Constellation GNSS RF Signals:** The design and development of an antenna capable of receiving multi-constellation GNSS RF signals, including direct Right-Hand Circularly Polarized (RHCP) and Earth-reflected Left-Hand Circularly Polarized (LHCP) signals is proposed in this work. Traditional GNSS antennas are optimized for navigation and positioning applications, focusing on receiving RHCP signals from satellites while actively rejecting LHCP signals to minimize the effects of multipath interference. However, GNSS-R applications rely on the reception of Earth-reflected LHCP signals to study surface properties and environmental phenomena. Therefore, designing an antenna specifically tailored for GNSS-R is essential to ensure it can efficiently receive both RHCP signals for reference and LHCP signals for reflectometry. Additionally, the proposed antenna is compact, lightweight and suitable for deployment of various platforms, including UAVs, aircraft and satellites, if radiation-hardened.

4. **SDR-Based Reflectometry Receiver Design for GNSS-R Applications:** Proposed a GNSS-R receiver that leverages a Software-Defined Radio (SDR) platform integrated with

a Raspberry Pi single-board computer as the primary processing unit. The proposed design focuses on efficiently processing Earth-reflected GNSS signals directly on board, enabling its deployment on a variety of platforms, such as Unmanned Aerial Vehicles (UAVs) and Low Earth Orbit (LEO) satellites. One of the key features of this receiver is its ability to support multi-constellation and multi-frequency GNSS signals. The SDR-based architecture offers flexibility and adaptability, allowing for the implementation of customized algorithms for real-time data acquisition and signal processing tailored to specific remote sensing objectives. The integration of advanced signal processing capabilities with the flexibility of SDR technology ensures that this receiver is a scalable and future-ready solution for GNSS-R applications in both terrestrial and spaceborne environments.

Each of these contributions addresses a critical challenge in GNSS Reflectometry, advancing the field and enhancing the practical application of GNSS-R for Earth observation and related technologies.

1.5 Structure of Thesis

The thesis is structured into six chapters, each addressing specific aspects of the research.

Chapter 1 provides the basic foundational introduction to the thesis topic. The motivation and the research objectives of the thesis are outlined in this chapter. The major contributions of the thesis, as well as a list of publications and presentations associated with the research, are provided in this chapter.

Chapter 2 initially explains the fundamentals of the GNSS-R technique along with some of the major applications of GNSS-R, including altimetry measurement, soil moisture and snow height estimation, wetland studies and target localisation using GNSS-R. Building on this foundational understanding, the chapter transitions into a detailed explanation of the theoretical and signal-processing concepts that underpin GNSS-R. Further, this chapter provides a detailed explanation of the theoretical and signal processing concepts, including DDM generation and GNSS signal acquisition, which are commonly used in the GNSS-R.

Chapter 3 addresses the challenges associated with managing large datasets for GNSS-Reflectometry applications. It presents a technique and algorithm for GNSS data compression used while handling large datasets for GNSS-Reflectometry applications. The proposed algorithm aims to reduce the size of GNSS datasets without compromising the integrity of the information required for reflectometry analysis. The algorithm for GNSS data compression and reconstruction on the receiver side is presented in this chapter. The feasibility of this algorithm is evaluated on both the GPS-L1 and NavIC-L5 signals. Metrics such as compression ratio, reconstruction accuracy, and computational efficiency are analyzed, highlighting the algorithm's potential to balance data reduction and fidelity. Comparative results for GPS-L1 and NavIC-L5 signals illustrate the algorithm's adaptability to diverse signal characteristics and its ability to handle varying levels of signal complexity.

Chapter 4 delves into the concept of static target localisation using GNSS-Reflectometry (GNSS-R) and explores the critical role of Doppler frequency-bound calculations for NavIC-L5 signals. In addition to static target localisation and Doppler calculations, the chapter underscores the importance of optimizing the signal acquisition time in GNSS-R systems. A shorter acquisition time not only reduces computational overhead but also enables faster initialization of the GNSS-R system, which is particularly beneficial for real-time applications.

Chapter 5 details the design, development, and testing of key hardware components for GNSS-Reflectometry (GNSS-R) applications, specifically focusing on a multi-frequency GNSS antenna and an SDR-based multi-constellation GNSS-R receiver. These components form the backbone of a sophisticated GNSS-R system capable of acquiring and processing both direct and reflected GNSS RF signals from multiple satellite constellations. The development of the multi-frequency GNSS antenna is discussed in detail, highlighting its unique capability to simultaneously receive signals across multiple GNSS frequency bands, such as GPS-L1 and NavIC-L5. Building upon the antenna development, the chapter presents the design of an SDR (Software-Defined Radio)-based multi-constellation GNSS-R receiver. This receiver leverages the flexibility of SDR technology to support real-time signal acquisition, processing, and analysis across multiple GNSS constellations and frequency bands. The use of SDR technology allows for easy customization and scalability, making it adaptable to evolving GNSS standards and emerging applications.

To validate the performance of the developed GNSS-R system, the chapter presents the results of rigorous testing conducted using a hardware-in-loop (HIL) simulator testbed. The HIL setup replicates real-world GNSS signal conditions, enabling controlled experiments to evaluate the system's sensitivity, accuracy, and robustness. In addition to simulator-based testing, the chapter presents findings from field experiments. The field results highlight the multi-frequency antenna's ability to capture both direct and reflected signals simultaneously, and the SDR-based receiver's proficiency in processing these signals to generate accurate Delay-Doppler Maps (DDMs) and extract meaningful parameters for GNSS-R applications. In summary, this chapter showcases the development and testing of a comprehensive GNSS-R hardware system, integrating a multi-frequency GNSS antenna and an SDR-based multi-constellation receiver.

Chapter 6 concludes this dissertation and states the contributions made during this thesis to the advancement of multi-constellation GNSS-R. Following this, suggestions are made for future research into areas covered by this research.

The pictorial representation of the thesis is shown in Fig. 1.3.

1.6 List of Publications and Presentation

1.6.1 Publications

1. Bushra Ansari, and Sanat K. Biswas. "Target Localisation using GNSS-R and Doppler Bound Estimation for NavIC -L5 Reflected Signal: A Simulation-Based Approach". in Advances in Space Research (Under Review)

2. B. Ansari, D. Kundu, and S.K. Biswas, "A multi-frequency GPS and NavIC reflectometry receiver using commercially off-the-shelf SDR". GPS Solut 29, 29 (2025).

3. B. Ansari and S. K. Biswas, "Multi-Frequency GNSS-R Receiver using BladeRF SDR and Single-Board Computer", 2024 4th URSI Atlantic Radio Science Meeting (AT-RASC), Meloneras, Spain, 2024

4. B. Ansari and S. K. Biswas, "A Hardware-In-Loop simulation Test-bed for NavIC Reflec-

tometry Experiments," in 2021 XXXIVth General Assembly and Scientific Symposium of the International Union of Radio Science (URSI GASS), 2021, pp. 1–3.

5. B. Ansari, V. Kaushik, and S. K. Biswas, "Raw GNSS Data Compression using Compressive Sensing for Reflectometry Applications," in 2020 33rd General Assembly and Scientific Symposium of the International Union of Radio Science, URSI GASS 2020. Institute of Electrical and Electronics Engineers Inc., 8 2020.

1.6.2 Presentations

1. Invited to present my research work on "NavIC-Reflectometry Receiver Development for Remote Sensing Applications" at United Nations/Finland Workshop on the Applications of GNSS, 23 – 26 October 2023, Helsinki, Finland, organized by the UN Office of Outer Space Affairs (UNOOSA).

2. Presented "GNSS-Reflectometry using NavIC-L5 signals for Earth Observation" at National Space Science Symposium 2022, organised by Indian Institute of Science Education and Research, Kolkata.

3. Presented "High-Resolution Satellite-Based Land Surface Monitoring Using NavIC L5 Signal" at the UN/AUSTRIA SYMPOSIUM: "SPACE APPLICATIONS FOR FOOD SYSTEMS" in 2021, organized by the UN Office of Outer Space Affairs (UNOOSA).

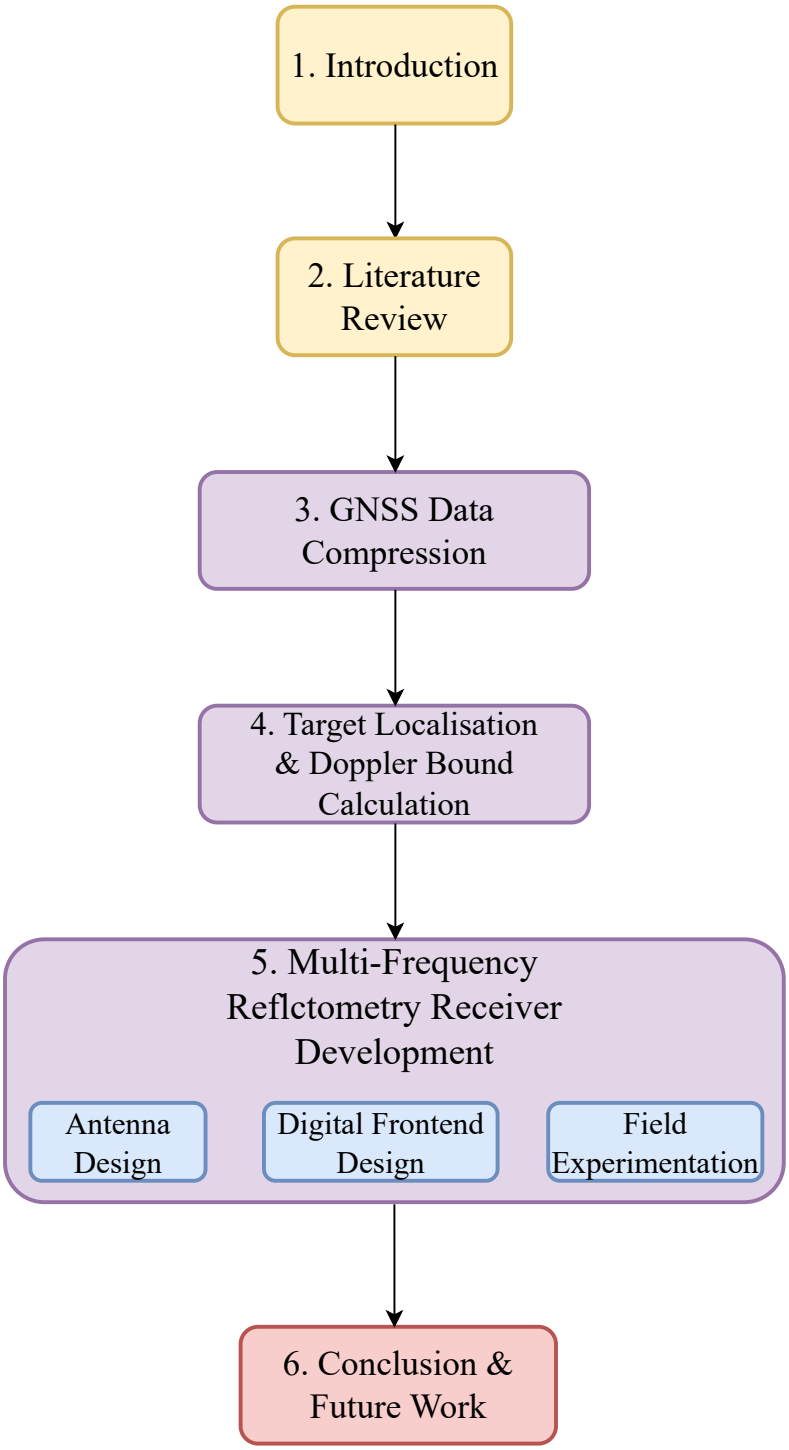

Figure 1.3: Structure of Thesis

Chapter 2

Literature Review

Contents

The chapter begins by providing a comprehensive overview of the fundamentals of the GNSS-Reflectometry (GNSS-R) technique, emphasizing its versatility and wide range of applications in remote sensing. The chapter elaborates on how GNSS-R has emerged as a cost-effective and innovative solution for Earth observation, owing to the global availability of GNSS signals, their wide coverage, and the passive nature of the technique. Based on basic understanding, the chapter transitions into a detailed explanation of the theoretical and signal processing concepts of GNSS-R. A key concept introduced is the Delay-Doppler Map (DDM) generation. Through this comprehensive exploration of GNSS-R fundamentals, applications, and signal processing concepts, the chapter provides a solid foundation for understanding the technique's potential and its implementation in real-world scenarios.

2.1 What is GNSS-R: A brief overview

When computing a navigation solution, GNSS reflected signals are conventionally considered multipath signals or contributors to the error vector. The concept of using GNSS reflected signals as signals of opportunity to perform reflectometry and scatterometry was first proposed in 1988 [55]and then for mesoscale ocean altimetry in 1993 [13]. GNSS-Reflectometry (GNSS-R) has rapidly evolved as a transformative remote sensing technology that leverages the unique properties of GNSS signals for Earth observation. Unlike traditional monostatic radar systems, which require both a transmitter and receiver, GNSS-R uses the already existing GNSS constellations as transmitters, significantly reducing the cost and complexity of deployment. With the rise of satellite-based navigation systems like Global (GNSS), Regional (RNSS), and satellite-based augmentation systems, there has been an exponential increase in the number of satellites transmitting GNSS signals, therefore providing more simultaneous observations.

This passive bistatic radar configuration enables GNSS-R to simultaneously track multiple reflections from the Earth's surface, offering enhanced spatial and temporal resolution compared to conventional nadir-looking monostatic altimeters. The reflected GNSS signals carry information about the geophysical characteristics of the surface, which can be extracted through advanced signal processing techniques. For instance, the Delay-Doppler Map (DDM) is a key data product

generated by GNSS-R receivers, providing detailed insights into the time delay and Doppler shift of reflected signals. DDM enables precise characterization of surface parameters, such as roughness, permittivity, and scattering properties.

Recent advancements in GNSS-R technology have focused on improving the accuracy and reliability of surface parameter retrievals. The GNSS transmitting satellites include the USA's GPS, China's BDS, the European Union's Galileo, and Russia's GLONASS, which offer real-time, all-weather, any-time, anywhere and high-precision observations by transmitting L-band signals continuously, which have been widely used for positioning, navigation and timing. The GNSS-R receiver can be placed either on board a UAV, Aircraft or LEO satellite. The receiving platforms that are typically used for GNSS-R are shown in Fig. 2.1. Fig. 2.1 depicts how the GNSS signals transmitted from already existing navigation satellites can be received on board various receiving platforms, including UAV, aircraft and LEO satellites. Multi-frequency GNSS-R systems, for example, exploit signals across different GNSS bands, such as L1, L2, and L5, to enhance penetration capabilities and improve the sensitivity to various surface types. Furthermore, advanced algorithms, such as machine learning and deep learning techniques, are increasingly being utilized to process GNSS-R data, enabling more robust estimation of geophysical parameters and better handling of noise and interference.

The main difference between a GNSS-R receiver and a typical GNSS receiver is that the former contains hardware and software to generate a Delay-Doppler map, which contains the key observation data for airborne and spaceborne GNSS-R technology. Thus, a GNSS-R receiver may be considered an extension of a typical GNSS receiver. GNSS-R receivers detect direct and reflected signals and analyze the received signal properties to estimate the geophysical information of the reflecting surface. The reflected GNSS signals vary from direct signals in terms of time delay, Doppler shift, signal power and polarization. Observations such as signal-to-noise ratio (SNR) [56], carrier phase and pseudo-range provided by typical GNSS receivers can be used as GNSS-R data to measure geophysical parameters. The properties of reflected signals depend on various geophysical parameters such as surface roughness, moisture and vegetation. GNSS-R applications have expanded from traditional altimetry [57, 58] to include a wide range of geophysical studies. From the formerly suggested applications (altimetry [57, 58] and wind speed [59, 60]), others have

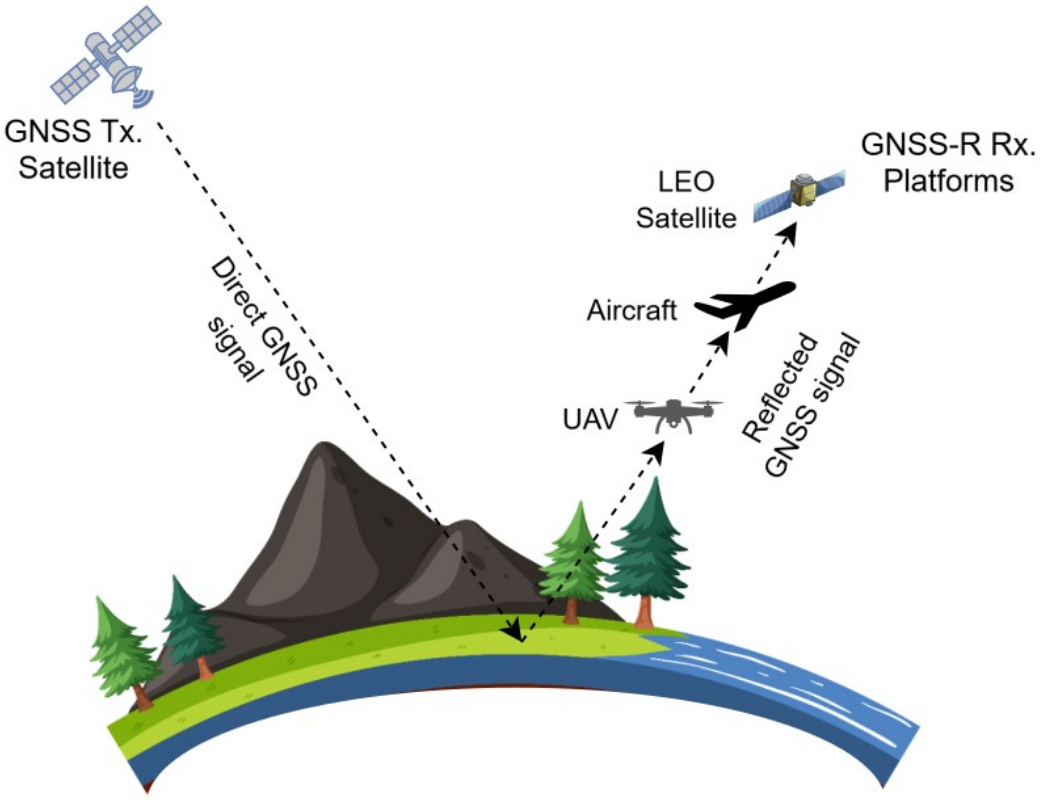

Figure 2.1: GNSS-R Rx. Platforms

also been proposed including soil moisture [61, 62], wind speed [44, 63], snow depth [64, 65], sea state [66, 67] and vegetation height and cover [68, 69]. Emerging research is exploring the potential of GNSS-R for monitoring dynamic phenomena such as floods, landslides, and vegetation growth, demonstrating its versatility in addressing real-time environmental challenges. Additionally, the fusion of GNSS-R data with other remote sensing modalities, such as synthetic aperture radar (SAR) and optical sensors, is being investigated to provide complementary datasets for more comprehensive Earth system analyses.

Similar to other major remote sensing technologies, there have been about 10 satellite missions with a payload for GNSS-R applications or a main focus on specific GNSS-R applications. The UK-DMC (Disaster Monitoring Constellation) satellite [4, 70] is the first GNSS-R related satellite which was built by Surrey Satellite Technology Ltd. (SSTL). It carried four major payloads, and one of them was designed to conduct an experiment to demonstrate the potential application of GNSS-R. The UK-DMC satellite was launched on 27 September 2003. On 8 July 2014, the UK launched the TechDemoSat-1 (TDS-1) satellite, which carried the SGR-RESI (Space GNSS

Receiver-Remote Sensing Instrument), which was also developed by SSTL. Over the period of four years, TDS-1 has recorded a large number of data, which has been widely used for studies in science and technology. The TDS-1 satellite was retired from service in December 2018. Following TDS-1, on 15 December 2016, NASA launched eight micro-satellites to monitor tropical cyclones with the initial main objective of enhancing the accuracy of the measurement and prediction of hurricane intensity [71, 72]. The constellation is termed cyclone GNSS (CYGNSS) [73, 74]. This project has been led by the University of Michigan. CYGNSS has also produced a large number of data, which have been used to retrieve various ocean and land parameters. On 14 July 2017, microsatellite WNISAT-1R was launched, developed by Weather news Inc. in Japan. A WNISAT-IR payload is a GNSS-R receiver that has received GNSS signals and generated delay–Doppler maps. The Spire Global Inc. [5, 75] GNSS-RO CubeSats has also been providing altimetric observations from surfaces that reflect coherently at the L-band since 2019. In 2019 and 2020, the company launched two batches of two 3U CubeSats with GNSS-R capabilities (two in 2019, two in 2020). The miniaturized receiver weighing less than 5 kg, produced by Spire, is the outcome of years of working with GNSS-RO receivers, and it provides a multi-constellation (GPS, QZSS, Galileo) capability. The instrument is able to operate continuously with deployable solar panels. It is currently collecting LHCP measurements at near-nadir and RHCP measurements at grazing angles, combining their GNSS-R and GNSS-RO satellites.

Another mission is by UPC NanoSat-Lab, which leads the European Space Agency (ESA) FSSCat mission. The mission was launched in September 2020, and included a combined GNSS-R receiver and an L-band radiometer using software-defined radio technology (SDR) [76]. Additionally, Passive REflecTomeTry and dosimetrY (PRETTY) satellite [77, 31] by ESA for GNSS-R altimetry was launched in October 2023. Another upcoming GNSS-R mission named Hydrological Global Navigation Satellite System (HydroGNSS) [33, 78] by ESA is planned to be launched in 2025. The major spaceborne GNSS-R missions are summarised in Table 2.1.

Despite the significant contributions of these missions, several critical limitations and research gaps remain, particularly in the context of regional applications, lightweight platform integration, and signal diversity:

Table 2.1: Various Space-borne GNSS-R Missions

GNSS-R Mission	**Launched date**	**Frequency Band**	**GNSS Constellation Used**
UK-DMC [4]	2003	L1	GPS
UK TDS-1 [79]	2015	L1	GPS
NASA CYGNSS [73]	2016	L1	GPS
Spire GNSS-R [80]	2019	L1	GPS, Galileo
PRETTY [31]	2022	L5	GPS, Galileo
HydroGNSS [33]	2025	L1, L5	GPS, Galileo

- Lack of Support for NavIC Signals: All current spaceborne GNSS-R missions rely exclusively on signals from global GNSS constellations—primarily GPS, Galileo, and sometimes QZSS or GLONASS. None of the existing GNSS-R payloads support the Indian Regional Navigation Satellite System (NavIC), despite its high signal strength and continuous visibility over the Indian subcontinent. This presents a major gap in regional GNSS-R development, particularly for localised applications in India such as precision agriculture, disaster resilience, and hydrological monitoring

- Heavy Payloads: Even the most recent and miniaturized GNSS-R payloads, such as those developed by Spire Global, weigh several kilograms (e.g., 5 kg) and require significant power and thermal regulation infrastructure. This makes them unsuitable for lightweight platforms like drones or UAVs, which are increasingly being used for near-surface remote sensing in agriculture, urban monitoring, and localized disaster assessments.

To address these limitations, this research proposes the development of a Software-Defined GNSS-R receiver capable of processing both NavIC-L5 and GPS-L1 signals for reflectometry. The system will be lightweight, low-power, and modular, allowing it to be mounted on drones, high-altitude platforms (HAPs), or small satellites, vastly expanding the use cases of GNSS-R.

2.2 Applications of GNSS-R

GNSS-R is an innovative technique that leverages reflected GNSS signals to monitor and measure various geophysical properties. It has provided major advances in understanding the climate system and its changes by quantifying processes and spatio-temporal states of the atmosphere, land and oceans. The applications of GNSS-R [81] span across oceanography, cryosphere studies, and terrestrial observations, providing significant advancements in understanding the Earth's systems. Typical application areas of GNSS-R are shown in Fig. 2.2, which include land surface remote sensing, soil moisture and vegetation estimation, maritime target tracking and localisation, and sea-state and sea-ice estimation. The reflected GNSS signals received by the GNSS-R receiver contain geophysical parameters of the underlying surface. A detailed description of some of the major application areas of GNSS-R is provided in the following sections.

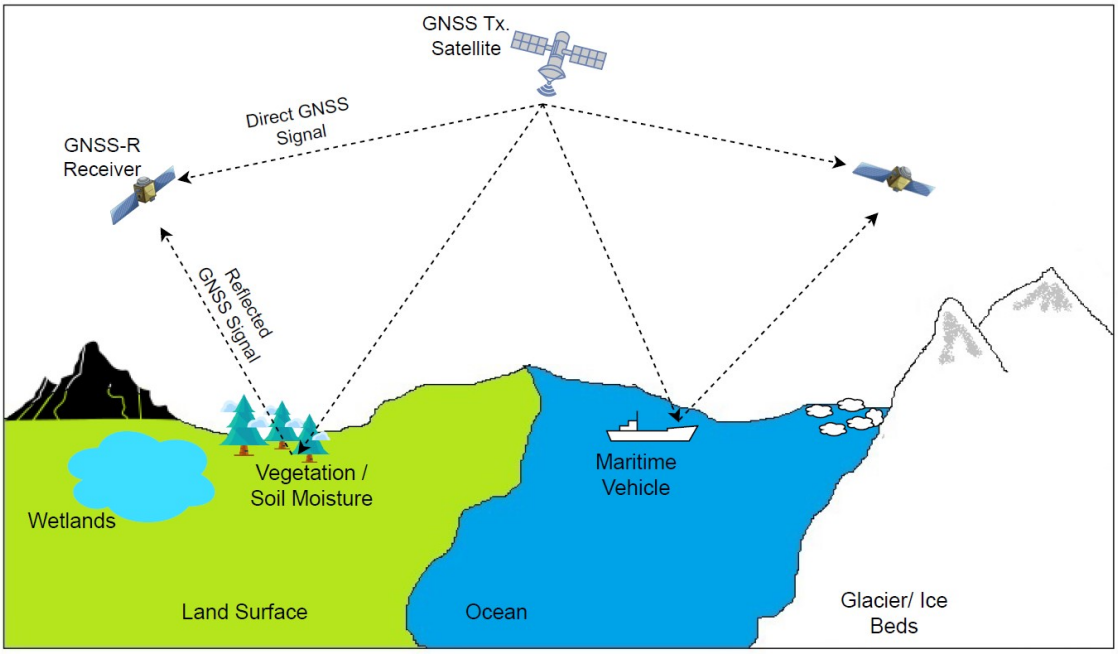

Figure 2.2: Applications of GNSS-R

2.2.1 Altimetry measurement

The effect of the increase in sea level and global warming is of utmost concern for the human habitat on islands and in coastal areas. These regions are extremely prone to extreme weather conditions such as cyclones, high tides, storms and waves that affect not only the humans of these regions

but also the economic status of these places. Therefore the measurements of sea level are of great importance. Observations from tide gauges measure the level of the sea with respect to the ground level on which these places are located, i.e., it measures the vertical distance between the land and the sea surface, related to the Earth's crust. The resulting measurements of sea level using a tide gauge are then directly correlated to the volume of the ocean. However, the above-mentioned method is not always feasible to carry out, which gives rise to the GNSS-R measurements. Now, the Global Navigation Satellite System (GNSS) signals are available globally, and moreover, the GNSS receiver technique is cost-effective. Therefore, the measurements of differential path delay between direct and ocean-reflected GNSS signals enable passive altimetry [82] from space-borne [83, 84] and air receivers [85, 86] and hence fill the gaps of existing altimetry techniques. To understand the global changes, estimation of sea level is essential. The recent increase in the measurement of sea level has led to the studies of GNSS-R for ocean height measurement altimetry [57, 87]. GNSS-R for ocean altimetry was first proposed in [88].

In the paper [12] for sea altimetry, the electromagnetic path differences method is applied between the direct Global Positioning System (GPS) signals and the lake reflected signal. The measurement resulted in 2-cm precision in the lake surface height estimates in 1 second. It is the first high-precision altimetry measurement with GPS signals from and an altitude of 480 m to study basic experimental errors, which be used for calibrating future air and space-borne passive GPS altimetry. It also acts as the first confirmation of a new technique for altimetric remote sensing in the coastal and sea region, a region that can not be measured easily by conventional radar altimetry. The GNSS-R ocean altimetry is explored extensively, but the earlier studies used the Delay waveform (DW) only in the estimation of ocean surface height.

The paper [1] explores the use of the "full -Doppler Map (DDM)" method in estimating the sea surface height and applies this technique to the observations of TechDemoSat-1 (TDS-1) data, a recent space-borne mission for reflectometry. The methods using a complete Delay-Doppler Map (DDM), which is defined as the amplitude/power distribution of the reflected signal in a 2-D array of delay offsets and Doppler shifts around the specular point [44], have been proposed in [71], to improve accuracy. According to [1] altimetry information is obtained from small shifts in the delay of the waveform. These shifts are typically smaller than the apparent "resolution" of the

DDM itself, making the use of additional information beyond the delayed waveform valuable to reduce the influence of "speckle" noise on the retrieval process.

2.2.2 Vegetation cover and Soil moisture studies

Estimating soil water content is essential for assessing flood prediction, weather forecasting, climate changes and aquifer recharge studies [89]. The presence of vegetation cover affect the soil moisture measurements [90]. Therefore, evaluating vegetation parameters, such as vegetation height, vegetation cover, and water content, is valuable to ecology and hydrology communities concerned with using remote sensing data products for vegetation cover, height and soil moisture estimation. Soil water content is estimated in-situ at many places, but either for individual studies or monitoring networks. While this analysis is helpful for small-scale or regional works, their applicability for global studies is limited because of the reasons stated: The in-situ data lack standardized instrumentation, direct measurements are labour intensive and destructive, and continuous measurement is also not possible.

Here, it is demonstrated that GNSS signal receivers already set up for geodetic, geophysical, and positioning applications can also be used to assess variations in soil water content [24, 91]. It is achievable because GNSS receivers collect energy from land reflections in addition to the direct signal received by the receiving antenna from the GNSS satellite. Therefore, with the change in soil moisture and the dielectric value of the ground, the characteristics of the multi-path signal change. Moreover, the GNSS signal pierces deeper into the dry soil as compared to when it is wet. With the change in "reflector" depth and the variation in dielectric value, the frequency and amplitude, along with the GNSS signal strength, change [16, 92].

The multipath signal alters all variables i.e. pseudorange, carrier-phase and signal-to-noise ratio (SNR) being collected by a GNSS receiver. The SNR is mainly used for reflectometry analysis. The phase of SNR observation is a function of satellite-reflector-antenna geometry. The SNR measurements give a measure of signal phase and amplitude that is independent of orbits, atmospheric delays, and clock variations, unlike the pseudorange observable and carrier phase. The SNR values that are measured are the addition of the multipath and direct signal components. As

the GNSS-R technique works on the multipath reflection, so, the direct signal component needs to be removed. As the signal above ∼30 degrees elevation angle has no significant oscillations due to multipath, therefore, it needs to be removed from the remaining SNR series. The SNR data is finally converted into volts from the native dB-Hz units to have a linear representation of the data. The SNR data need to be modified to a linear scale to remove the direct signal component. The SNR data should be detrended as well with a low-order polynomial to remove the effect of the direct signal. The reduced SNR signal has previously been modelled using the following equation [93]:

$$SNR = A\cos\left(\frac{4\pi h}{\lambda}\sin E + \Phi\right) \tag{2.1}$$

where A is constant amplitude, h is the height of the antenna, λ is the GPS wavelength, E is the elevation angle of the satellite, and ϕ is the phase shift. A and ϕ are then calculated from the SNR data using the least-squares estimation technique, with the best estimate of the height of the antenna.

Moreover, the different relative dielectric constant of the surface under observation causes the reflected signal to have different waveform patterns. This alteration in the signal characteristics is due to the variation of the amplitude, phase, frequency, and other information of the reflected signal. The soil moisture content is positively correlated with the soil dielectric constant; that is, the high moisture content indicates that the dielectric constant value is also higher [94]. It has been proved in the field of experiments and a modelling study that signal amplitude and phase ϕ are sensitive to changes in soil moisture content. This is because, for microwave frequencies, dielectric value or land surface's permittivity is primarily a function of its water content. Some spaceborne GNSS-R missions, including TDS-1 [95, 96] and CYGNSS [97, 98, 99], were designed to monitor and observe the ocean. However, the scattered signals received from the land surface have led to investigations in land surface parameter extraction, including soil moisture estimation and vegetation monitoring using the TDS-1 [100, 90, 101] and CYGNSS [102, 103, 104] received signals.

In future work, the effect of changes in GNSS equipment, i.e. antennas and receivers, needs to be assessed. Moreover, retrieval algorithms need to be studied and modified. This will

lead to the advancement of retrieval algorithms for the GNSS soil moisture estimation, including models which explain the dielectric value of distinct types of soils and soil moisture profiles. The long-term motive is to establish a retrieval algorithm to convert GNSS SNR data to soil water content estimates. To achieve this objective, we fully need to understand the various environmental factors that affect the SNR data. In future satellite reflectometry missions, GNSS soil moisture content data will be highly useful for validating and calibrating planned missions for soil moisture estimation.

2.2.3 Snow height estimation

Snow is one of the essential components of the climate and hydrological system, which impacts the water cycle and atmospheric circulation. Snow density and depth are the most important parameters for hydrological study because they represent the amount of water potentially available for runoff. Water runoff from snow melt is an important water resource feeding one-sixth of the world population [105]. Also, accurate measurements of snowpack properties are needed to understand better the effects of climate variability on water resource availability [106].

It is first demonstrated in [107] that the snow depth retrieved from traditional geodetic-GPS receivers has a good agreement with in situ depth measurements, indicating that geodetic-GPS receivers can be used to estimate snow depth [108]. Global Navigation Satellite System (GNSS) ground stations have been successfully used to continuously estimate snow depth at an intermediate scale of about 1.000 m^2 around the stations. Assuming a horizontal and a planar reflector (ground, snow, etc.), the interference between the reflected and the direct GPS signals produces approximately a sinusoid of constant frequency in SNR observations [24]. Multiple cycles of this modulation pattern must be observed to estimate that frequency, which is then related to the height of the antenna above the reflecting surface. As GPS signals reflect off the snow surface, the frequency decreases with increasing snow depth because the frequency $f = \frac{4\pi h}{\lambda}$ of the interference pattern depends on the wavelength λ of the GNSS carrier and the height h of the GNSS antenna above a reflecting planar surface [109]. After modelling the GPS SNR data [110], most of the difference between the solutions is seen in the signal amplitude, but it is not used for

data analysis [14]. The use of the amplitude data is complex because it can also be affected by the roughness of the surface, which would be expected to vary as the snow surface is scoured by wind.

In contrast to previous studies, where the GNSS stations were situated on bare soil [111] or grassland, The study presented in [109] is focused on monitoring snow depth in a built-up area with several constructions in the proximity of the station. The most challenging task at this site is to separate the GNSS reflections from the ground and from surrounding buildings. Here, snow depth is calculated as the difference between the GNSS reflector height above the soil and the snow surface. The frequency of the interference pattern was calculated using the Lomb–Scargle periodogram method, an algorithm to calculate the spectral power for irregularly spaced time series. The Lomb–Scargle periodogram with the frequency, converted into reflector height, often shows two significant peaks. The dominant frequency does not always correspond to the reflections from the ground. Especially on days with snow cover, the reflections from the roof show larger amplitudes than the reflections from the ground. Therefore the algorithm proposed in [112] for rural areas is modified for built-up areas. In order to avoid reflections from the roof, the range for picking the largest amplitude is restricted to a particular range. The range was derived by the median of the reflector height plus or minus 2 m.

Most previous studies use GPS L1C/A and L2C [113, 114] Signal-to-Noise Ratio (SNR) data to retrieve snow depth. In paper [115], snow depth variations are retrieved from new weak GPS L2P SNR data. The method employed here uses the multipath SNR data caused by the interference between direct and reflected signals. The frequency of multipath oscillations changes with the antenna height variations, so the snow depth can be estimated based on this relationship. The main procedures for retrieving snow depth from GPS SNR data can be summarized as follows:

- Using low-order polynomial function to fit GPS SNR time series and remove the direct trend, and the multipath oscillations are obtained.
- The frequency domain of multipath oscillations is obtained using the Lomb–Scargle periodogram.
- Finally, the frequency is converted to the reflector height.

These results in [115] indicate that geodetic GPS observations with SNR L2P data can reasonably estimate snow depths with a high correlation value. The GNSS reflected signals from each layer of snow allow the estimate of snow and ice thickness, and it has been explained in detail in [116]. Sea-ice measurement is performed by estimating the reflected signal delay and modelling the depth based on the angle of incidence. Extensive research [107, 14, 117, 118, 119] has been carried out to show the feasibility of GNSS-R for snow depth measurements.

2.2.4 Wetland estimation

The rapid urbanization, human encroachment and weather changes have led to wetlands collapse on a large scale. Therefore it is necessary to closely study and restore the world's wetlands for people and nature. Wetlands are home to a wide variety of fauna and flora specific to wetlands and support various ecosystem services like flood reduction. Wetlands can be used for water storage, which will contribute to groundwater recharge as well. It will help in local hydrology and ecosystem requirements. As it is challenging to observe the wetlands using in-situ methods, passive remote sensing is the only feasible way to study wetland extent globally. However, previous remote sensing and in-situ methods lack Spatio-temporal resolution and hence limit the ability to exist methods to measure the wetland dynamics at appropriate scales. GNSS Reflectometry can potentially fill the limitations in measurements, as experimental GNSS data [120, 121] proves that ground-reflected GNSS signals are susceptible to changes in inundated areas.

By estimating GNSS-R data captured from the Technology Demonstration Satellite (TDS-1) and a 2005 aircraft experiment over the Ebro delta in Spain [122], it is proven that the reflections over wetlands have a very strong coherent component and the peak values are several dB higher (even reaching 10 dB, equivalent to one order of magnitude) than the reflections from the surrounding drylands. For coherent reflections, the area contributing to the peak power is approximately equal to the first Fresnel zone, which is nearly less than a kilometre for low Earth-orbiting satellites. The signal-to-noise ratio (SNR) is considered and evaluated in order to sum up the temporal changes and spatial features in DDMs over wetlands. The peak value will be affected by the dielectric constant of the reflecting surface, underlying medium and roughness, which will, in turn,

determine the extent of coherence in the signal.

From the study of closed wetlands, it is proved that the coherence in the reflected GNSS signal is strong, which is reflected from the glistening zones, and the signal power decreases rapidly away from the wetlands. The coherent reflections are expected to come from the signals reflected from the water surface, which the vegetation cover can possibly attenuate. On the other hand, incoherent scattering includes scattering from tree leaves and branches, contributions due to the soil and trunk interactions, multiple interactions between vegetation elements and between the vegetation and the soil, and incoherent scattering from the soil attenuated by the overlapping vegetation canopy. Analysis of DDMs over flatlands and open wetlands shows an extensive dynamic range and coherence in the reflected signal, which proves that ground-reflected GNSS signals have a large sensitivity to small spatial features in many regions.

In conclusion, GNSS-R is an emerging means of remotely sensing oceans, land or glaciers, and snow fields using the reflected signals of the GNSS. As a long-term stable and free source of L-band signals, GNSS satellites fully leverage the advantages of the GNSS system, including all-weather, all-time, broad coverage, high temporal and spatial resolution, etc. In particular, GNSS-R can be used to determine sea surface wind [123], estimate seawater salinity [124, 125] and sea surface oil spills in oceans [126, 127], monitor soil moisture and plant growth on land and measure sea ice thickness, snow thickness, density, roughness, etc. Further, with the expansion of multi-frequency [128, 129] multi-GNSS constellations and space-based augmentation systems and the implementation of spaceborne GNSS reflection measurement missions (such as the upcoming HydroGNSS mission [33, 130, 78]), one will get larger coverage and spatial-resolution surface feature information.

2.2.5 Target Localisation using GNSS-R

Global Navigation Satellite Systems (GNSS) provide signals that cover the entire Earth's surface, enabling a range of alternative applications beyond their primary purpose of navigation and positioning. Among these, the analysis of GNSS-reflected signals, known as GNSS reflectometry (GNSS-R), has been extensively studied and utilized for remote sensing of the Earth's atmosphere,

ionosphere, oceans, land surfaces, and cryosphere. This technique leverages GNSS signals as illuminators of opportunity due to their global availability and abundance. GNSS-R has proven effective in Earth observation applications, including soil moisture estimation, ocean altimetry, sea state characterization, and wind speed measurement. Recently, an innovative application of GNSS-R has emerged in the domain of passive radar systems for maritime target detection.

Passive radar systems, which rely on external sources of illumination, are particularly advantageous for maritime surveillance because of their low cost, covert operation, and capability to monitor areas beyond territorial waters. GNSS satellites, as illuminators of opportunity, are uniquely suited for this purpose due to their extensive coverage and the simultaneous illumination of an area by 6-8 satellites from a single GNSS constellation. This enables the development of a multi-static radar system, where signals from multiple satellites can be received simultaneously by a single sensor, enhancing the overall system performance. In recent works by [131, 132, 133], the feasibility of using the GNSS as transmitters of opportunity in a passive bistatic radar system for maritime target detection applications.

GNSS-based passive radar systems for maritime surveillance typically consist of two RF channels: one for receiving the direct GNSS signal and another for capturing the reflected signal. The direct signal is used for synchronization and for detecting changes in delay and Doppler shifts, which are then used to generate a noise-free replica of the signal. This replica is correlated with the reflected signal, and range match filtering is applied to produce Range-Doppler (R-D) maps, which provide information on the bistatic range and velocity of targets. These R-D maps are further processed to optimize target tracking and localisation, enabling the system to effectively detect and monitor maritime moving targets. This approach represents a significant advancement in the use of GNSS signals for passive radar applications, providing a robust, cost-effective solution for maritime domain awareness. A basic block diagram for target localisation is shown in Fig. 2.3

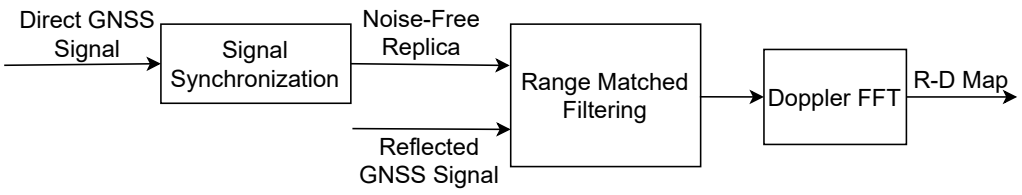

Figure 2.3: Basic Target Localisation Algorithm

2.3 GNSS-R Theoretical Concept

The signals broadcast by GNSS satellites are coded with ranging and timing information. This information allows a receiver to estimate the line-of-sight range from its location to the satellite with high accuracy and precision. These signals also reflect from the Earth's surface and are received by GNSS receivers for remote sensing. This technique is termed GNSS Reflectometry, and it is a form of bistatic radar [134, 135, 136]. On the other hand, most radar systems, such as those used for monitoring air space, harbour approaches, and weather forecasting, combine the radar transmitter and receiver at the same site, the so-called monostatic radar. The bistatic systems use transmitters and receivers separated by a considerable distance. In a bistatic radar application, the surface reflected signals are received in conjunction with the direct GNSS signals. Parameters of the reflecting surface, such as its bistatic range and reflectivity, are derived from the reflected signal properties. The power observed by the receiver in a bistatic radar configuration can be expressed by means of the bistatic radar equation, given as follows [137]:

$$P_{pq}^{r} = \frac{P_t \lambda^2}{(4\pi)^3} \int \frac{G_t G_r}{R_{ts}^2 R_{rs}^2} \sigma_{pq}^{0} dA \tag{2.2}$$

where P_t denotes the GNSS transmitted signal power, λ is the wavelength of the signal, G_t and G_r are the transmitting and receiving antenna gain respectively, R_{ts} and R_{rs} is the distance from the transmitter and the receiver to the specular point respectively, σ_{pq}° is the bistatic radar coefficient for a particular pq polarisation. The bistatic radar coefficient (or normalized radar cross-section) describes the object's ability to re-radiate the incident energy in a certain direction. By definition, this is the ratio between the scattered power density per unit area and the power density re-radiated by an isotropic scatterer [134].

$$\sigma_{pq}^{0} = 4\pi R_{rs}^2 \frac{\left|E_{pq}^{s}\right|^2}{A\left|E_p\right|^2} \tag{2.3}$$

where E_p and E_{pq}^{s} are the incident and scattered fields. A is the total area of the illuminated surface, and R_{rs}^2 is the distance of the point of observation to the centre of A. The concept of

bistatic radar can be extended to satellite signals. Since signals transmitted by a satellite get scattered off the Earth's surface, detecting these reflections by a separated passive receiver could provide some information about the surface. In GNSS-R, a single receiver picks up the direct and reflected signals coming from multiple GNSS satellites to retrieve the geophysical parameters of the scattering surface (multi-static configuration). With the increasing number of GNSS satellites, a single receiver could potentially get signals from more than 20 emitters at the same time, thus obtaining a high number of independent observations of the same scene, which could either be used to increase the instrument's swath, or to reduce the noise in the estimation of geophysical parameters.

Now, examining the GNSS signal architecture. The properties of the GNSS signal enter the radar equation through the ambiguity function χ and are defined through the GNSS signal structure. A thorough reference for GNSS receiver fundamentals and signal structures is provided by [138] and [139]. For a given time t, the direct GNSS signal at a receiver's location can be expressed as:

$$S_d = \sqrt{\frac{P_t G_t}{4\pi}} a\left(t - \frac{R_{tr}}{c}\right) \frac{e^{-jkR_{tr}}}{R_{tr}} e^{-j2\pi(f_c+f_d)t} \tag{2.4}$$

where $a(t)$ represents the modulating PRN code, k is the wavenumber, f_c and f_d are the carrier frequency and the Doppler frequency shift, respectively. The previous equation 2.4 can also be used to express the field reflected from a perfectly flat surface. It is considered that the actual source is replaced by a mirrored one below the surface. The reflected GNSS signal structure is defined as:

$$S_{ref} = \sqrt{\frac{P_t G_t}{4\pi}} \sigma_0 a\left(t - \frac{R_{ts} + R_{rs}}{c}\right) \frac{e^{-jkR_{ts}+Rrs}}{R_{ts} + R_{rs}} e^{-j2\pi(f_c+f_d)t} \tag{2.5}$$

where σ_0 is the Fresnel reflection coefficient at the specular point. In GNSS-R, the reflected signal power arriving at the receiver can be modelled by the integration over the surface ρ.

$$P_{rx}^{r} = \frac{T_i^2 P_t G_t \lambda^2}{(4\pi)^3} \iint\limits_{\rho} \frac{G_r(\vec{\rho})}{R_{ts}(\vec{\rho}) R_{rs}(\vec{\rho})} \sigma_{pq}^{\circ} \chi^2(\vec{\rho}; \delta\tau, \delta f) d\vec{\rho} \tag{2.6}$$

where T_i is the coherent integration time, and $\chi(\vec{\rho}; \delta\tau, \delta f)$ is known as the Woodward Ambiguity Function (WAF). The WAF is the result of the matched filtering of the signal for the delay and Doppler frequency of the reflection and depends on the properties of the signal. The delay and Doppler are represented by τ and f, respectively. WAF is a product of two functions associated with the delay offset (τ) and Doppler shifts (f_d). WAF is expressed as follows [140]:

$$\chi^2(\vec{\rho}; \delta\tau, \delta f) \simeq \Lambda^2(\tau) \cdot |S(f_d)|^2 \tag{2.7}$$

where $\Lambda = 1 - |\tau| / \tau_c$ if $|\tau| \leq \tau_c$ and 0 otherwise, here τ_c represents the C/A code chip length. $\Lambda(\tau)$ is the PRN code autocorrelation, and it represents the impulse response of the system in the time domain. Whereas $|S(f_d)|$ represents the response of the system in the Doppler dimension and is represented as $|S(f)| = |sin(\pi f)/(\pi f)|$.

The geometry of the GNSS-R experiment is explained in Fig. 2.4. Here, the GNSS navigation satellite is used as a transmitter, and a GNSS-R receiver is placed on board a LEO or UAV that can receive both the direct and reflected GNSS signals. The size of the active region from where the specular reflections are received is defined by the first Fresnel zone [141]. Specular reflection is characterized by incidence and reflection angles that are equal and form a plane containing the transmitter, receiver, and surface reflection point. When the distance from the surface to the transmitter is much larger than the distance from the surface to the receiver (or vice versa), the semi-major axis a and semi-minor axis b of the first Fresnel ellipse are dependent upon the elevation angle E and minimum height of the transmitter or receiver h, and is given as follows:

$$a = \frac{\sqrt{\lambda h \sin E}}{(\sin E)^2}, b = \frac{\sqrt{\lambda h \sin E}}{\sin E} \tag{2.8}$$

where λ is the GNSS signal wavelength.

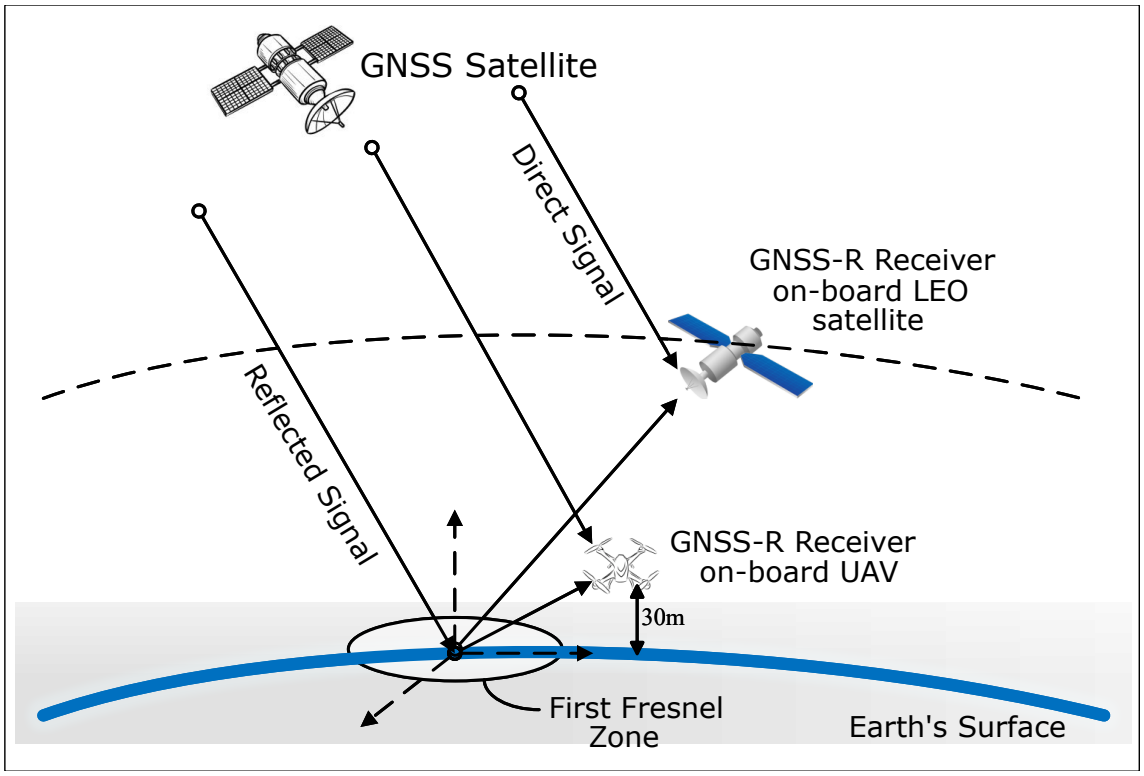

Figure 2.4: GNSS-R geometry

For a perfectly smooth surface, the reflected power is considered as coherent [142] and is governed mainly by the Fresnel reflection coefficient of the active region from which power is reflected. Now, as the surface roughness increases, the coherent component of the reflected signal decreases, and the surface scatters more power incoherently in other directions. For rough surfaces, the active scattering region of the surface expands beyond the first Fresnel zone to a glistening zone surrounding the specular reflection point.

2.3.1 GNSS-R Observable: The Delay Doppler Map

In radar, the ambiguity function measures the similarity between a signal and a delayed and Doppler-shifted version of it. The GNSS-R equivalent to this ambiguity function is known as a delay–Doppler map (DDM) [143]. A DDM consists of the power distribution of the reflected signal over the 2-D space of delay offsets and Doppler shifts. The distribution of the GNSS scattered power as a function of delay and frequency is defined as:

$$|P(\tau, f)|^2 = \frac{T_i^2 P_t G_t \lambda^2}{(4\pi)^3} \iint\limits_A \frac{G_r(\vec{\rho})}{R_{ts}(\vec{\rho}) R_{rs}(\vec{\rho})} \sigma^{\circ}_{pq} \chi^2(\vec{\rho}; \delta\tau, \delta f) d\vec{\rho} \tag{2.9}$$

by selecting different (τ, f) pairs, the contributions coming from different cells on the surface can be observed due to the spatial filtering of the WAF. These cells are the intersections of iso-delay and iso-doppler stripes at any point on the surface with a width determined by the GNSS PRN code chip for the delay and by the coherent integration time for the Doppler. The DDM coordinates are referenced with respect to the specular point so that the delay and Doppler pair (0,0) correspond to the specular point itself. The DDM "horseshoe" shape is primarily due to the frequency filtering as indicated by the sinc function in 2.7. The rougher the scattering surface, the more probable it is for regions far away from the specular point to contribute to the final scattered power, contributing to smearing the DDM towards higher Doppler frequencies. On the contrary, for a flat surface, the scattering is produced around the specular point, and therefore, the DDM will be more concentrated around the (0,0) point. The area contributing to the specular reflections is mainly calculated using 2.8.

DDM Numerical Simulation

DDM numerical simulation is an essential step while performing the hardware-in-loop simulations and theoretical verification of the receivers. The power distribution over delay-doppler space is expressed as shown in 2.9. To obtain simulated DDMs, 2.9 can straightforwardly be implemented by defining the scenario (the reflecting surface, the transmitter, and the receiver) in a reference system and evaluating the functions inside the integral to compute the integral for every (τ, f_d) coordinate. However, such an approach becomes extremely time and resource-consuming [140] as the simulated observed surface increases in size, as it happens for space-borne receivers since the glistening zone extends over hundreds of kilometres. The first step to accelerate the simulation consists of expressing the DDM as a 2-D convolution that can efficiently be computed by means of a 2-D fast Fourier transform and is represented as:

$$\left\langle |P(\tau, f_d)|^2 \right\rangle = \chi^2(\tau, f_d) ** \sum(\tau, f_d) \tag{2.10}$$

where χ^2 is the ambiguity function as defined in 2.7. This ambiguity function is independent of the pixel position and can be computed in a straightforward manner and only once for all the pixels. Now, $\sum(\tau, f_d)$ is termed as the weight function associated with each delay-Doppler bin. This function accounts for the surface geometry, the antenna patterns, and other terms from the bistatic radar equation and is defined as follows:

$$\sum(\tau, f_d) = T_i^2 \iint_{\rho} \frac{D^2(\vec{\rho})\sigma_0(\vec{\rho})}{4\pi R_{ts}^2 R_{rs}^2} \times \delta(\tau - \tau(\vec{\rho}))\delta(f_d - f_d(\vec{\rho}))d^2\rho \tag{2.11}$$

The power received using the GNSS signals has two components: coherent and incoherent. Hence, received power P_r is written as:

$$P_r = P_r^{coh} + P_r^{incoh} \tag{2.12}$$

The bistatic radar equation describing the coherent component of the received power is modelled as follows:

$$P_r^{coh} = \frac{P_t \lambda^2 G_t G_r}{(4\pi)^2 (R_{ts} + R_{rs})^2} \left|\Gamma_{pq}\right|^2 \tag{2.13}$$

whereas the incoherent component is modelled as:

$$P_r^{incoh} = \frac{P_t \lambda^2 G_t G_r \sigma^0 A_{eff}}{(4\pi)^3 R_{ts}^2 R_{rs}^2} \tag{2.14}$$

where A_{eff} is the area of the glistening zone. According to the bistatic radar equation, the coherently reflected power at the receiver is a function of surface reflectivity Γ_p. The surface reflectivity Γ_p is defined as [102]:

$$\Gamma_p(\epsilon_s, \theta_i) = \left| \frac{1}{2}(R_{vv} - R_{hh}) \right|^2 \tag{2.15}$$

where R_{vv} and R_{hh} are fresnel coefficients for vertical and horizontal polarization and are defined as [102]:

$$R_{vv}(\epsilon_s, \theta_i) = \frac{\epsilon_s cos\theta_i - \sqrt{\epsilon_s - sin^2\theta_i}}{\epsilon_s cos\theta_i + \sqrt{\epsilon_s - sin^2\theta_i}} \tag{2.16}$$

$$R_{hh}(\epsilon_s, \theta_i) = \frac{cos\theta_i - \sqrt{\epsilon_s - sin^2\theta_i}}{cos\theta_i + \sqrt{\epsilon_s - sin^2\theta_i}} \tag{2.17}$$

where ϵ_s is the dielectric constant and θ_i is the incidence angle. According to (2.15) the surface reflectivity Γ_p is a function of the surface dielectric constant, which further depends on the soil moisture; hence the change in surface soil moisture will affect the coherent reflected power received at the GNSS receiver. Once the DDMs are obtained, the coherent reflected peak power can be calculated. Further, the peak power is used to calculate the surface reflectivity and can be derived using (5.3) as follows [144, 145]:

$$\Gamma_p(\epsilon_s, \theta_i) = \frac{(4\pi)^2 (P_{DDM})(R_{ts} + R_{rs})^2}{\lambda^2 P_t G_t G_r} \tag{2.18}$$

where P_{DDM} is the DDM peak power. The surface reflectivity obtained using (2.18) is further used to retrieve the dielectric constant by using (2.15), (2.16) and (2.17). As shown in equation 2.18, the surface reflectivity can successfully be derived from the DDM-derived power. Hence, DDM is an important GNSS-R observable that is used for remote sensing.

2.4 GNSS Signal Acquisition

The acquisition process is a fundamental step in GNSS signal processing, aiming to determine the visible satellites and estimate the coarse values of two critical parameters: carrier frequency and code phase. Satellites are uniquely identified by their specific Pseudo-Random Noise (PRN) sequences [146]. The acquisition process involves detecting these PRN codes and estimating the code phase, which is the time alignment of the PRN code within the current block of data. Determining the code phase is essential for generating a local replica of the PRN code that is perfectly

synchronized with the incoming signal. Accurate alignment is critical because PRN codes exhibit high correlation only when there is zero lag between the locally generated code and the incoming signal. This perfect alignment enables the removal of the PRN code from the received signal, allowing the receiver to extract meaningful information from the signal. In addition to the code phase, the acquisition process also estimates the carrier frequency, which corresponds to the Intermediate Frequency (IF) after down-conversion. The IF is determined by the difference between the signal's original carrier frequency and the frequency of the local oscillator in the downconverter. Precise knowledge of the IF is vital for correctly demodulating the signal and mitigating the effects of Doppler shift caused by the relative motion between the satellite and the receiver.

An acquisition method is employed to detect the presence of a satellite signal and estimate the necessary parameters to track and decode the information embedded in GNSS signals. Once the signal is acquired, the estimated parameters, such as code phase and carrier frequency, are passed to the tracking program. The acquisition process thus serves as a crucial bridge between signal detection and the extraction of meaningful data.

Three primary acquisition methods are commonly used in GNSS processing: conventional acquisition, Fast Fourier Transform (FFT)-based acquisition, and delay-and-multiply acquisition. The conventional acquisition method employs a serial search technique, where the receiver generates and correlates local PRN codes across a range of code phases and Doppler frequencies. While this method is straightforward, it is computationally intensive and time-consuming, particularly for large search spaces. The FFT-based acquisition method leverages the efficiency of the Fourier transform to accelerate the correlation process. By converting the incoming signal and the local PRN code into the frequency domain, this method significantly reduces the computational burden, making it well-suited for real-time applications. The delay-and-multiply acquisition method involves delaying the incoming signal by one chip and multiplying it with itself. This technique generates a unique spectral signature for each PRN code, simplifying the identification of visible satellites. By employing efficient acquisition methods and incorporating techniques for weak signal detection, modern GNSS receivers can achieve robust performance across a wide range of environments and applications.

2.4.1 Serial Search Acquisition

The algorithm is based on the multiplication of locally generated PRN code sequences and locally generated carrier signals [147]. The first serial search acquisition method task is multiplying the incoming signal with the locally generated PRN sequence. Instead of generating PRN sequences every time the algorithm is executed, all possible PRN sequences are generated offline. The second step is multiplication with a locally generated carrier wave. The carrier generator must generate two carrier signals with a phase difference of 90°, corresponding to a cosine and a sine wave. The carrier must have a frequency corresponding to the IF ± the frequency step according to the examined frequency area.

The last parts of the serial search algorithm involve an integration and a squaring of the two results of the multiplications with the cosine and sine signals, respectively. The squaring is introduced to obtain the signal power. The integration is simply a summation of all points corresponding to the length of the processed data. The squaring is then performed on the result of the summation. The final step is to add the two values from the I and the Q. If the locally generated code is well aligned with the code in the incoming signal, and the frequency of the locally generated carrier matches the frequency of the incoming signal, the output will be significantly higher than if any of these criteria were not fulfilled. The block diagram of the serial search acquisition algorithm is shown in Fig. 2.5.

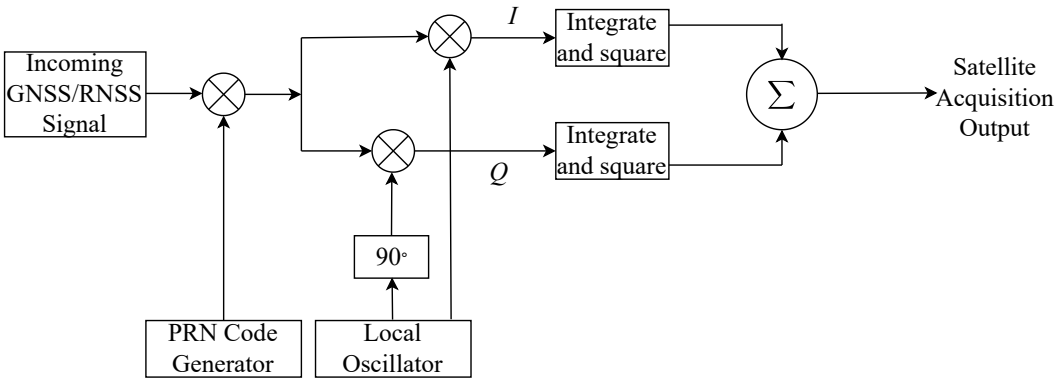

Figure 2.5: Serial search Acquisition Algorithm

2.4.2 Parallel Frequency Space Search Acquisition

As the name parallel frequency space search acquisition implies, this second method of acquisition parallelizes the search for one parameter. This method utilizes the Fourier transform to perform a transformation from the time domain into the frequency domain [148]. The incoming signal is multiplied by a locally generated PRN sequence, with a code corresponding to a specific satellite and a code phase between 0 and 1022 chips. The resulting signal is transformed into the frequency domain by a Fourier transform. With a perfectly aligned PRN code, the output of the Fourier transform will show a distinct peak in magnitude. The peak will be located at the frequency index corresponding to the frequency of the continuous wave signal and, thereby, the frequency of the carrier wave signal. The block diagram for the same is shown in Fig. 2.6.

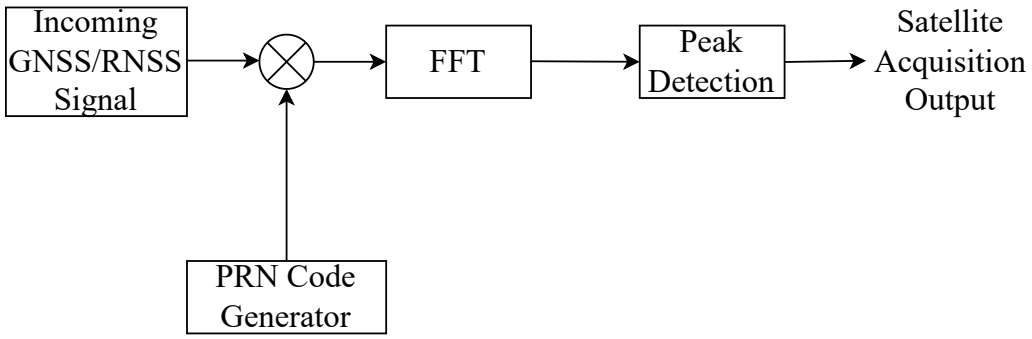

Figure 2.6: Parallel frequency search algorithm

2.4.3 Parallel Code Phase Search Acquisition

The previous method parallelized the frequency space search eliminating the necessity of searching through the possible frequencies. If the acquisition could be parallelized in the code phase dimension, only 41 steps should be performed compared to 1023 in the parallel frequency space search acquisition algorithm [149]. The incoming signal is multiplied by a locally generated carrier signal. Multiplication with the signal generates the I signal, and multiplication with a 90◦ phase-shifted version of the signal generates the Q signal. The I and Q signals are combined to form a complex input signal. The generated PRN code is transformed into the frequency domain and the result is complex conjugated. The Fourier transform of the input is multiplied by the Fourier transform of the PRN code. The result of the multiplication is transformed into the time domain by an inverse

Fourier transform. The absolute value of the output of the inverse Fourier transform represents the correlation between the input and the PRN code. If a peak is present in the correlation, the index of this peak marks the PRN code phase of the incoming signal. The block diagram for this acquisition algorithm is shown in Fig. 2.7

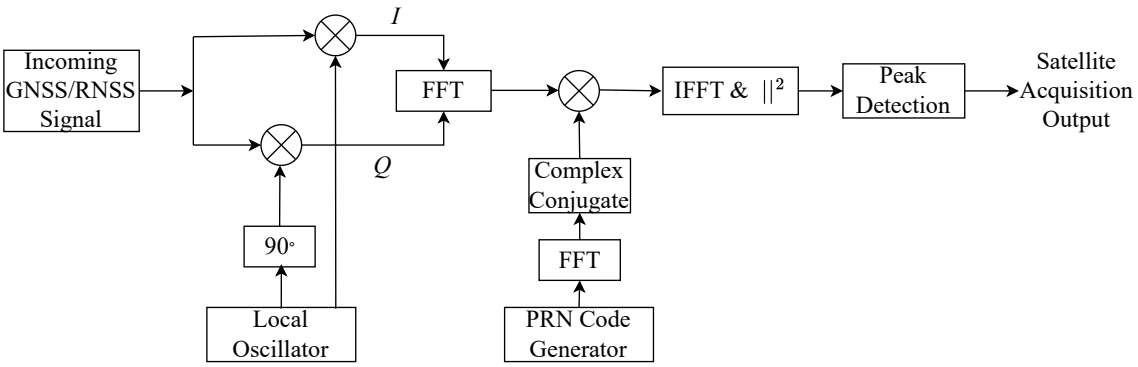

Figure 2.7: Parallel Code Phase search algorithm

2.4.4 Acquisition of weak signal

During the satellite signal acquisition process conducted on the field experiment data, it was observed that the typical 1 ms data interval was insufficient to achieve a reliable satellite acquisition lock. This limitation posed significant challenges, particularly when dealing with weak GNSS signals often encountered in environments with high noise levels, multipath interference, or low signal power. Achieving satellite acquisition lock is a critical step in GNSS-R processing, as it involves identifying visible satellites, estimating their Doppler shift, and determining the coarse time delay of incoming signals. Failure to acquire a lock can significantly hinder the subsequent stages of signal processing, such as tracking and generating Delay-Doppler Maps (DDMs).

Weak signal acquisition is particularly relevant for GNSS-R applications, where reflected signals are inherently weaker than direct signals due to propagation losses and surface scattering. This section discusses key approaches to weak signal acquisition, including coherent and non-coherent integration methods. Coherent integration involves aligning and summing signal samples over an extended period, maintaining phase coherence to maximize the accumulated signal power. While effective, this method requires precise Doppler compensation to prevent signal degradation

due to frequency shifts. Non-coherent integration, on the other hand, accumulates the squared magnitude of the signal, eliminating the need for phase alignment but resulting in a lower SNR improvement compared to coherent integration.

Non-Coherent Integration

Sometimes using 1 ms of data through the circular correlation method cannot detect a weak signal [150]. Longer data records are needed to acquire a weak signal. One way to process more data is through non-coherent integration. It can simply be performed by summing the k instances of the correlation output of the acquisition block. For example, if 2 ms of data are used, the data can be divided into two 1 ms blocks. Each 1 ms of data is processed separately, and the results are summed together. This operation basically doubles the number of operations, except for the addition in the last stage.

The improvement obtained by this method is less than with the coherent method but there are fewer operations. The block diagram of the non-coherent integration technique is shown in Fig. 2.8. Another advantage of this latter method is the ability to perform acquisition on successive 1 ms of data and sum the results. The final result can be compared with a certain threshold. Whenever the result crosses the threshold, the signal is found. A maximum data length can be chosen. Due to the squaring operation in the non-coherent integration, the noise floor gets positively biased.

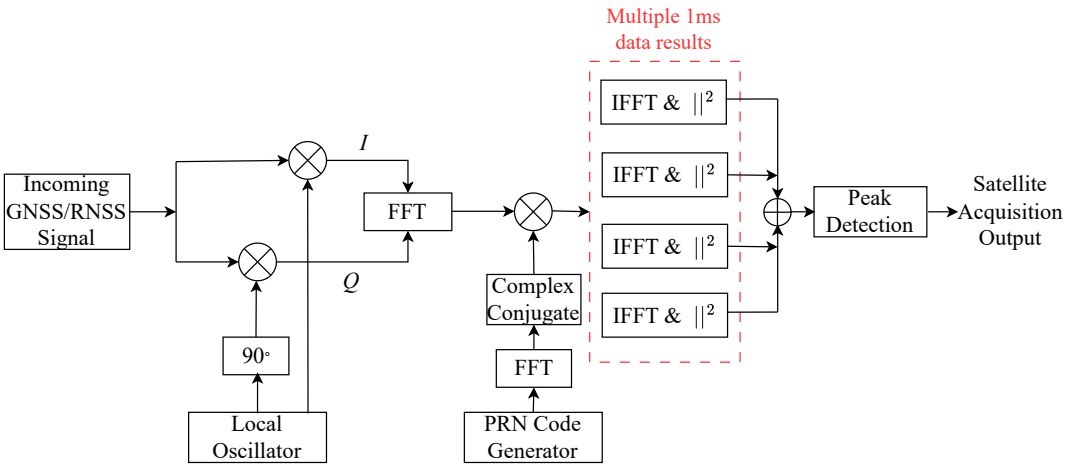

Figure 2.8: Non-Coherent Integration Technique

Coherent Integration

The coherent integration method presents the concept of processing a long data coherently. The common approach to acquiring weak signals [151] is to increase the data length in signal acquisition. However, the computation load is also enlarged if the data length is increased. The block diagram of the coherent integration technique is presented in Fig. 2.9.

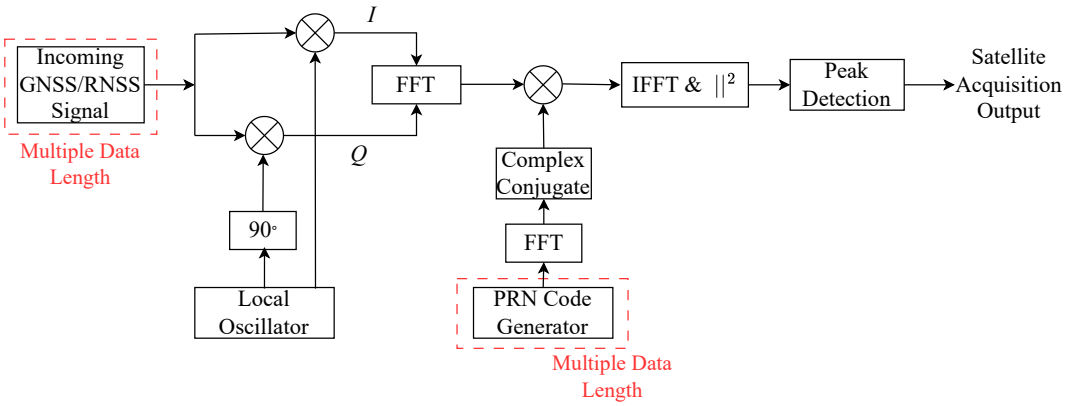

Figure 2.9: Coherent Integration Technique

In Coherent integration, "coherent" means matched in time/phase. It works on complex-valued measurements in which the signal's phases from measurement to measurement are in close alignment, thus allowing constructive addition of signal, whereas the phase of noise is random from measurement to measurement, resulting in cancellation.

Chapter 3

Compression of GNSS Reflectometry Data for On-board Processing and Transmission.

Contents

3.1 Introduction

One of the significant challenges in GNSS reflectometry (GNSS-R) is managing the extensive size of GNSS data, which can become exceedingly large even for a relatively short duration of observation. This issue is particularly prominent in real-time data collection scenarios, where large datasets can hinder efficient processing and transmission. In this study, the analysis is conducted on real-time raw GPS data collected from the TDS-1 satellite, which is made publicly available through the online portal merrbys.co.uk, with additional data access provided via the FTP server ftp://ftp.merrbys.co.uk. The raw data is processed using the softGNSS [152] algorithm, which extracts the data vector from the recorded stream. This data stream encompasses all GNSS signals within the filter bandwidth, as observed by both zenith and nadir antennas. The dataset under analysis corresponds to a duration of 2 minutes and 20 seconds, sampled at a rate of 16.367 MHz with a carrier frequency of 4.188 MHz. Despite this relatively short observation window, the dataset includes approximately 100,000 samples, resulting in a substantial data volume. Such a large dataset poses challenges for storage, processing, and especially transmission over wireless channels for GNSS-R applications, as the transmission time for these datasets can be prohibitively long. Consequently, there is a pressing need to develop advanced algorithms capable of effectively reducing the data volume while retaining the essential information required for GNSS-R analysis. Data reduction techniques are vital for addressing this challenge, as memory resources are generally constrained in satellite applications, and this will enable efficient storage on board the satellite and reduce the transmission overhead for real-time applications. Developing such algorithms would significantly enhance the feasibility and scalability of GNSS-R systems, enabling their deployment for a wider range of remote sensing and surveillance applications.

The above-mentioned problem can be solved by first compressing the GNSS data and then reconstructing it at the receiver end. The problem is segmented into three steps, the first step is the sparse representation of the GNSS data in a sparse domain. The second step is the formation of the measurement vector of lower dimensions than the original signal. The third step is the reconstruction of the original signal from a reduced number of measurement. According to previous work done in this area, a two-stage deterministic CS algorithm has been proposed.

However, the algorithm results in high computational complexity. Moreover, the deterministic CS matrix is not robust to noisy signal [153]. A study is performed in [154], which uses multiple measurement vectors as the reconstruction algorithm; this algorithm is complex as it uses multiple measurement CS theory. To solve these problems a compression and reconstruction algorithm based on compressive sensing is proposed in this work which is applicable to the noisy input signal as well. The proposed method has low algorithmic complexity than the previously proposed algorithms. Finally, the proposed algorithm has been used on both direct and multipath GNSS-R data collected by TechDemo satellite (TDS)-1. Application of the proposed algorithm shows that the algorithm implemented for compression and reconstruction of the GPS data gives a good performance in terms of reconstruction of the signal from the measurement vector. The SNR of the recovered signal for 60% sampling ratio is 27.88dB which is 1dB less as compared to the SNR of the original signal which is 28.10dB. The Normalised Mean Square Error (NMSE) performance for Discrete Cosine Transform (DCT), Discrete Wavelet Transform (DWT) sparsifying matrix and Toeplitz, Bernoulli and Gaussian measurement matrix is also compared.

3.2 Mathematical formulation and Methodology

Compressive sensing (CS) is an emerging signal processing technique that enables efficient compression and reconstruction of signals by exploiting their inherent sparsity in a specific transform domain. Unlike traditional sampling methods, which adhere to the Nyquist-Shannon sampling theorem, CS operates on the principle that signals with a sparse representation can be accurately reconstructed using fewer samples than required by conventional methods. This makes CS particularly useful for applications where acquiring large amounts of data is challenging or resource-intensive. In the context of GNSS signals, compressive sensing techniques [155, 156, 157] can be effectively applied as these signals exhibit sparsity in certain transform domains, such as the Discrete Cosine Transform (DCT) and Discrete Wavelet Transform (DWT).

During the compression process in CS, a reduced number of measurements is captured by discarding samples deemed insignificant in the sparse domain. This reduction in data acqui-

sition significantly lowers storage and transmission requirements while still retaining the essential information of the original signal. The missing information is then recovered through sparse recovery algorithms [158], such as Basis Pursuit, Orthogonal Matching Pursuit, or L1-minimization techniques. These algorithms iteratively reconstruct the signal by solving an optimization problem that minimizes the error between the reconstructed and original signals.

Consider a scenario in which we have a signal $x \in R^m$, of size $m \times 1$ that has a sparse representation in a transform domain. The signal can be represented sparsely in a particular transform domain, by multiplying the signal with the sparsifying matrix i.e. DCT or DWT matrix. Now, the signal having a reduced number of samples is constructed using the sparse signal, which is called the measurement vector. The measurement vector $y \in R^n$ of size $n \times 1$ where $n < m$ will be used for original signal recovery.

The vector $y \in R^n$ is a linear measurement of the signal x given by $y = Ax$, where A is the measurement or sensing matrix of size $n \times m$. This system is under-determined, so the reconstruction of the signal x is an ill-posed problem. Therefore, optimization algorithms are used to obtain an optimal solution for this system. The sparse signal recovery algorithms are based on convex-optimization technique. One of the method that is based on convex l_1 minimization which gives near optimal solution can be defined as:

$$min \left\|x\right\|_1 \text{ subject to } y = Ax \tag{3.1}$$

this convex minimization approach is called as Basis Pursuit (BP). However, in case of noisy measurements, the linear measurement vector is represented as $y = Ax + n$, where n is the noise and $\left\|n\right\|_2 < \varepsilon$, the optimization approach is called Basis Pursuit Denoising (BPDN) [159] and is defined as:

$$min \left\|x\right\|_1 subject\ to \left\|y - Ax\right\|_2 \leq \varepsilon \tag{3.2}$$

The BPDN algorithm can be solved using SPGL-Toolbox which is a Matlab solver for large-scale sparse reconstruction.

Consider the input signal $x \in R^m$ which is the In-phase (I) and Quadrature phase (Q)

signals from GNSS. At first, the sparse representation of GNSS Signal is performed by multiplying the signal with the sparsifying matrix, that can be either DCT or DWT matrix.

$$Dx = \psi \tag{3.3}$$

where D is the sparsifying matrix of dimension $m \times m$, x is the original signal of size $m \times 1$ and ψ is the sparse representation of the signal in D domain.

The second step is the construction of the measurement vector of size less than the original signal. It is obtained by performing the multiplication of the signal with the measurement matrix of size $n \times m$.

$$y = \phi x \quad i.e. \quad y = \phi D^{-1}\psi \tag{3.4}$$

where n is the no. of samples that depends on the sampling ratio, ϕ is the sensing matrix and y is the measurement vector of lower dimension.

Now, the signal is reconstructed by solving the convex l_1-norm minimisation of $\|Dx\|_1$ subject to the constraint provided below:

$$min \, \|Dx\|_1 \, subject \, to \, \|y - \Phi x\|_2^2 < \varepsilon \tag{3.5}$$

now, substituting $Dx = \psi$ results in minimisation of $\|\psi\|_1$ as shown below

$$min \, \|\psi\|_1 \, subject \, to \, \left\|y - \Phi D^{-1}\psi\right\|_2^2 < \varepsilon \tag{3.6}$$

Once the sparse signal ψ is computed, the original signal x can be recovered as:

$$\widehat{x} = D^{-1}\psi. \tag{3.7}$$

The procedure followed is summarized in the Algorithm 1 given below [160]:

Algorithm 1: CS based reconstuction algorithm

INPUT: x (GNSS Signal)

STEP1: Compression of GNSS signal, i.e. sparse representation and generation of measurement vector.

$$Dx = \psi$$

where D is the sparsifying marix and ψ is the sparse representation of GNSS signal.

$$y = \phi x \quad i.e. \quad y = \phi D^{-1}\psi$$

where y is the measurement vector and ϕ is the measurement matrix.

STEP2: Wireless transmission of measurement vector.

STEP3: Obtain the sparse signal using convex l_1 minimization algorithm.

$$min \left\|\psi\right\|_1 subject\ to \left\|y - \Phi D^{-1}\psi\right\|_2^2 < \varepsilon$$

STEP4: Reconstruction of original signal from the sparse vector.

$$\widehat{x} = D^{-1}\psi.$$

OUTPUT: $\widehat{x}$ (Reconstructed Signal)

3.3 Results and Analysis

The simulation results for reconstruction and comparison of different sparsifying and measurement matrices are presented. The normalised mean square error (NMSE) in signal reconstruction is calculated at different sampling ratio to show the comparison between different matrices. The NMSE is defined as:

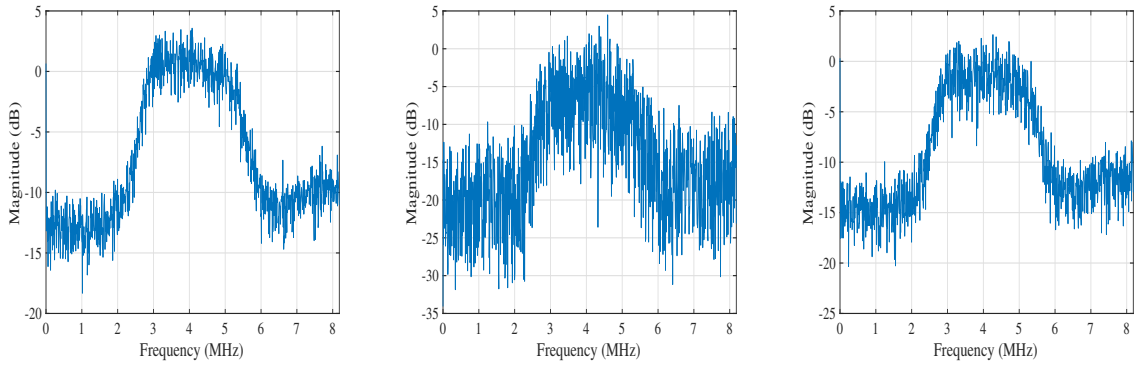

(a) Original signal (b) 10% sampling ratio (c) 50% sampling ratio

Figure 3.1: Frequency domain plot of original and reconstructed signal

$$NMSE = \frac{\|\widehat{x} - x\|_2^2}{\|x\|_2^2} \tag{3.8}$$

where $\widehat{x}$ is the recovered signal and x is the original signal. The signal reconstruction is presented for 10% and 50% sampling ratio with DCT as sparsifying and Toeplitz as the measurement matrix as shown in Fig. 3.1.

The performance of the DCT and DWT sparsifying matrix is compared in terms of NMSE at different sampling ratios for the Toeplitz, Bernoulli and Gaussian measurement matrix. One of the case with toeplitz matrix is presented in Fig. 3.2. It is observed that the NMSE of the DCT sparsifying matrix is less than that of the DWT matrix, which states that the DCT matrix is performing better than the DWT matrix.

Similarly, the performance of Toeplitz, Bernoulli and Gaussian measurement matrix is evaluated as shown in Fig. 3.3. The performance of the Toeplitz measurement matrix is better as compared to the Bernoulli and Gaussian matrix in terms of signal reconstruction. Hence, it is concluded that DCT as the sparsifying matrix with Toeplitz as the measurement matrix has better results over the other sparsifying and measurement matrix.

Additionally, after performing the frequency-domain correlation of the reconstructed data with the locally generated GPS/NavIC code (depending on the data used), the same satellite PRN i.e. PRN 24 and code delay is found as detected for the original data. The frequency domain acquisition for the original and reconstructed GPS data for satellite PRN 24 is presented in Fig.3.4

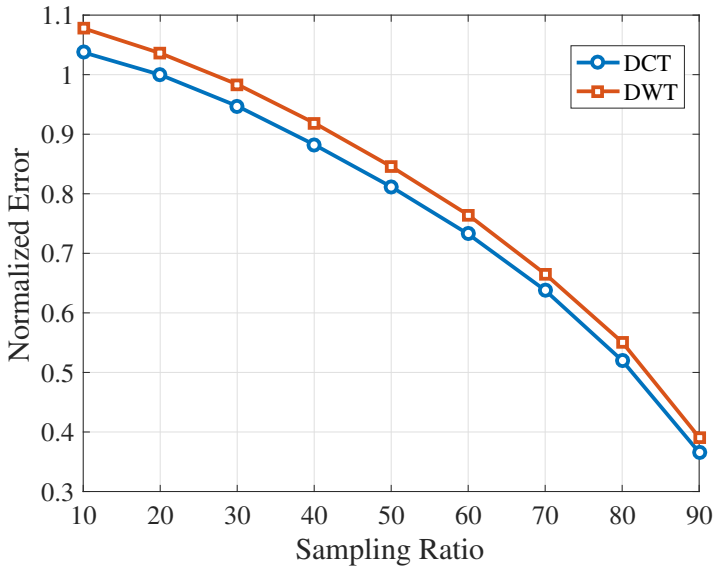

Figure 3.2: Comparison between DCT and DWT sparsifying matrix for different sampling ratio.

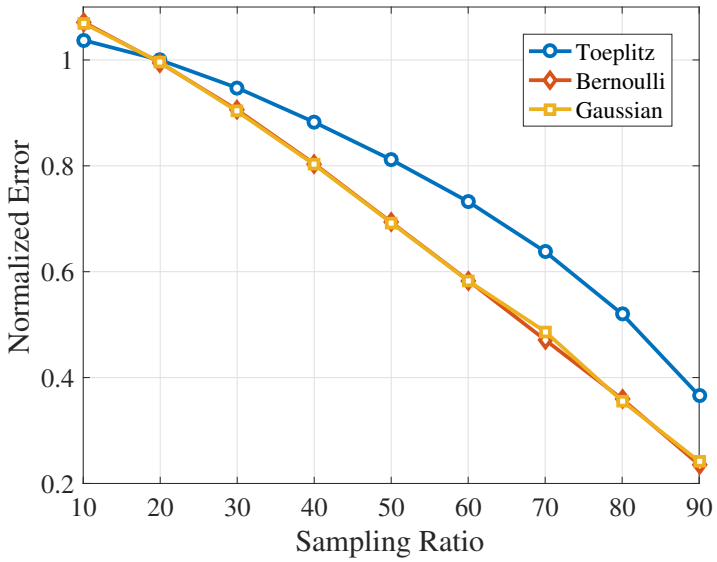

Figure 3.3: Comparison between Toeplitz, Bernoulli and Gaussian measurement matrix for different sampling ratio.

and Fig.3.5 respectively. The reconstructed data is obtained from the 40% sampling ratio. It is evident from Fig. 3.5, that it is feasible to perform satellite signal acquisition using the compressed and reconstructed data set and further perform reflectometry analysis.

For reflectometry application, the DDMs of two NavIC data sets for different surface properties are generated. For two different surface properties, two dielectric constants, i.e. 5 and 20, are considered, which represent a dry soil and a smooth surface, respectively. Now, according to the bi-static radar equation [19], the coherent power levels for two different surfaces will vary

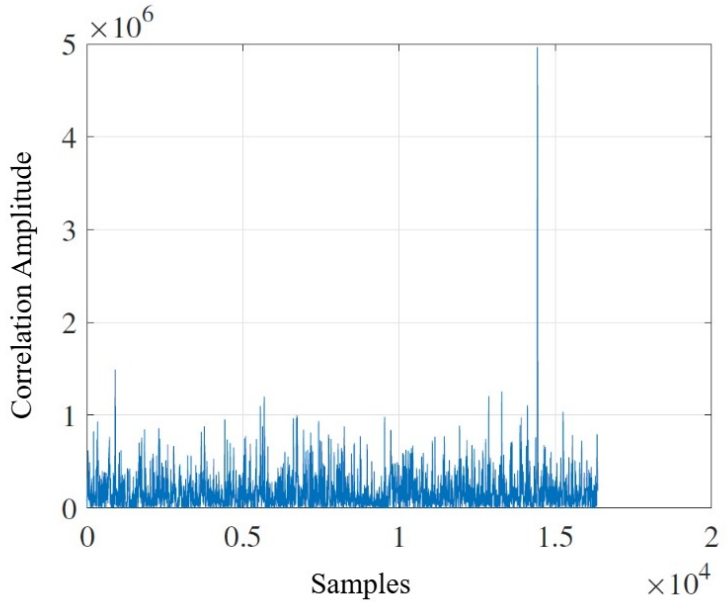

Figure 3.4: Frequency domain acquisition for the Original GPS data.

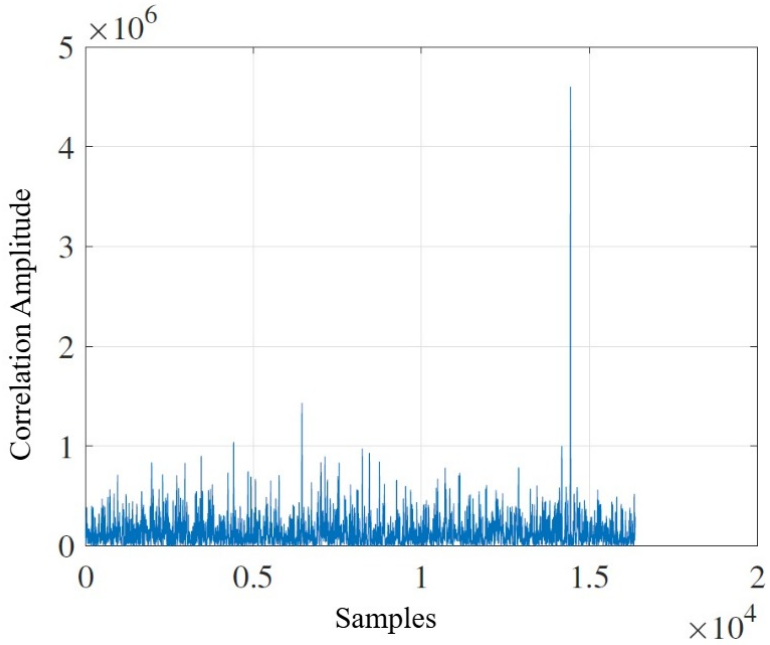

Figure 3.5: Frequency domain acquisition for the Reconstructed GPS data.

depending on the surface properties. The DDMs for two different NavIC data sets are presented in Fig.3.6a and Fig.3.7a. The correlation power levels of the DDM show variation depending on the surface properties. The correlation peak of DDM for dielectric constant 5 is less compared to the correlation peak for dielectric constant 20. Moreover, the DDMs of the data, which are reconstructed using the proposed algorithm, also show the variation in the correlation power. The DDMs of the reconstructed data for both the dielectric constant are presented in Fig.3.6b and

Fig.3.7b. The experimental results of DDMs obtained from the original and reconstructed data set are summarized in the Table.3.1

Table 3.1: Change in correlation peak with different surface dielectric constant

Dielectric Constant	**Correlation peak (Original Data Set)**	**Correlation Peak (Reconstructed Data set)**
5	2848	476.8
20	4176	849.9

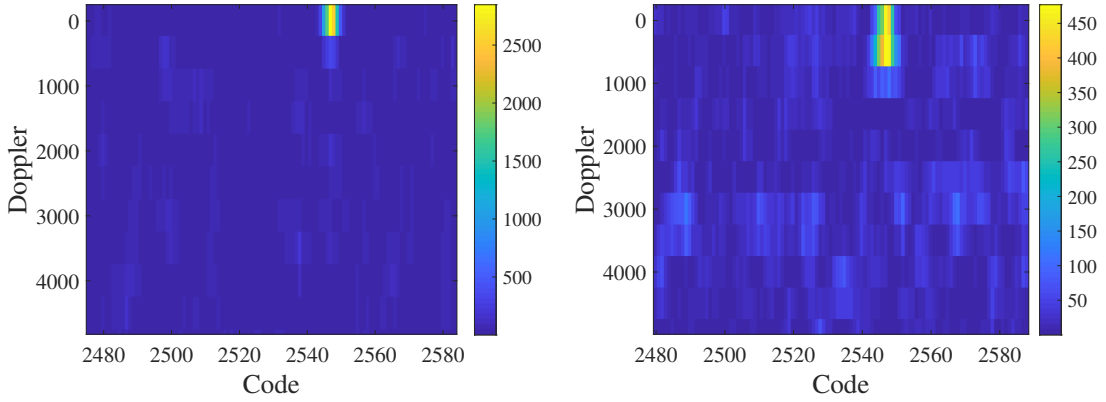

(a) Original Data (b) Reconstructed Data

Figure 3.6: DDM for the multi-path NavIC signal for Dielectric Constant 5

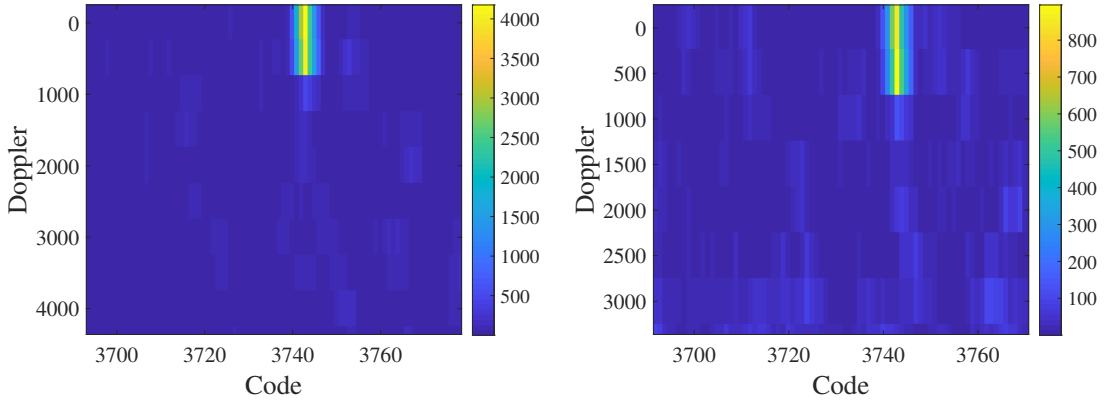

(a) Original Data (b) Reconstructed Data

Figure 3.7: DDM for the multi-path NavIC signal for Dielectric Constant 20

The results presented in Fig.3.6 and Fig.3.7 implies that the similar variations in correlation power can be achieved with the reconstructed GNSS signal using 60% sampling ratio as shown by the original GNSS signal DDMs. Hence, only few significant GNSS data samples can be

transmitted and then reconstructed at receiver's end for further processing.

3.4 Conclusion

In this work, the BPDN (Basis Pursuit De-Noising) convex optimization algorithm, a key component of compressive sensing theory, is applied to GNSS signals to address the challenge of handling large datasets while maintaining signal integrity. Experimental results highlight significant findings regarding the performance of different sparsifying and measurement matrices. Specifically, the Discrete Cosine Transform (DCT) matrix outperforms the Discrete Wavelet Transform (DWT) matrix in terms of sparsification, demonstrating better efficiency in compressing the GNSS signal. For measurement matrices, among the three tested—Toeplitz, Bernoulli, and Gaussian—the Toeplitz matrix exhibits superior performance in terms of reconstruction accuracy. Thus, a combination of the DCT sparsifying matrix and the Toeplitz measurement matrix is identified as the optimal configuration for compressing GNSS signals effectively.

The robustness of this algorithm extends to noisy environments. This has been validated by introducing noise into the original signal and then reconstructing it using the same compressive sensing framework. The reconstructed signal retains high fidelity, demonstrating the algorithm's capability to perform well even under noisy conditions. Moreover, the acquisition of satellite signals from the reconstructed data has been performed using a frequency-domain correlation technique. The same satellite PRN codes detected in the original direct signal are successfully identified in the reconstructed signal, confirming the algorithm's effectiveness in preserving key satellite acquisition parameters. Additionally, this study investigates the potential of the reconstructed data for generating Delay-Doppler Maps (DDMs) and analyzing surface properties. The DDMs generated from the reconstructed data enable the differentiation of two surface properties characterized by their dielectric constants. This finding suggests that the algorithm can capture subtle variations in surface characteristics, making it potentially useful for remote sensing applications such as soil moisture estimation and land surface characterization.

However, further research is essential to validate and generalize this algorithm for diverse

surface properties and broader environmental conditions. Future studies should focus on testing the algorithm across a wider range of surface types, including varying roughness levels, moisture content, and dielectric properties, to fully assess its applicability. Additionally, optimizing the computational efficiency of the algorithm for real-time implementation and expanding its capabilities to handle multi-constellation and multi-frequency GNSS signals would further enhance its utility in GNSS-Reflectometry and related remote sensing applications. This work lays a strong foundation for advancing signal processing techniques in GNSS-R and highlights the potential for compressive sensing theory to address critical challenges in large-scale data handling.

Chapter 4

Target localisation using GNSS-R and Doppler bound calculation for NavIC-L5

Contents

4.1 Introduction

The Global Navigation Satellite System (GNSS) constellations are initially developed for precise Positioning, Navigation and Timing (PNT) services. The GNSS receivers majorly use the direct satellite signal for the PNT applications. However, the development of the GNSS-Reflectometry (GNSS-R) technique [55, 13], which utilises the earth-reflected multipath signals, has given rise to a wide range of remote sensing applications. In GNSS-R, the earth-reflected signals are utilised in a bistatic-radar scenario to study the geophysical properties of the underlying Earth's surface.

The GNSS-R technique has been widely utilized for remote sensing applications such as soil moisture estimation [17], sea state monitoring [161], snow depth measurement [109], vegetation growth analysis [68], and altimetry [12]. The use of Delay-Doppler Maps (DDM) [1] has gained attention for extracting physical properties of the Earth's surface. Beyond environmental monitoring, GNSS-R has demonstrated significant potential for target detection and localization. Additionally, it has been experimentally proved [133, 132, 131] that the GNSS signals can also be used for target detection and localization by receiving the GNSS signals in a multi-static or bi-static radar configuration. It is feasible to detect the target by using observations from a single transmitter and receiving it using a single receiver. Target localization [162, 21] using GNSS-R can be realized by obtaining signals from multiple transmitting satellites and receiving them using a single receiver. Also, the existing GNSS and RNSS constellations guarantee that at least 4 satellites are present at the same time, illuminating the same area. Therefore, a single receiver capable of receiving the multi-frequency GNSS [163, 164] signal can form a multi-static radar system. The availability of a greater number of observations can significantly improve the target detection and localization performance. In a multi-static GNSS-R system, the target location can be estimated if the bistatic ranges and the coordinates of the transmitters and the receiver are known. This approach enables real-time target tracking, making GNSS-R a viable technique for applications such as maritime surveillance, search and rescue operations, and defence-related monitoring.

Now, before processing the satellite signal for remote sensing or target tracking and localisation application, satellite signal acquisition and an estimate of Doppler frequency and the code delay are necessary. In order to get the navigation information and estimates of code delay

and Doppler shift from the GNSS signal, a signal acquisition algorithm must be implemented. The signal acquisition detects the satellite PRN code in the received signal and estimates code delay and Doppler frequency related to the detected satellite. The signal acquisition is a 2D search problem where the satellite code delay and Doppler frequency are searched by correlating the incoming satellite signal with the locally generated C/A code over a given range of code delay and Doppler frequency shift. Hence, the Doppler frequency bound is an essential parameter that needs to be defined during the signal acquisition process. The theoretically calculated Doppler frequency search range for GPS satellite signal acquisition is ±5kHz, and ±10kHz [139], for the static and moving GPS receiver scenarios. In the signal acquisition process, the Doppler range needs to be defined in order to cover all the expected Doppler frequency changes. The Doppler frequency range for the GPS signal is already defined, whereas the Doppler range for NavIC-L5 multipath signal acquisition has not yet been studied.

In this chapter, the Doppler frequency bound for NavIC-L5 multipath satellite signal acquisition is estimated. It will help in fast signal acquisition while performing satellite signal analysis for target-tracking or reflectometry applications. This research work provides a methodology for calculating the Doppler search range based on the reflection points, transmitter and receiver's position and velocity. The bound of Doppler frequency depends on the transmitter and receiver's velocity and position. The NavIC-L5 satellite velocity and related parameters, including the elevation angle of all the NavIC-L5 transmitting satellites with different surface points, are simulated using the STK software. The Doppler bound is calculated for NavIC multipath signal acquisition, considering both the static and moving receiver scenario. The variation of Doppler bound based on the location (i.e. latitude and longitude) of the receiver is also presented in this work. The processing time and performance comparison are carried out based on the Doppler bound calculated. The signal acquisition time has been significantly reduced by 70% and 60% for static and moving receiver scenarios, respectively, based on the calculated Doppler frequency bound. Further, the calculated Doppler bound is used to generate the Range-Doppler maps for target localisation and tracking applications. This work presents the target localisation using the GNSS-R technique. The target location is determined by optimizing three sets of bistatic ranges obtained from multiple GNSS transmitters and a single receiver. The key observation for target lo-

calisation is the difference between the direct signal path and the reflected multipath length, which is also called the Bistatic Range. The calculated Doppler bound is integrated with GNSS-R based target localisation in order to reduce the processing time for Range-Doppler (RD) Map generation.

The rest of the chapter is organized as follows: we have first introduced the theoretical concepts and methodology for Doppler bound calculation in Section II. The Range-Doppler map generation and PDOP analysis are explained in Section III. The Doppler frequency bounds calculated for the static and moving receiver scenario and Range-Doppler maps are presented in Section IV. Section V concludes the paper with discussions on the estimated Doppler frequency bound and target location accuracy analysis using the GNSS multipath signal.

4.2 Doppler Frequency Range for NavIC-R

While receiving a satellite signal for a reflectometry application, a Doppler shift occurs, which is caused by the motion of the transmitter relative to the receiver. The basic transmitter-surface-receiver geometry is shown in Fig.4.1. The receiver (Rx.) is placed at height h from the ground and has a velocity V_r, as shown in Fig.4.1. The receiver moves in the (x, y) plane with velocity component V_{rx} and V_{ry} in the x and y direction. The transmitting satellite (Tx.) is the NavIC satellite, which is placed in a geostationary (GEO) and geosynchronous (GSO) orbit.

During the satellite signal acquisition, the acquisition algorithm estimates the satellite code delay and Doppler frequency by searching through a range of Doppler frequencies and code delay.

Therefore, the Doppler frequency shift experienced at various surface target points within the NavIC service area is calculated in order to define the maximum and minimum Doppler shift bound for performing signal acquisition. The bound on the Doppler frequency shift differs for the static and the moving receiver scenario and is studied for both cases. Considering the flat-earth scenario, the Doppler shift $f_{d,xy}$ associated to surface point (x, y) is mathematically defined as

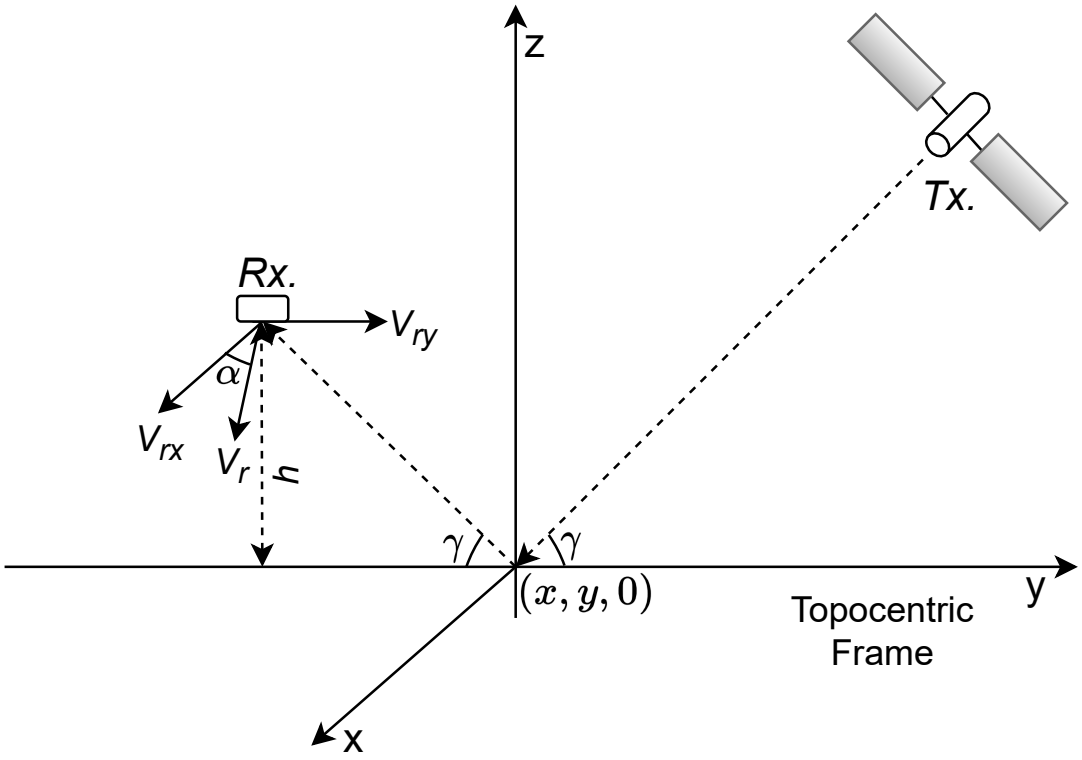

Figure 4.1: Basic GNSS signal reception geometry.

[140]:

$$f_{d,xy} = [\overrightarrow{V_t}\hat{n}_i - \overrightarrow{V_r}\hat{n}_s]/\lambda = [-V_{ty}\cos\gamma - V_{tz}\sin\gamma + \frac{V_{rx}x + V_{ry}(y + \frac{h}{\tan\gamma}) + V_{rz}h}{\sqrt{x^2 + (y + \frac{h}{\tan\gamma})^2 + h^2}}]/\lambda \tag{4.1}$$

where $\overrightarrow{V}_t$, $\overrightarrow{V}_r$ are the transmitter and receiver velocity and $\hat{n}_i$, $\hat{n}_s$ are the unit vectors in the incident and scattering directions. The GNSS signal wavelength is denoted by λ. V_{ty} and V_{tz} are the transmitter velocity in the y and z direction. The x and y are the surface target point coordinates. The receiver is at height h from the earth's surface, having a velocity component as V_{rx}, V_{ry}, V_{rz} in x, y, z direction and γ is the elevation angle. The Doppler frequency bound defined in the acquisition algorithm is a function of transmitting satellite velocity, the receiver's velocity and position or the location of the surface target point. All the NavIC transmitting satellites in geosynchronous and geostationary orbit are used for studying the Doppler bound. The Doppler shift values at a particular surface target point are calculated corresponding to all seven NavIC transmitting satellites, and then the maximum and minimum Doppler values for that particular surface target point are selected.

Now, a grid-based analysis is performed to calculate the Doppler frequency bound. The surface target point is fixed for the grid-based analysis, and the transmitter position is varied for 24 hours. The 72 grid-points are taken within the NavIC service area. The 72 surface target points are uniformly distributed with a Longitude range from 60° to 100° and a Latitude range of 5° to 40° with a spacing of 5° in both latitude and longitude axis. The simulation is performed in STK software to extract the relevant parameters, including the NavIC transmitting satellite velocity and elevation angle. The elevation angle for all the surface points with respect to all the NavIC transmitting satellites is simulated using the STK and is further used to calculate the Doppler frequency bound. This work considers 72 surface target points within the NavIC service area. The surface target points in a grid-based scenario and the transmitting NavIC satellites are shown in Fig. 4.2. The Doppler frequency bound is calculated for both the static receiver scenario and the moving receiver scenario with the receiver placed on a Unmanned Aerial Vehicle (UAV) and a Low Earth Orbit (LEO) satellite.

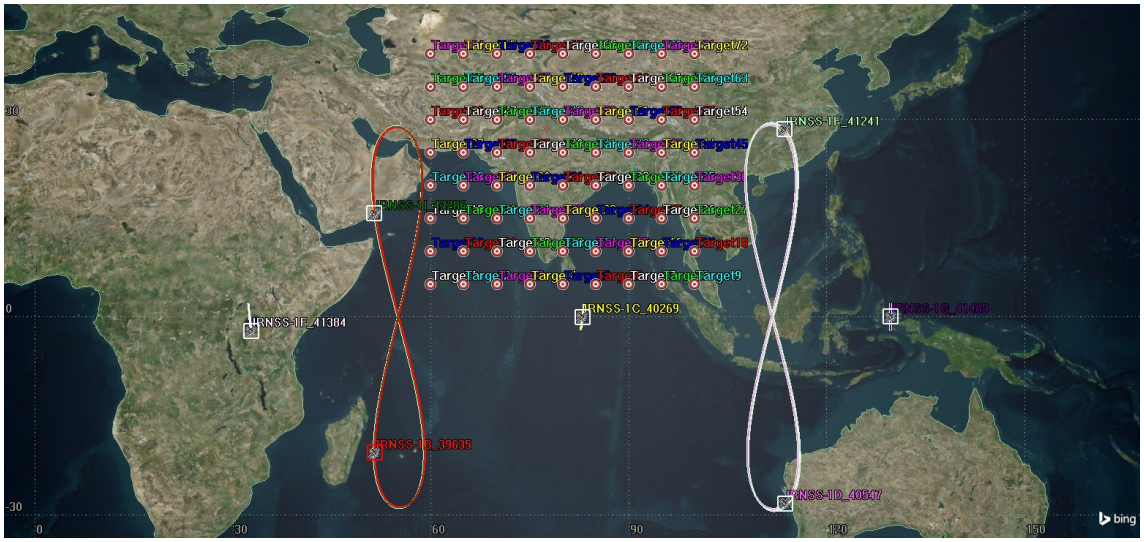

Figure 4.2: Surface target points location.

4.2.1 Static Case:

The Doppler frequency for the static receiver scenario is calculated using (4.1) and taking the receiver velocity components as zero. Hence, (4.1) can be written as:

$$f_{d,xy} = [-V_{ty}.\cos\gamma - V_{tz}.\sin\gamma]/\lambda \tag{4.2}$$

The maximum and minimum Doppler frequency associated with all the target points and the NavIC transmitting satellites is calculated using (4.2). The maximum and minimum values of Doppler for a particular surface point are selected from the Doppler values obtained corresponding to all 7 satellites. Based on the maximum and minimum Doppler values related to all the target points, the Doppler frequency bound for the static receiver case is defined.

4.2.2 Dynamic case:

Now, considering the moving receiver scenario, we have to calculate the maximum and minimum components of receiver velocity to get the maximum and minimum bound of Doppler frequency. The surface point defined in (4.1) can be represented in terms of latitude (Φ) and longitude (Θ) as follows:

$$x = R\cos\Phi\cos\Theta \tag{4.3}$$

$$y = R\cos\Phi\sin\Theta \tag{4.4}$$

where R is the radius of the Earth. The velocity components of the receiver in the x and y directions are represented as :

$$V_{rx} = V\cos\alpha \tag{4.5}$$

$$V_{ry} = V\sin\alpha \tag{4.6}$$

where V is the magnitude of receiver velocity.

Now substituting, x, y, V_{rx}, V_{ry} in (4.1),

$$f_{d,xy} = [-V_{ty}\cos\gamma - V_{tz}\sin\gamma + \frac{V\cos\alpha(R\cos\Phi\cos\Theta)}{R_{rx,s}} + \frac{V\sin\alpha(R\cos\Phi\sin\Theta + \frac{h}{\tan\gamma})}{R_{rx,s}} + \frac{V_{rz}h}{R_{rx,s}}]/\lambda \tag{4.7}$$

where $R_{rx,s}$ is defined as :

$$R_{rx,s} = \sqrt{(R\cos\Phi\cos\Theta)^2 + (R\cos\Phi\sin\Theta + \frac{h}{\tan\gamma})^2 + h^2} \tag{4.8}$$

Now, differentiating (4.7) with respect to α

$$\frac{df_d}{d\alpha} = \frac{1}{R_{rx,s}\lambda}[-V\sin\alpha(R\cos\Phi\cos\theta) + V\cos\alpha(R\cos\Phi\sin\Theta + \frac{h}{\tan\gamma})] \tag{4.9}$$

equating (4.9) to zero, we get :

$$\alpha = \tan^{-1}\left[\frac{R\cos\Phi\sin\Theta + (\frac{h}{\tan\gamma})}{R\cos\Phi\cos\Theta}\right] \tag{4.10}$$

In (4.10), considering h to be small compared to the radius of Earth, therefore :

$$\alpha = \tan^{-1}[\tan\Theta]$$

$$\alpha = \Theta \tag{4.11}$$

After calculating the second derivative of (4.9), the value of f_d is $\pm\frac{V}{R_{rx,s}\lambda}R\cos\Phi$ for $\alpha = 180{+}\Theta$ and Θ, respectively. So, it is concluded that for a particular surface target point, the receiver's velocity component angle α should be equal to the longitude Θ and $180 + \Theta$, respectively, for maximum and minimum values of Doppler frequency. By taking the α equal to the longitude Θ and $180° + \Theta$, the maximum and minimum Doppler frequency is calculated for the corresponding surface target point. The procedure followed for estimating the Doppler frequency bound is summarised in the Algorithm 2.

Algorithm 2: Doppler frequency calculation for a specific target point

Input: $V_{ty}, V_{tz}, V_{rx}, V_{ry}, V_{rz}, \Phi, \Theta$
Output: $f_{d,max}, f_{d,min}$
if *Static Receiver* **then**
  Calculate $f_{d,max}$ and $f_{d,min}$ using (4.2)
else
  Calculate $f_{d,max}$ using (4.7) with $\alpha = \Theta$
  Calculate $f_{d,min}$ using (4.7) with $\alpha = 180{+}\Theta$

4.3 Target Localisation using GNSS-R and Accuracy Analysis

The bistatic range obtained using the multi-static GNSS-R configuration can be used for target localisation. The bistatic range is defined as the difference between the direct and the reflected path length. The bistatic range is then used in least square optimisation to perform target localisation. The bistatic range-based target localisation is shown in Fig. 4.3.

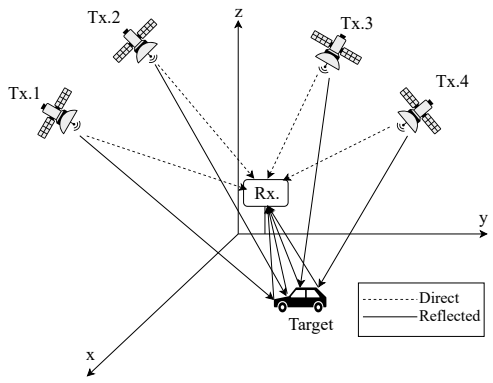

Figure 4.3: Bistatic range-based target localisation

This system consists of multiple GNSS satellites as the transmitter and a single receiver capable of receiving both direct and reflected signals. Now, in order to localize the ECEF coordinates of a target point, 3 sets of observations are needed. The availability of 3 transmitting satellites is checked for a particular receiver location at a given instant of time. The elevation angle variation of all the 7 NavIC satellites for 24 hours at an interval of 10 minutes is shown in Fig. 4.4. The three satellites having elevation angles in the range of 30° to 32° are selected for target localisation using GNSS-R. The bistatic ranges are calculated between each transmitter and the receiver. The obtained bistatic ranges are used as observations in order to perform the target localisation. The bistatic range is defined as the difference between the direct and reflected path

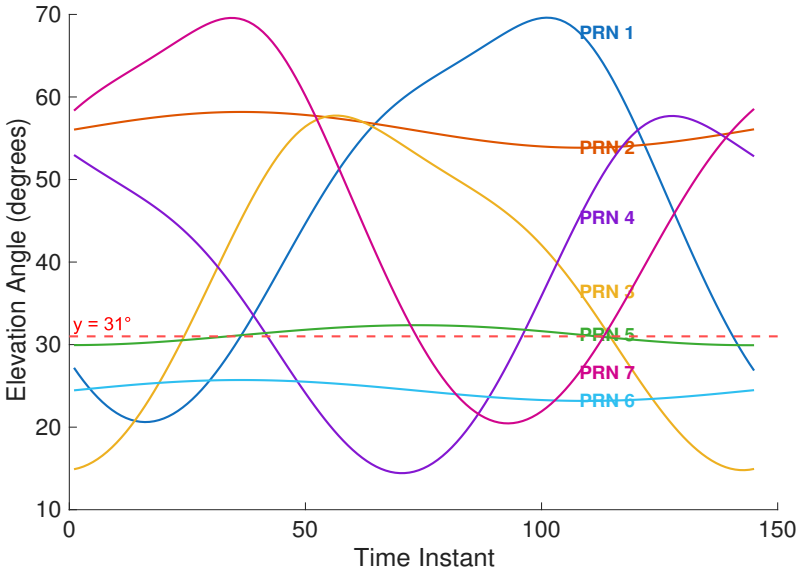

Figure 4.4: Elevation angle of 7 NavIC satellites for 24 hrs.

length. The direct, reflected path lengths and bistatic range are defined as:

$$direct: \ \|T - R\| \tag{4.12}$$

$$reflected: \ \|T - S\| + \|R - S\| \tag{4.13}$$

$$bistatic\ range\ (b_r) : (\|T - S\| + \|R - S\|) - (\|T - R\|) \tag{4.14}$$

Where $T(T_x, T_y, T_z)$, $S(S_x, S_y, S_z)$ and $R(R_x, R_y, R_z)$ are the transmitters, target point, and receiver location in the ECEF coordinate.

The optimisation of the bistatic range for target localisation can be written as follows:

$$\hat{s} = \underset{s}{arg\ min}\ [\hat{b_r} - b_r] \quad subject\ to\ \sqrt{S_x^2 + S_y^2 + S_z^2} = r_e \tag{4.15}$$

where $\hat{b_r}$ is the estimated bistatic range obtained from the range-doppler map, and b_r is the true bistatic range, r_e is the radius of Earth. The above optimization equation is used to estimate the target point coordinates $S(S_x, S_y, S_z)$. The constraint $\sqrt{S_x^2 + S_y^2 + S_z^2} = r_e$ is used to satisfy the condition that the estimated target point lies on the surface of Earth. After the target point is calculated, the DOP analysis is performed for accuracy analysis. For DOP calculation, the **G** matrix needs to be calculated, the **G** matrix is defined as:

$$\mathbf{G} = (\mathbf{H}^T\mathbf{H})^{-1}$$

where $\mathbf{H}$ is the measurement Jacobian matrix. For the n satellite in view, $\mathbf{H}$ matrix is an nx3 matrix, in which each term represents the direction vector between the transmitter, target point and receiver.

The pseudo-range for reflected path length used for $\mathbf{H}$ matrix is expressed as:

$$\rho_j = \sqrt{(T_{xj} - S_x)^2 + (T_{yj} - S_y)^2 + (T_{zj} - S_z)^2} + \sqrt{(S_x - R_x)^2 + (S_y - R_y)^2 + (S_z - R_z)^2} \tag{4.16}$$

The approximate pseudo-range is written as :

$$\hat{\rho_j} = \sqrt{(T_{xj} - \hat{S_x})^2 + (T_{yj} - \hat{S_y})^2 + (T_{zj} - \hat{S_z})^2} + \sqrt{(\hat{S_x} - R_x)^2 + (\hat{S_y} - R_y)^2 + (\hat{S_z} - R_z)^2} \tag{4.17}$$

The $\mathbf{H}$ matrix used for the DOP is defined as a function of the bistatic range and written as:

$$H = \begin{bmatrix} -(\frac{T_{x1}-S_x}{r_{t1}}) + (\frac{S_x-R_x}{r_r}) & -(\frac{T_{y1}-S_y}{r_{t1}}) + (\frac{S_y-R_y}{r_r}) & -(\frac{T_{z1}-S_z}{r_{t1}}) + (\frac{S_z-R_z}{r_r}) \\ -(\frac{T_{x2}-S_x}{r_{t2}}) + (\frac{S_x-R_x}{r_r}) & -(\frac{T_{y2}-S_y}{r_{t2}}) + (\frac{S_y-R_y}{r_r}) & -(\frac{T_{z2}-S_z}{r_{t2}}) + (\frac{S_z-R_z}{r_r}) \\ \vdots & \vdots & \vdots \\ -(\frac{T_{xn}-S_x}{r_{tn}}) + (\frac{S_x-R_x}{r_r}) & -(\frac{T_{yn}-S_y}{r_{tn}}) + (\frac{S_y-R_y}{r_r}) & -(\frac{T_{zn}-S_z}{r_{tn}}) + (\frac{S_z-R_z}{r_r}) \end{bmatrix} \tag{4.18}$$

now for n number of satellite observations H and H^T are written as:

$$H = \begin{bmatrix} H_{11} & H_{12} & H_{13} \\ H_{21} & H_{22} & H_{23} \\ \vdots & \vdots & \vdots \\ H_{n1} & H_{n2} & H_{n3} \end{bmatrix} \tag{4.19}$$

$$H^T = \begin{bmatrix} H_{11} & H_{21} & \cdots & H_{n1} \\ H_{12} & H_{22} & \cdots & H_{n2} \\ H_{13} & H_{23} & \cdots & H_{n3} \end{bmatrix} \tag{4.20}$$

Let's compute $G = (H^T H)^{-1}$, which is further used for the calculation of PDOP.

$$G = (H^T H)^{-1} = \begin{bmatrix} \sum_{i=1}^{n} (H_{i1})^2 & \sum_{i=1}^{n} H_{i1}H_{i2} & \sum_{i=1}^{n} H_{i1}H_{i3} \\ \sum_{i=1}^{n} H_{i1}H_{i2} & \sum_{i=1}^{n} (H_{i2})^2 & \sum_{i=1}^{n} H_{i2}H_{i3} \\ \sum_{i=1}^{n} H_{i1}H_{i3} & \sum_{i=1}^{n} H_{i2}H_{i3} & \sum_{i=1}^{n} (H_{i3})^2 \end{bmatrix}^{-1} \tag{4.21}$$

where n is the number of transmitters and H_{i1}, H_{i2} and H_{i3} are as follows:

$$H_{i1} = -(\frac{T_{xi} - S_x}{r_{ti}}) + (\frac{S_x - R_x}{r_r}) \tag{4.22}$$

$$H_{i2} = -(\frac{T_{yi} - S_y}{r_{ti}}) + (\frac{S_y - R_y}{r_r}) \tag{4.23}$$

$$H_{i3} = -(\frac{T_{zi} - S_z}{r_{ti}}) + (\frac{S_z - R_z}{r_r}) \tag{4.24}$$

Further, representing the H_i in terms of elevation angle (E). The distance r_{ti} and r_r can be written as a function of elevation angle.

Now, the receiver and transmitter positions need to be transformed from ECEF to ENU

conversion. The following conversion matrix is used for the same:

$$A_{ENU} = \begin{bmatrix} sin(\theta) & cos(\theta) & 0 \\ sin(\phi)cos(\theta) & sin(\phi)sin(\theta) & cos(\phi) \\ cos(\phi)cos(\theta) & cos(\phi)sin(\theta) & sin(\phi) \end{bmatrix} * A_{ECEF} \tag{4.25}$$

where ϕ is latitude and θ is longitude of the reference point. Now H_{i1}, H_{i2} and H_{i3} are written as :

$$H_{i1} = -(\frac{T_{xi} - S_x}{T_{zi-enu}})sin(E) + (\frac{S_x - R_x}{R_{z-enu}})sin(E) \tag{4.26}$$

$$H_{i2} = -(\frac{T_{yi} - S_y}{T_{zi-enu}})sin(E) + (\frac{S_y - R_y}{R_{z-enu}})sin(E) \tag{4.27}$$

$$H_{i3} = -(\frac{T_{zi} - S_z}{T_{zi-enu}})sin(E) + (\frac{S_z - R_z}{R_{z-enu}})sin(E) \tag{4.28}$$

Now in ENU frame w.r.t $S(S_x, S_y, S_z)$, H_{i1}, H_{i2} and H_{i3} can be written as:

$$H_{i1} = -(\frac{T_{xi}}{T_{zi-enu}})sin(E) + (\frac{-R_x}{R_{z-enu}})sin(E) \tag{4.29}$$

$$H_{i2} = -(\frac{T_{yi}}{T_{zi-enu}})sin(E) + (\frac{-R_y}{R_{z-enu}})sin(E) \tag{4.30}$$

$$H_{i3} = -(\frac{T_{zi}}{T_{zi-enu}})sin(E) + (\frac{-R_z}{R_{z-enu}})sin(E) = -2sin(E) \tag{4.31}$$

Now evaluating $\frac{R_x}{R_z}, \frac{R_y}{R_z}$ and $\frac{T_x}{T_z}, \frac{T_y}{T_z}$ as a function of elevation (E) and receiver azimuth (A_r) angle

$$tan(E) = \frac{R_z}{\sqrt{R_x^2 + R_y^2}} \tag{4.32}$$

$$tan^2(E) = \frac{1}{(\frac{R_x}{R_z})^2 + (\frac{R_y}{R_z})^2} \tag{4.33}$$

$$(\frac{R_x}{R_z})^2 + (\frac{R_y}{R_z})^2 = \frac{1}{tan^2(E)} \tag{4.34}$$

where A_{ti} is the azimuth angle of the different transmitters with respect to the target point.

$$tan(A) = \frac{R_y}{R_z} \tag{4.35}$$

$$R_y = R_x tan(A_r) \tag{4.36}$$

$$and\ R_x = \frac{R_y}{tan(A_r)} \tag{4.37}$$

Now, substituting (24) and (25) in (22), we get:

$$\frac{R_x}{R_z} = \frac{1}{tan(E)\sqrt{1 + tan^2(A_r)}} \tag{4.38}$$

$$\frac{R_y}{R_z} = \frac{tan(A_r)}{tan(E)\sqrt{1 + tan^2(A_r)}} \tag{4.39}$$

Similarly,

$$\frac{T_x}{T_z} = \frac{1}{tan(E)\sqrt{1 + tan^2(A_{ti})}} \tag{4.40}$$

$$\frac{T_y}{T_z} = \frac{tan(A)}{tan(E)\sqrt{1 + tan^2(A_{ti})}} \tag{4.41}$$

Substituting (26), (27), (28) and (29) in (17), (18), we get:

$$H_{i1} = \frac{-cos(E)}{\sqrt{1+tan^2(A_{ti})}} + \frac{-cos(E)}{\sqrt{1+tan^2(A_r)}} \tag{4.42}$$

$$H_{i2} = \frac{-tan(A_{ti})cos(E)}{\sqrt{1+tan^2(A_{ti})}} + \frac{-tan(A_r)cos(E)}{\sqrt{1+tan^2(A_r)}} \tag{4.43}$$

$$H_{i3} = -2 * sin(E) \tag{4.44}$$

In the above equation, H_{i1}, H_{i2} and H_{i3} are represented as a function of elevation and azimuth angle only.

The PDOP is further calculated from the G Matrix as:

$$PDOP = \sqrt{G_{11} + G_{22} + G_{33}} \tag{4.45}$$

G_{11}, G_{22}, and G_{33} are the diagonal terms of the **G** matrix given by (4.21). The **G** matrix can be calculated using the elevation and azimuth angle of the receiver and the corresponding azimuth angle of the transmitter while performing the target localisation using the GNSS-R concept. The elevation angle remains the same for all three different pairs of the transmitter, target point and receiver. Meanwhile, the transmitter and receiver azimuth angles will be different for these three pairs. Hence, the PDOP can be calculated by using the experimental values of azimuth and elevation angle. After PDOP calculation, the bistatic range optimisation is also performed for the target location estimation. The algorithm for the bistatic range optimisation is as follows:

4.4 Analysis and Results

The Doppler frequency bound that is required during the signal acquisition process is estimated in this section. The calculation is performed for two scenarios: the static receiver and the moving receiver platform. In the static receiver scenario, the velocity of the receiver is considered zero,

Algorithm 3: Bistatic Range optimisation for Specular Point Estimation

Input: Receiver position $\mathbf{R} = [x_R, y_R, z_R]$;
True specular point $\mathbf{C}_{\text{true}} = [x_C^{\text{true}}, y_C^{\text{true}}, z_C^{\text{true}}]$;
Initial guess $\mathbf{C}_0$;
Fixed transmitter positions $\mathbf{T}_i$ for $i = 1, \ldots, 4$;
Measurement noise standard deviation σ;
Number of timesteps N;
Number of Monte Carlo runs M;
Maximum iterations, convergence tolerance.
Output: Mean estimation errors for x, y, and z at each timestep.
for $m = 1$ **to** M **do**
    Initialize $\mathbf{C}_{\text{est}} = \mathbf{C}_0$;
    for $t = 1$ **to** N **do**
        Compute direct path: $d_i^{\text{direct}} = \|\mathbf{T}_i - \mathbf{R}\|$;
        Compute reflected path: $d_i^{\text{reflected}} = \|\mathbf{T}_i - \mathbf{C}_{\text{true}}\| + \|\mathbf{C}_{\text{true}} - \mathbf{R}\|$;
        True bistatic range: $b_i^{\text{true}} = d_i^{\text{reflected}} - d_i^{\text{direct}}$;
        Add noise: $b_i^{\text{obs}} = b_i^{\text{true}} + \mathcal{N}(0, \sigma^2)$;
        repeat
            Compute estimated direct and reflected distances using $\mathbf{C}_{\text{est}}$;
            $b_i^{\text{est}} = d_i^{\text{reflected(est)}} - d_i^{\text{direct}}$;
            Residual: $r_i = b_i^{\text{obs}} - b_i^{\text{est}}$;
            Build Jacobian J;
            Update: $\Delta = (J^T W J)^{-1} J^T W \mathbf{r}$;
            $\mathbf{C}_{\text{est}} \leftarrow \mathbf{C}_{\text{est}} + \Delta$;
        until *convergence*;
        Save $\mathbf{C}_{\text{est}}$ for timestep t;
Compute estimation errors: ϵ_x, ϵ_y, ϵ_z;
Compute mean estimation errors over all runs.

and hence (4.1) can be written as:

$$f_{d,xy} = [-V_{ty} \cos\gamma - V_{tz} \sin\gamma]/\lambda \tag{4.46}$$

The Doppler bound for all the target point (x, y) as shown in Fig. 4.2 is calculated w.r.t all the NavIC transmitting satellites using (4.46). The maximum values of Doppler frequency for different longitudes with varying latitudes are shown in Fig.4.5a, and the maximum Doppler frequency observed is 460 Hz. Similarly, the minimum values of the Doppler frequency variation over all the target points are shown in Fig. 4.5b. The minimum frequency bound observed is -540 Hz. Hence, as observed from Fig. 4.5a and Fig. 4.5b, the Doppler frequency bound for the static receiver case is taken as ± 550 Hz. The 2D heatmap representation of maximum and minimum Doppler frequency values for the different latitude and longitude points within the NavIC service area are shown in Fig. 4.6a and Fig. 4.6b, respectively. The minimum and maximum Doppler values for all the considered grid points over NavIC service region are represented in Fig. 4.8.

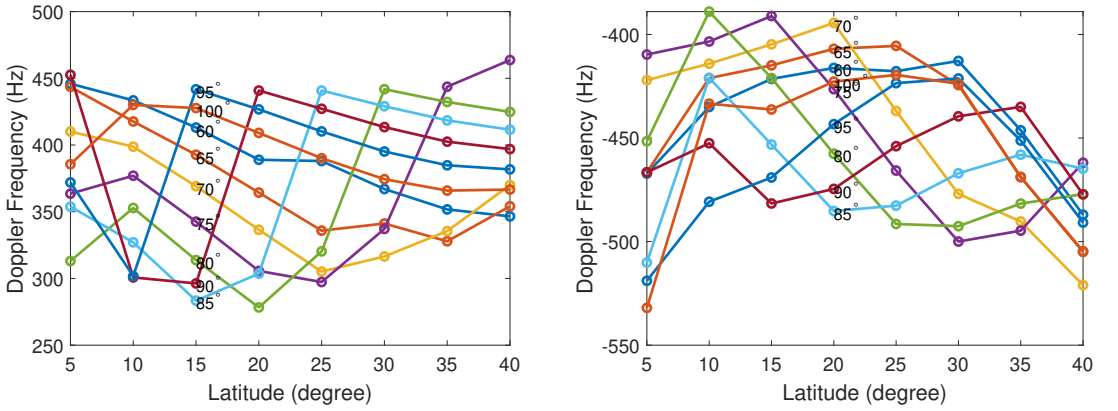

(a) Maximum Doppler Values (b) Minimum Doppler Values

Figure 4.5: Maximum and Minimum Doppler frequency values for all surface points for static receiver scenario.

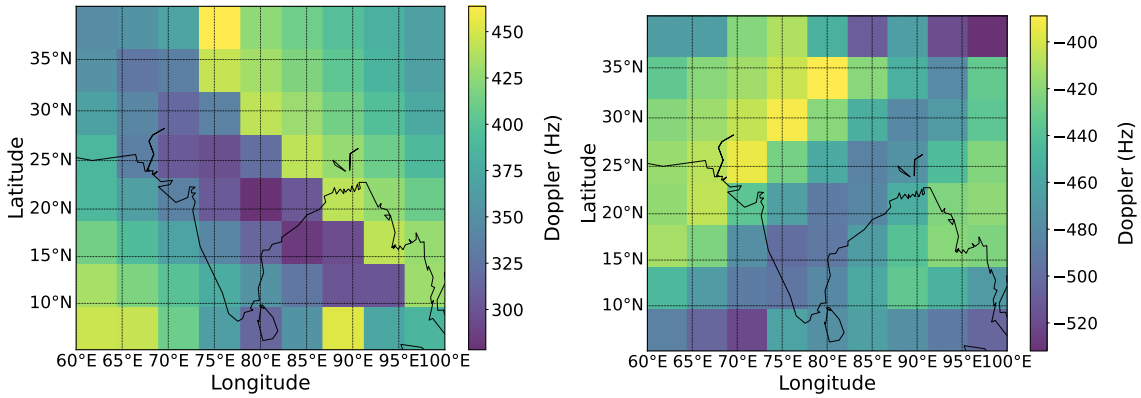

(a) Maximum Doppler Values (b) Minimum Doppler Values

Figure 4.6: Heatmap of Maximum and Minimum Doppler frequency values for all surface points for static receiver scenario.

Now, considering the moving receiver scenario, the Doppler frequency bound is calculated using (4.7), with α values equal to the longitude Θ for the maximum Doppler values and $\alpha = 180° + \Theta$ for minimum Doppler value. The Doppler frequency is calculated for two cases with the receiver placed on a Unmanned Aerial Vehicle (UAV) and Low Earth Orbit (LEO) satellite. In the case of the receiver placed on a UAV, the Doppler frequency does not change significantly with the change in receiver velocity, as the velocity of a UAV is much less compared to the velocity of the NavIC transmitter satellite in the Geostationary (GEO) and Inclined Geosynchronous orbits (IGSO). However, in the case of a receiver placed on-board a LEO satellite, the Doppler frequency depends on the receiver velocity. The LEO satellites at an altitude range from 200 Km-1000 Km have a velocity range of 7.78 Km/s - 7.35 Km/s. The maximum and minimum Doppler frequency is calculated using algorithm 2 for the receiver placed on a LEO satellite with different latitudes

and varying longitudes of the target points are shown in Fig. 4.7a and Fig. 4.7b, respectively. The Doppler shift values are calculated for a LEO altitude of 200 Km with the corresponding velocity of 7.78 Km/s.

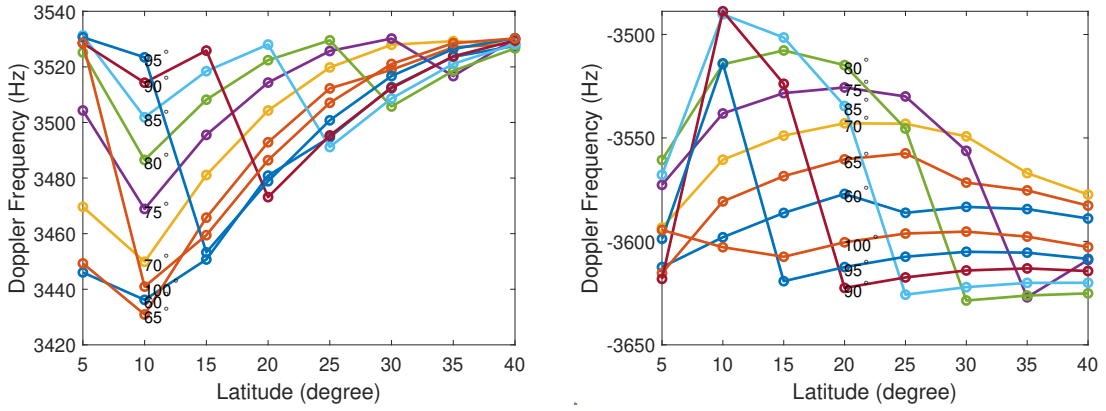

(a) Maximum Doppler Values (b) Minimum Doppler Values

Figure 4.7: Maximum and Minimum Doppler frequency values for receiver onboard LEO satellite.

From Fig. 4.7a and Fig. 4.7b, the Doppler bound for the LEO receiver scenario can be considered as ± 3.7 kHz. The 2D heatmap representation of maximum and minimum Doppler frequency values for the different latitude and longitude points for moving receiver scenario within the NavIC service area are shown in Fig. 4.8a and Fig. 4.8b, respectively. The Doppler frequency

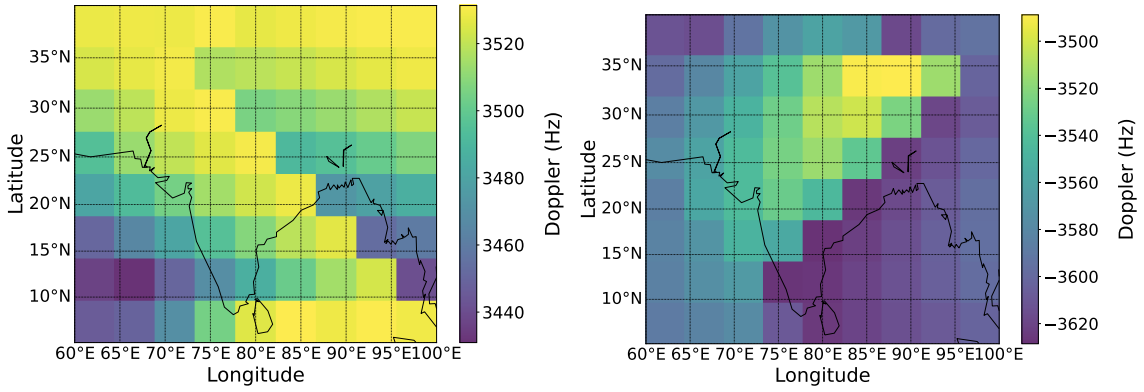

(a) Maximum Doppler Values (b) Minimum Doppler Values

Figure 4.8: Heatmap of Maximum and Minimum Doppler frequency values for receiver onboard LEO satellite.

bounds calculated for NavIC-L5 multipath satellite signals for static and moving receivers are then used in signal acquisition algorithms. The Doppler bound presented in this paper can be used for performing satellite signal acquisition for the NavIC-Reflectometry application [165]. For signal acquisition processing time comparison, the Doppler bound of ± 0.55 kHz is used for performing

Table 4.1: Signal acquisition time comparison for static receiver case.

Doppler Frequency Bound (kHz)	**Signal Acquisition Time (sec.)**
± 0.55	0.65
± 5	2.19

Table 4.2: Signal acquisition time comparison for moving receiver case for receiver onboard a LEO satellite.

Doppler Frequency Bound (kHz)	**Signal Acquisition Time (sec.)**
± 3.7	1.4
± 10	3.58

NavIC-L5 signal acquisition, and the acquisition time is 0.65 sec. It is 70% less compared to the acquisition time of 2 sec., calculated using standard ± 5kHz Doppler frequency bound, which is used for GPS satellite signal acquisition. Similarly, the signal acquisition time is calculated for the LEO receiver scenario using both the estimated Doppler bound of ± 3.7 kHz and the standard ± 10 kHz Doppler bound. The signal acquisition time for the moving receiver scenario is 1.4 sec, which is 60% less than the acquisition time of 3.58 sec for ± 10 kHz. The acquisition time calculated for different frequency bounds for static and moving receiver scenarios is presented in Table. 4.1 and Table. 4.2, respectively. The signal acquisition time reduction presented here is the average of 100 repeated trials. It will further help in resource optimisation by reducing the required number of correlators while processing a large data set for reflectometry analysis.

Once the Doppler bounds are calculated, the Range-Doppler (R-D) maps are generated using the GNSS RF signal. The NavIC-L5 RF signals are received using the SIMAC-2 GNSS simulator, including both the direct signal and the target-reflected signal. The bistatic ranges are calculated between four transmitters and a single receiver and are used as observations in least square estimation in order to estimate the target location. The noise in direct path length

is considered as 20m, and similarly, considering the same clock bias and atmosphere conditions, a noise of 20m is added to the reflected path length. Hence, the additive noise in the bistatic range is 28m. The bistatic ranges are calculated between four transmitters and a single receiver and are used as observations in least square estimation in order to estimate the target location. All the transmitter, receiver and target positions are in the ECEF coordinate system. The four transmitter coordinates in km are:

- Tx1 (-13219.83 km,38906.22 km,-9075.27 km)
- Tx2 (35484.96 km,22624.90 km,-310.25 km)
- Tx3 (20641.81 km,34165.59 km,-13776.98 km)
- Tx4 (22090.38 km,14617.84 km,3618.04 km)

The receiver coordinates in km are as follows:

- Rx (1239.26 km,5464.79 km,3038.77 km).

These bistatic ranges are used to estimate the target location using the Least square estimation method, and the norm difference between the true and estimated position is 78m, with an uncertainty of 130m and a GDOP value of 4.57. The estimation error in the x, y and z positions, along with the norm of error, is shown in Fig. 4.9. The estimation errors are presented for the Monte-Carlo simulation of 100 runs,215 and the errors are within the 100m bounds. The confidence interval analysis is also performed, and the 50(CEP) plot for the x-y, y-z and x-z planes is shown in Fig. 4.10.

The bistatic ranges for optimisation are obtained from the R-D map, developed using the received RF signal. For generating the R-D map, the signal delay of the direct signal is estimated for the synchronization. The calculated delay is used to align the noise-free PRN code. The aligned PRN code is further correlated with the received RF signal. It resulted in R-D maps with a direct signal peak at zero delays, with a multipath signal peak at the distance corresponding to the bistatic range of the target. The R-D map for an RF signal is shown in Fig. 4.11. In Fig.4.11, the

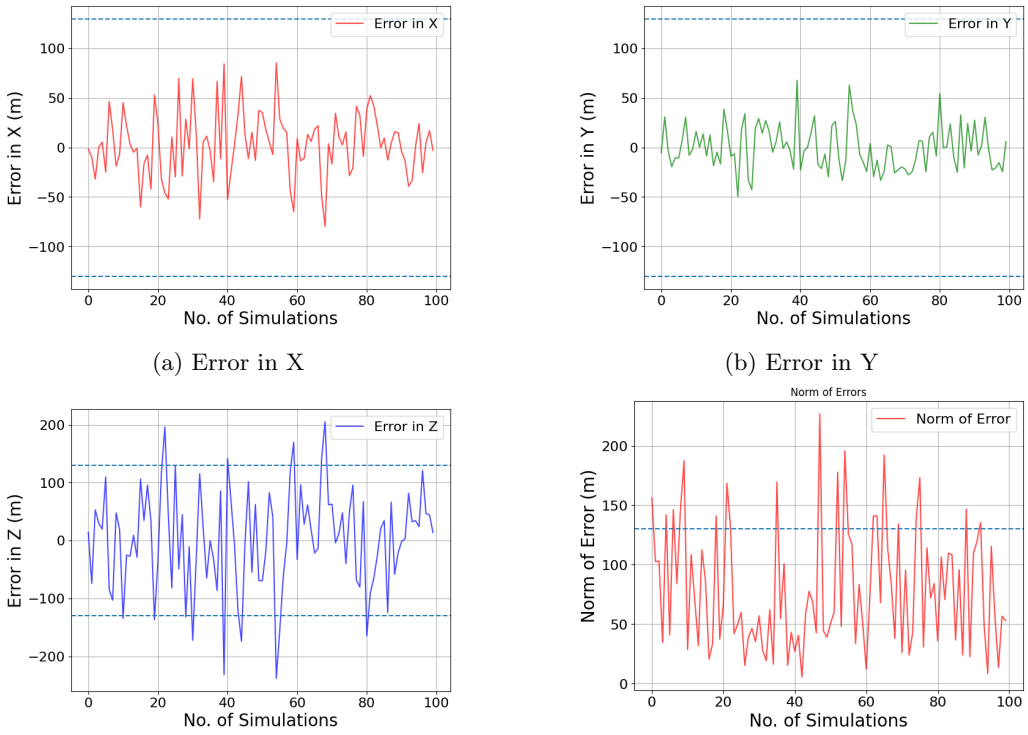

(a) Error in X

(b) Error in Y

(c) Error in Z

(d) Norm of Error

Figure 4.9: Estimation Error in Target Position

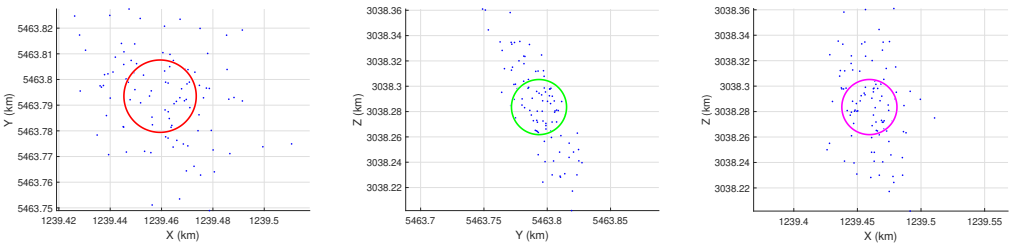

(a) CEP in x-y plane

(b) CEP in y-z plane

(c) CEP in x-z plane

Figure 4.10: Circular Error Probable Plot

corresponding bistatic range is 1399 m. The bistatic ranges calculated from R-D maps match the theoretical bistatic range for the particular scenario. The signal acquisition time is also calculated for this experiment for ±1 kHz and ±5 kHz Doppler bound. The signal acquisition time is 0.15 sec and 0.21 sec for ±1 kHz and ±5 kHz respectively. Therefore, Doppler bound calculation for the NavIC signal is necessary as it reduces the processing time while generating the R-D map and performing the target localisation using GNSS-R.

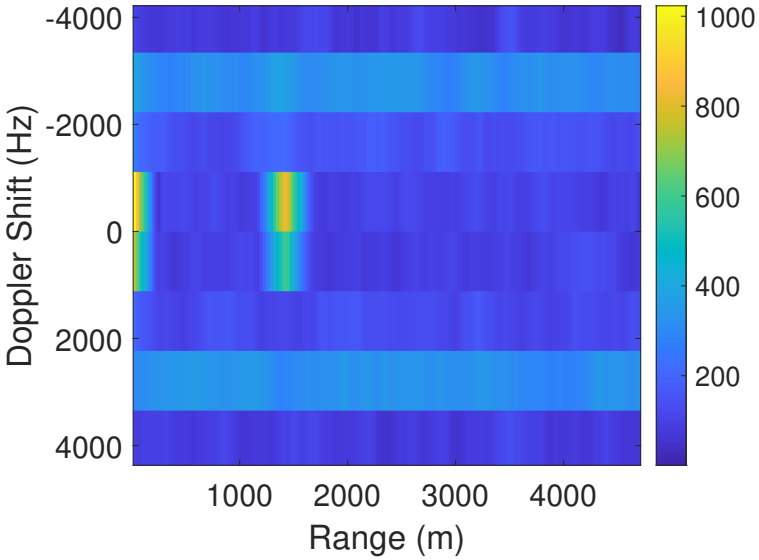

Figure 4.11: Range-Doppler Map example

4.5 Conclusion

This work introduces a comprehensive study on the GNSS-R based target localisation and Doppler frequency bound estimation for the NavIC-L5 multipath signals within the NavIC service area. Target localisation is performed using the GNSS-R technique by optimizing the bistatic range obtained from multi-static scenarios using the least square estimation technique. The bistatic range is calculated for the 4 pairs of observations and is used for the target tracking. The estimated target location is close to the true target point position, with a norm difference of 78m between the two positions and an uncertainty of 91m with an added random noise of 28m in the bistatic range.

Further, Doppler frequency bound calculation is necessary as it is required during the signal acquisition for target tracking applications. The estimation of Doppler frequency bounds for NavIC-L5 multipath signals, observed at various surface locations within the NavIC service area is calculated. The analysis begins with defining the maximum and minimum Doppler frequency bounds based on calculations performed at different surface target points. These bounds are then utilized to optimize the signal acquisition process by narrowing the Doppler search range, thereby improving acquisition efficiency and reducing computational load. The Doppler frequency bound calculations are extended to both static and moving receiver scenarios, enabling a broader

understanding of signal behaviour across diverse setups. For a static receiver, the Doppler frequency bound is found to be ± 0.55 kHz, whereas, for a moving receiver onboard a Low Earth Orbit (LEO) satellite with a velocity of 7.78 Km/s, the bound increases significantly to ± 3.7 kHz. In contrast, for a moving receiver onboard a UAV, the Doppler variation is minimal due to the lower velocity of the UAV compared to the NavIC satellite. These findings highlight the influence of receiver dynamics on Doppler frequency bounds and their implications for signal acquisition.

The calculated Doppler bounds are particularly useful for defining the search range during signal acquisition, thereby minimizing the processing time and computational effort required for GNSS-R analysis. These advancements not only contribute to the field of GNSS-R but also pave the way for improved remote sensing applications, including maritime surveillance, environmental monitoring, and disaster management.

Further, the results are limited to simulated scenarios, and the actual performance in real-world conditions, especially under noisy signal environments and cluttered reflective surfaces, may vary. The future research can be directed toward validating the proposed methodology using field experiments with UAV or satellite-mounted receivers. Incorporating real signal acquisition from the NavIC constellation over diverse terrains such as forests, water bodies, and urban areas will help quantify environmental impacts on bistatic range accuracy.

Chapter 5

GNSS-R Hardware System Design and Real-time Experimentation

Contents

5.1 Introduction

Global Navigation Satellite System (GNSS) constellations are typically used for Positioning, Navigation and Timing (PNT) services. In addition, there are Regional Navigation Satellite Systems (RNSS) such as Navigation using Indian Constellation (NavIC) and Quasi-Zenith Satellite System (QZSS) for enhancing the regional PNT performances [166, 167]. Beyond the traditional PNT services, the GNSS and RNSS signals [168, 169] can successfully be used for remote sensing applications, and this process is termed as GNSS-Reflectometry (GNSS-R) [2]. Moreover, with the expanse of various global and regional navigation satellite systems, the GNSS-R technique has gained attention from the scientific communities. GNSS-R uses satellite navigation signals as the signal of opportunity [170, 171] for remote sensing purposes. It is a passive and cost-effective remote sensing technique that allows the monitoring of geophysical parameters [172] by processing the multipath GNSS signals reflected from the Earth's surface. The GNSS-R technique follows the bi-static or multi-static radar configuration principle, where the receiver and the transmitter are not co-located [173]. In GNSS-R, the existing GNSS satellite constellations are used as the signal transmitters, and the GNSS-R receiver payload can be positioned on a Low-Earth Orbit (LEO) satellite [4, 174, 175, 176] or an Unmanned Aerial Vehicle (UAV) [177, 178]. The ability to use GNSS signals for reflectometry and scatterometry was first proposed in 1988 [55]. Then, its first application for mesoscale ocean altimetry [13] was performed in 1993 using the PAssive Reflectometry and Interferometry System (PARIS) concept. Several spaceborne missions [179, 180], including TechDemoSat (TDS)-1 and NASA's Cyclone Global Navigation Satellite System (CYGNSS), have successfully demonstrated the remote sensing capability of GNSS-R [100, 181]. The CYGNSS mission is a constellation of eight satellites to measure wind speeds over Earth's oceans [182]. CYGNSS mission also provided a large number of terrestrial observations for land surface remote sensing applications [183]. The application of the GNSS-R technique is expanded to soil moisture estimation [184, 17], vegetation cover [16, 185], snow depth measurement [186, 187], wind speed retrieval [188], and many more. Several satellite missions [189, 190, 191, 192], ground-based and

spaceborne[193] experiments have demonstrated the practicality of retrieving the Earth's geophysical parameters [194] using the GNSS-R technique. Prior research in GNSS-R is mainly focused on characterising the Signal to Noise Ratio (SNR) [24, 15], Carrier to Noise Ratio C/N_O [195], and Phase and Amplitude characteristics. The Delay waveform is also used to study the Earth's surface characteristics. However, it is insufficient to capture the impact of noise and the specular point geometry [196].

The above-mentioned works are mainly focused on using GPS [197], Galileo [198], or BeiDou [199] satellite constellation signals. However, the remote sensing capability of NavIC has yet to be extensively assessed. In addition, the existing research on NavIC reflectometry is majorly restricted to the analysis of multipath signals acquired using commercial NavIC navigation receivers [200], which restricts the scope of the research. The proposed research focuses on developing and assessing the capability of a Software Defined Radio (SDR) based GNSS-R receiver for studying the direct and reflected GNSS and RNSS signals for remote sensing applications. The direct GNSS signals have Right Hand Circular Polarisation (RHCP), whereas the reflected signals are Left Hand Circular Polarised (LHCP). Hence, a dedicated circular polarised (CP) antenna is required to receive the GNSS signal. Therefore, a CP antenna is designed to receive both RHCP and LHCP NavIC-L5 and GPS-L1 signals. The field experiments are performed using the proposed GNSS antenna to collect the real-time NavIC-L5, and GPS-L1 reflected and direct signals and further process them for reflectometry applications. The received RF signal is digitised using the SDR front-end and stored as In-phase (I) and Quadrature (Q) phase signals. Further, the received signals are processed into Delay-Doppler Maps (DDMs), which is a measure of the reflected signal power and is a function of reflecting surface properties. The brief theoretical background of the GNSS-R technique, along with the DDM generation and real-time signal acquisition, is explained in the next section. The Numerical Simulation and Hardware-In-Loop (HIL) simulator developed by[165] for the NavIC-R experiments is also described briefly as a part of the experimental framework. The proposed GNSS-R hardware is explained and compared with the existing GNSS-R missions in the following section. The comparison results and analysis of the theoretical, HIL simulator and field experiments are summarized in Results and Analysis. Concluding remarks, along with future work, are discussed at the end of this chapter.

5.2 Theoretical Background

In the GNSS-R technique, the bi-static radar configuration is used to receive the GNSS satellite signals. The characteristics [201] of the received reflected GNSS signal changes based on the properties of the reflecting surface. The bi-static radar configuration of the GNSS-R geometry is shown in Fig. 5.1. In this figure, the GNSS/RNSS satellite is used as a navigation signal transmitter, with reflectometry receiver payloads mounted on the LEO satellite and a UAV flying at a certain height above the ground. The direct satellite signals are received using the Right-Hand Circular Polarised (RHCP) antenna. The signal polarisation changes when the signal reflects from any surface. At the same time, the reflected signals are acquired using a left-hand circular polarised (LHCP) antenna pointed in the direction of the nadir.

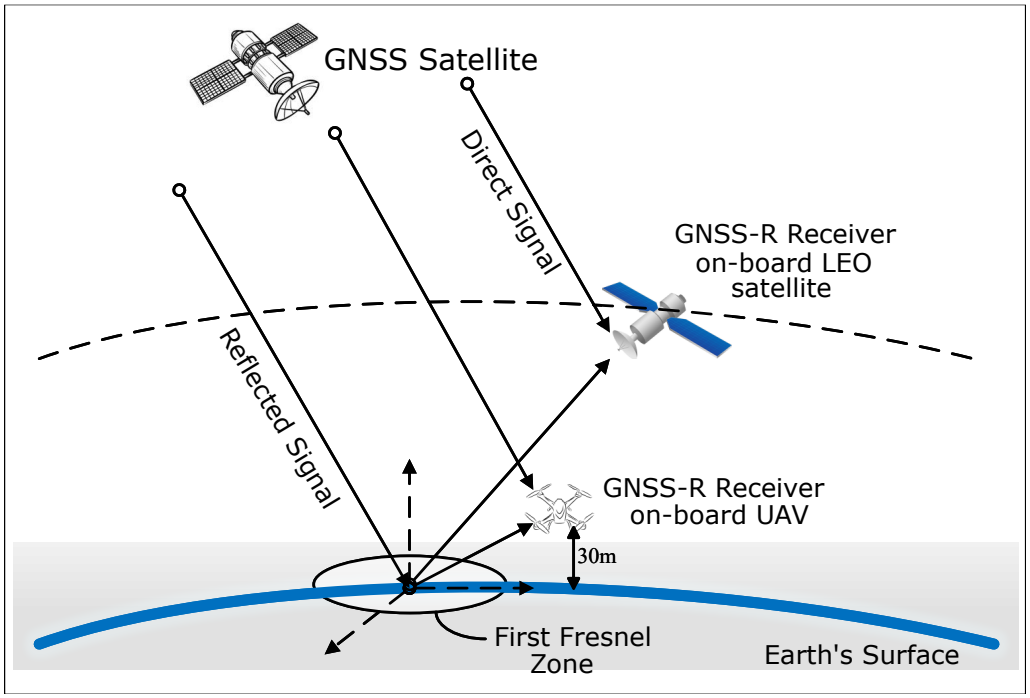

Figure 5.1: GNSS-R geometry

After receiving the GNSS signal, satellite signal acquisition is performed in order to detect the satellite PRN. Satellite signal acquisition is carried out by correlating the incoming satellite signal with the local C/A code, and then performing the peak detection. Generally, 1 ms of signal is used for satellite acquisition, whereas for real-time signal acquisition, a long input signal is necessary. As the real-time signal can be weak, hence, there is a need to collect more input data and perform coherent or non-coherent integration techniques [150] for satellite signal acquisition.

The received real-time GNSS signals are down-converted and passed through a notch filter, before implementing the signal acquisition block. After signal acquisition, the received reflected GNSS signals are processed to generate a Delay Doppler Map (DDM) [1] which is the 2D characterization of the reflected power over the delay-Doppler space. The DDM depends on the transmitter-surface-receiver geometry and physical properties of the reflecting surface. The power distribution $P(\tau, f)$ of the DDM over delay (τ) and doppler-shifted frequency f can be represented using the conventional bistatic radar observation [202]:

$$|P(\tau, f)|^2 = \frac{T_i^2 P_t G_t \lambda^2}{(4\pi)^3} \iint\limits_A \frac{G_r(\vec{\rho})}{R_{ts}(\vec{\rho}) R_{rs}(\vec{\rho})} \sigma_{pq}^{\circ} \chi^2(\vec{\rho}; \delta\tau, \delta f) d\vec{\rho} \tag{5.1}$$

where T_i refers to the coherent integration time, P_t denotes the NavIC signal transmitted power, λ is the GNSS signal wavelength, G_r and G_t are the receiving and transmitting antenna gain respectively, R_{ts} and R_{rs} are distances from the transmitter and the receiver to the surface specular point respectively, σ_{pq}° is the bistatic radar coefficient for a particular pq polarisation, and $\chi(\vec{\rho}; \delta\tau, \delta f)$ is known as the Woodward Ambiguity Function (WAF). WAF is a product of two functions, associated with the Delay offset (τ) and Doppler shifts (f). WAF is expressed as follows [140]:

$$\chi^2(\vec{\rho}; \delta\tau, \delta f) \simeq \Lambda^2(\tau) \cdot |S(f)|^2 \tag{5.2}$$

where $\Lambda = 1 - |\tau| / \tau_c$ if $|\tau| \leq \tau_c$ and 0 otherwise, here τ_c represents the C/A code chip length. And $|S(f)| = |sin(\pi f)/(\pi f)|$.

To simulate DDMs, integration in (5.1) needs to be performed for every Delay and Doppler pair. The above simulation becomes a cumbersome and computationally expensive task. To further simplify the DDM simulation process, (5.1) can be written as a 2D-convolution of the WAF, and the weight factor assigned to each Delay-Doppler pair [140]. Theoretically, the received coherent peak power of the DDM follows the bistatic radar equation, and it is given as [61]:

$$P_p^{coh} = \frac{P_t \lambda^2 G_t G_r}{(4\pi)^2 (R_{ts} + R_{rs})^2} \Gamma_p(\epsilon_s, \theta_i) \tag{5.3}$$

where Γ_p refers to the surface reflectivity for a specific polarization p. According to the bistatic radar equation, the coherently reflected power at the receiver is a function of surface reflectivity Γ_p. Therefore, the received reflected signals can successfully be used for remote sensing applications.

5.3 Simulation and Experimental Setup

This section is divided into two parts where the development of numerical simulator and the HIL simulator model is discussed. The numerical simulation is based on the bi-static radar theory, as discussed in the theoretical background section. The developed models are further used for the verification of the field-experiments. The GNSS-R HIL simulator testbed developed by [160] is also discussed in this section.

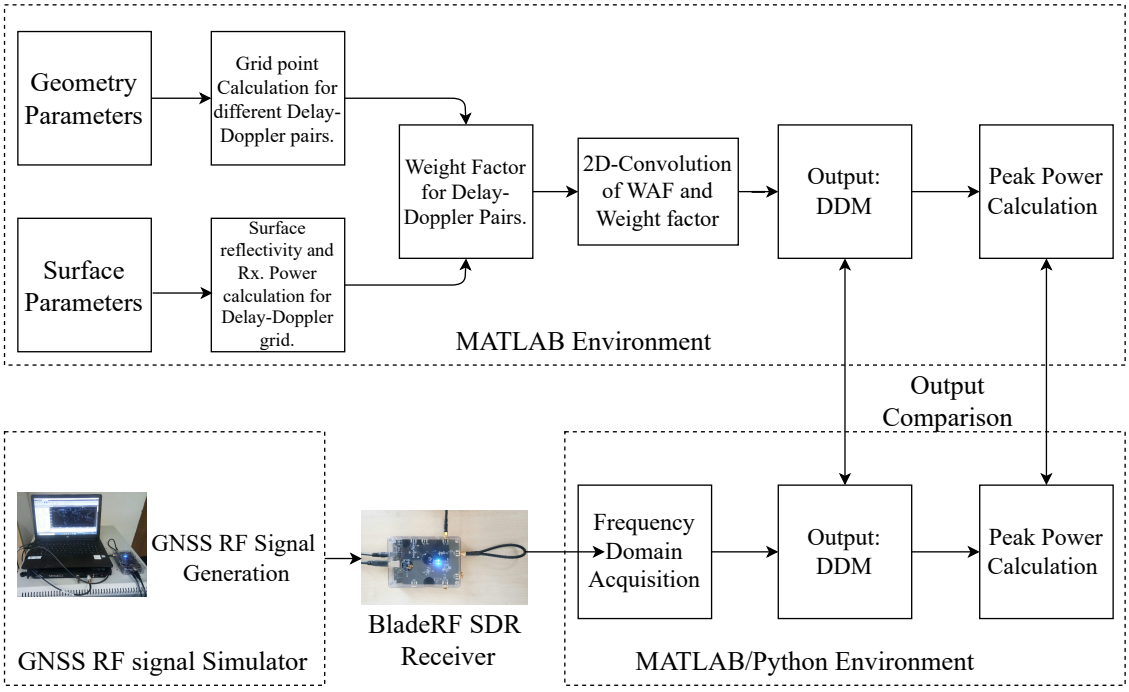

Figure 5.2: Numerical and Experimental simulation framework, describing the DDM generation and peak-power calculation using the numerical calculation and experimental hardware-in-loop setup.

5.3.1 Numerical Simulation Framework

The numerical simulation of the DDM is divided into two parts: Geometry and Surface parameters initialization and the DDM generation. It is implemented in MATLAB, using the equations defined in the theoretical section, and the framework is shown in Fig. 5.2. The geometry and surface parameter initialization are taken as the input for the numerical simulator. The geometry parameters include the height of the transmitter and the receiver from the ground surface. The transmitter and receiver antenna gain G_t,G_r, GNSS transmitted signal power P_t, and the incidence angle θ_i are also part of the geometry parameters. The geometry parameters are further used to calculate the R_{ts} and R_{rs} for the different Delay-Doppler grid points. To obtain the DDM, the WAF is simulated for all (τ, f) cells using the (5.2). The receiver and transmitter geometry are used along with the surface dielectric constant, which is a surface parameter, to calculate the surface reflectivity and the received coherent peak power for assigning a weight factor for each delay-Doppler grid point. The 2D convolution of the WAF and the weight factor results in the Delay Doppler Map. The numerical simulator is designed to verify the results of the experimental simulator that are obtained using the simulated NavIC-L5 and GPS-L1 RF signal.

5.3.2 Hardware-In-Loop (HIL) Simulation Framework

The experimental setup for generating the DDM using the GNSS-R is shown in Fig. 5.2. The NavIC-L5 and GPS-L1 RF reflected signal studied in the HIL simulator is simulated using the SIMAC2 GNSS Simulator. The BladeRF SDR is the hardware module that is involved in signal acquisition during the HIL experiment. The Nuand BladeRF x115 is used as a GNSS signal receiver unit. It can be tuned to a frequency range of 300 MHz to 3.8 GHz and, hence, is suitable for all the GNSS frequency bands (L1 (1575.42 MHz), L (1227.6 MHz) and L5 (1176.45 MHz)). The BladeRF SD is used as a digital front-end device to receive the GNSS RF signals and downconvert the received GNSS signal to the baseband signal. The BladeRF digitized RF signal can be stored as a .csv or .bin file, which includes the In-phase and Quadrature phase (I/Q) GNSS signal. The BladeRF x115 is paired with a Nuand XB-300 amplifier. Nuand XB-300 amplifier is a Low-Noise Amplifier (LNA) with a typical gain of 21 dB at 2.0 GHz and a bandwidth ranging from 500

MHz to 5 GHz. The single-board processing unit used in the receiver setup is a Raspberry Pi 4 model B (RPi-4b). The RPi-4B model is used because it has a USB-3.0 port, which supports a faster data transfer rate. The Ubuntu 20.04 is installed on RPi-4B to interface the BladeRF SDR and process the stored GNSS signal. The BladeRF software and the expansion board XB-300 software is installed in linux on RPi. The BladeRF SDR front-end receives the GNSS RF signal and digitizes it into In-phase (I) and Quadrature Phase (Q) data which is then transferred to the MATLAB/Python environment for further processing. The workflow and the hardware devices involved are shown in Fig.5.3. In Fig.5.3, it is shown that GNSS RF signals are simulated using the GNSS simulator. The output of the GNSS simulator is connected to the RX input of the SDR. The signals are further received using the RPi and the signal processing is performed on-board RPi only.

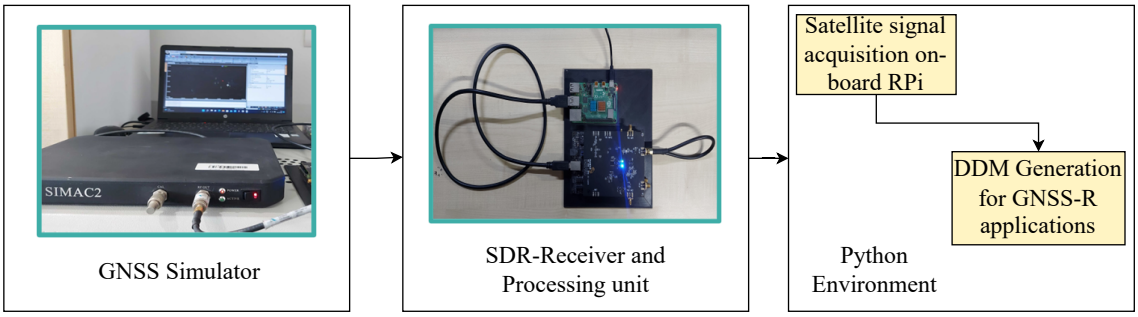

Figure 5.3: Multi-frequency GNSS simulator hardware and workflow

The hardware includes the GNSS simulator and receiver unit and a software processing block to process the GNSS signal. The single-board processing unit used in the receiver setup is a Raspberry Pi 4 model B (RPi-4b). The RPi-4B model is used because it has a USB-3.0 port, which supports a faster data transfer rate. The Ubuntu 20.04 is installed on RPi-4B to interface the BladeRF SDR and process the stored GNSS signal. The GNSS signal is processed in a Python environment for satellite signal acquisition and DDM generation. The hardware SDR-Receiver setup is shown in Fig.5.4. The BladeRF x115 receiver port is connected to the GNSS signal simulator via a sma-to-sma connector to receive the GNSS RF signals. The BladeRF is further connected to RPi-4B using a USB 3.0 SS cable. The RPi-4B is connected to a 5V-DC power supply, and the bladeRF is powered by RPi-4B itself.

The multi-frequency GNSS signals are simulated using the Accord's SIMAC2 GNSS sim-

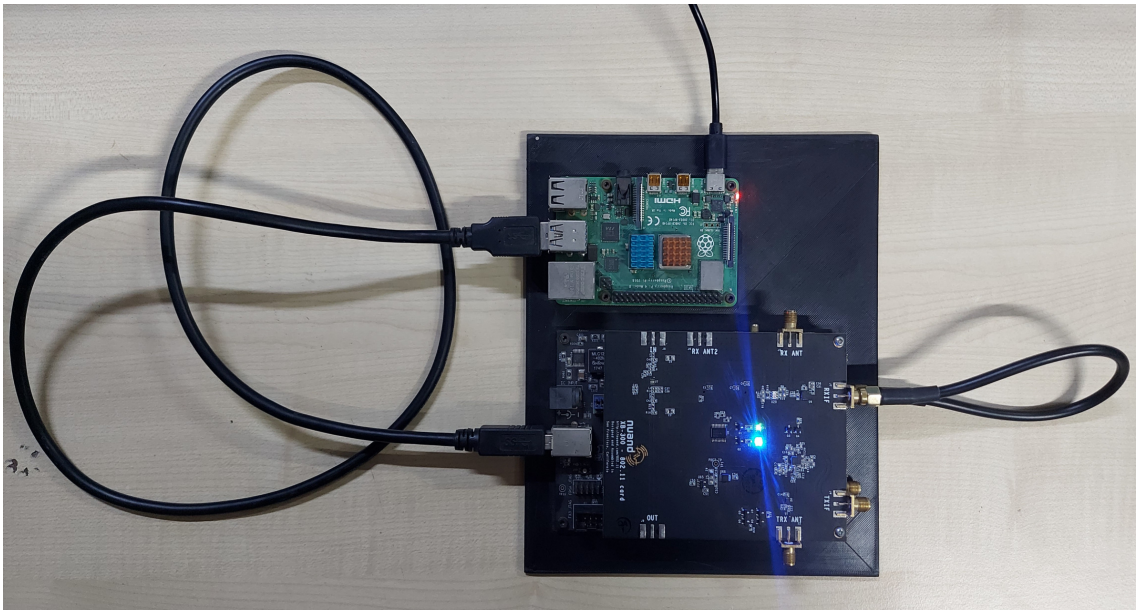

Figure 5.4: SDR-Receiver and on-board processing unit

ulator. It has the capability to generate the multipath NavIC-L5 and GPS-L1 satellite signals. The BladeRF Software Defined Radio (SDR) Receiver is tuned to receive both the GPS-L1 and NavIC-L5 satellite signals. The BladeRF is interfaced via commands from the onboard processing unit, i.e. RaspberryPi. The script followed for receiving the multi-frequency GNSS signal is summarized and explained in Algorithm 4. The script is implemented in Raspberry Pi, and it collects both the NavIC-L5 and GPS-L1 signals simultaneously in a single run. The collected binary data files are read and further processed for satellite signal acquisition and DDM generation using the Python script.

The Frequency-Domain Acquisition (FDM) [138] is performed for satellite PRN [203] search and to identify the satellite Delay and Doppler variations which result in the DDM. The FDM acquisition method involves the correlation of incoming satellite signals with the locally generated PRN code in the frequency domain. The Parallel Code Phase Search (PCPS) Acquisition [152] technique is used for the signal acquisition. In the PCPS algorithm, the acquisition is performed in parallel, and it significantly speeds up the acquisition process [204]. The PCPS algorithm for satellite signal acquisition is outlined in the following block diagram in Fig.5.5.

Typically, 1 ms of data length is selected for performing the satellite signal acquisition, whereas for the weak satellite signal acquisition, it is necessary to perform coherent or non-coherent

Algorithm 4: Multi-frequency GNSS signal receiving script

STEP1: Receiving the NavIC-L5 signals

- set frequency rx 1176.45M
- set samplerate rx 16M
- set bandwidth rx 5M
- rx config file=NavICL5.bin format=bin n=1M
- rx start;
- rx
- rx wait
- rx

STEP2: Receiving the GPS-L1 signals

- change the rx frequency to 1575.42M
- change the filename to GPSL1.bin
- repeat the steps given in STEP1

OUTPUT: NavIC and GPS I/Q data (NavICL5.bin, GPSL1.bin)

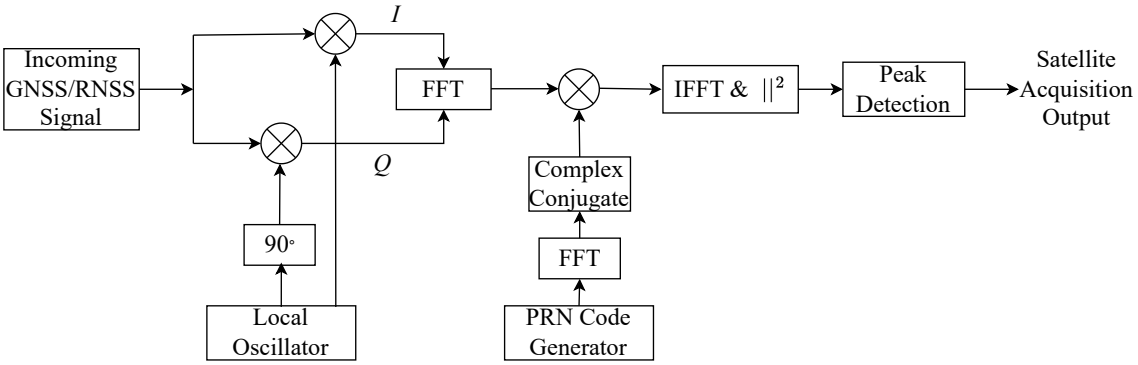

Figure 5.5: Block diagram of satellite signal acquisition algorithm

integration to improve the detection output [150]. After performing the satellite acquisition to detect the available satellites, Delay Doppler Map (DDM) generation is the next step for performing GNSS-R analysis. The different time delay and Doppler shift around the specular point along with the associated received power, is represented as the DDM. The received coherent peak power P_p^{coh} is derived from the DDM observable and can further be used to calculate the surface reflectivity τ_p.

5.4 GNSS/RNSS-Reflectometry Receiver Design

The reflectometry receiver proposed in this work is divided into three parts: RF front-end, mixed-signal segment, and general-purpose processing unit. The complete architecture of the GNSS-R Receiver Design is shown in Fig. 5.6. The proposed receiver consists of an in-house designed and fabricated GNSS antenna. After the antenna, two LNAs are connected to increase the received signal strength. The 2nd LNA is connected to the receiving port of the BladeRF SDR. The BladeRF is finally interfaced using an RPi 4B. A detailed explanation of these blocks is provided in the next section.

5.4.1 RF Front-End Design

The analog RF front-end consists of a passive antenna, which is used to receive both the direct and reflected (LHCP) GNSS RF signals. The commercially available antennas for receiving GNSS-reflected signals are costly, bulky and not readily available. Therefore, we have designed, fabricated,

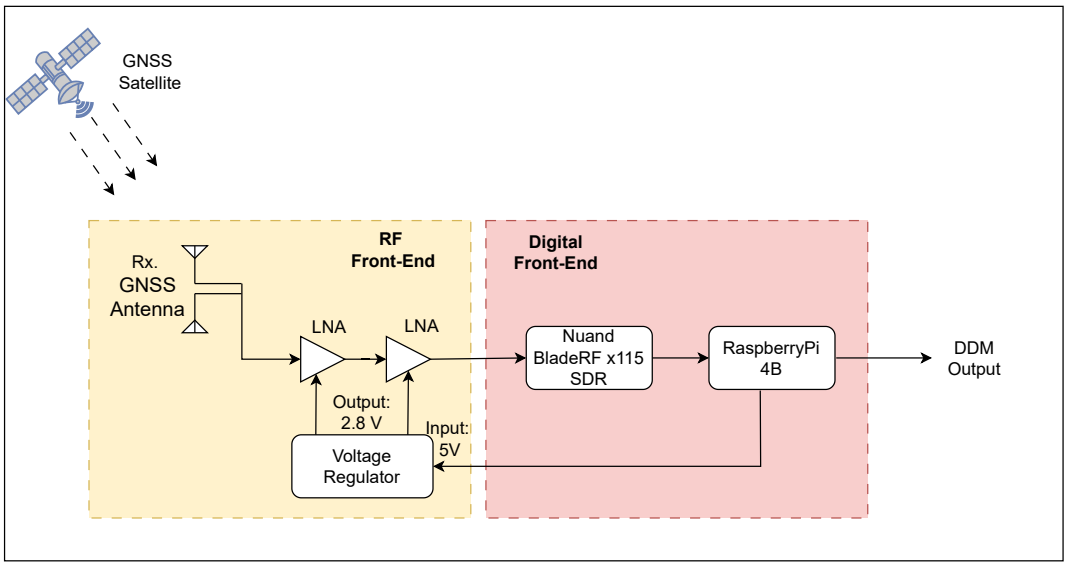

Figure 5.6: GNSS-R Receiver Architecture

and tested a PCB-based CP antenna in-house. This antenna is low-cost, lightweight, and suitable for onboard drone usage, as well. The front and back view of the antenna is shown in Fig. 5.7. It has a U-shaped slot and is fed using two microstrip lines. The antenna is fabricated on a FR-4 substrate material. The following paper [205] is taken as the reference for the proposed antenna design. The fabricated GNSS antenna based on the design is shown in Fig. 5.8. Further, this fabricated antenna is used for field experimentation.

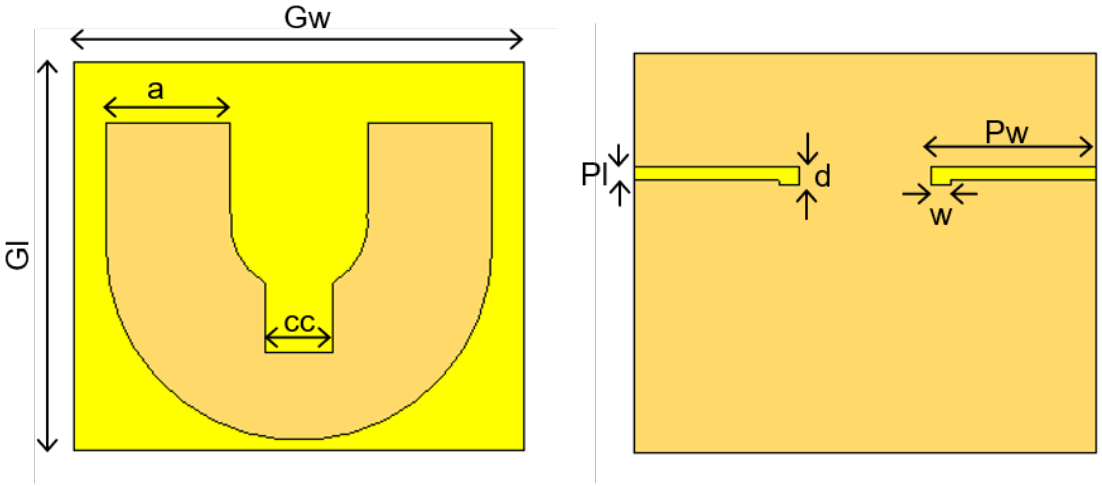

(a) Front View of designed Antenna

(b) Back View of designed Antenna

Figure 5.7: Antenna Design

The antenna design parameters are as follows: The antenna ground dimensions Gl and Gw are 95 mm and 105 mm, respectively. The width of the slot a is 29 mm. The microstrip feed

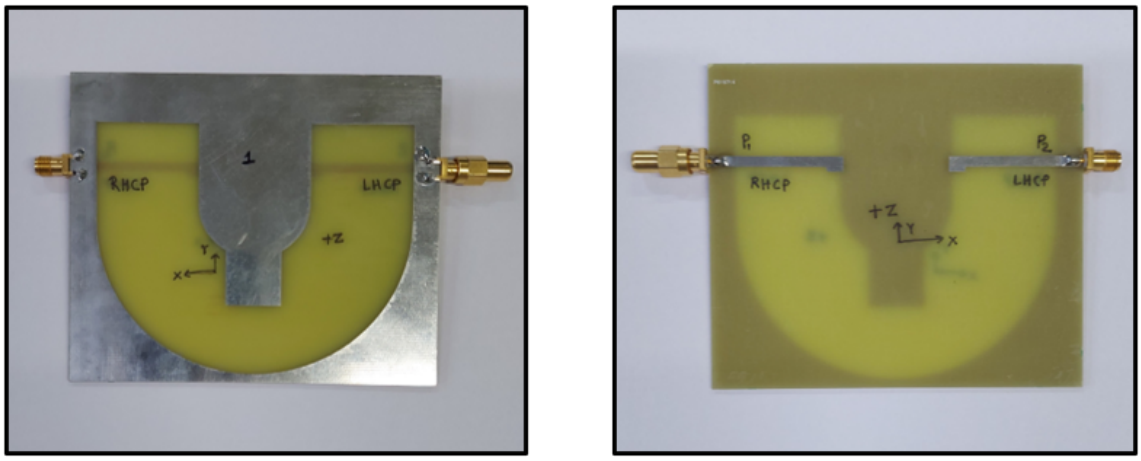

Figure 5.8: Fabricated Antenna

port lengths Pl and Pw are 2.85 mm and 24.18 mm, respectively. The dimensions cc, d and w are 16 mm, 4.23 mm and 4.68 mm, respectively. The S-parameters (S11, S21 and S22) of the proposed antenna are shown below in Fig. 5.9:

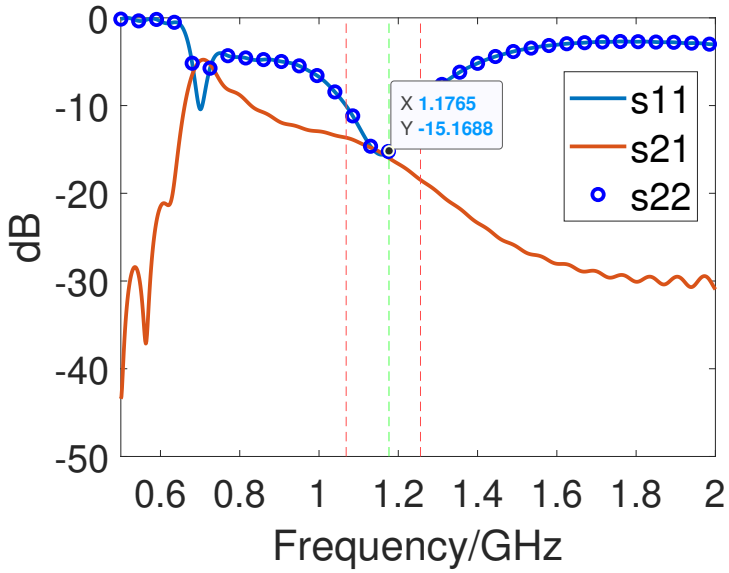

Figure 5.9: S-Parameters of Proposed Antenna

The S11 is less than -10 dB from 1.0 GHz to 1.25 GHz, as shown in Fig. 5.9 covering the required frequency range of GNSS signals. The axial ratio of the proposed antenna is shown in Fig. 5.11. The axial ratio is below 3db in the frequency range from 1.0 GHz to 1.3 GHz for the required frequency range, which is needed for a CP antenna.

The radiation pattern of the proposed antenna at 1.176 GHz is shown below in Fig. 5.11. It can be observed that port 1 provides LHCP as co-polarized radiation, whereas port 2 exhibits

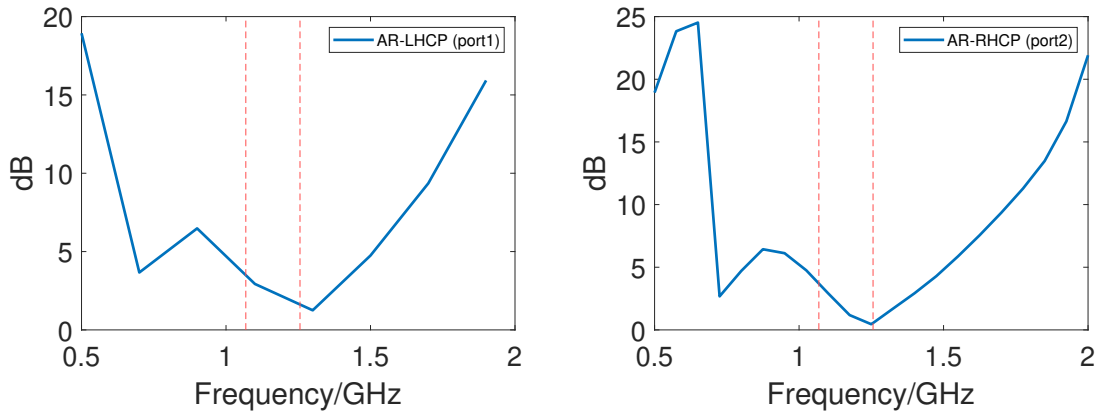

(a) Port 1 (b) Port 2

Figure 5.10: Axial-Ratio for the proposed antenna when each of the two feeding ports, Port 1 (left) and Port 2 (right), is excited individually

RHCP as co-polarized radiation. Thus, the antenna can be used as a dual circular polarized antenna.

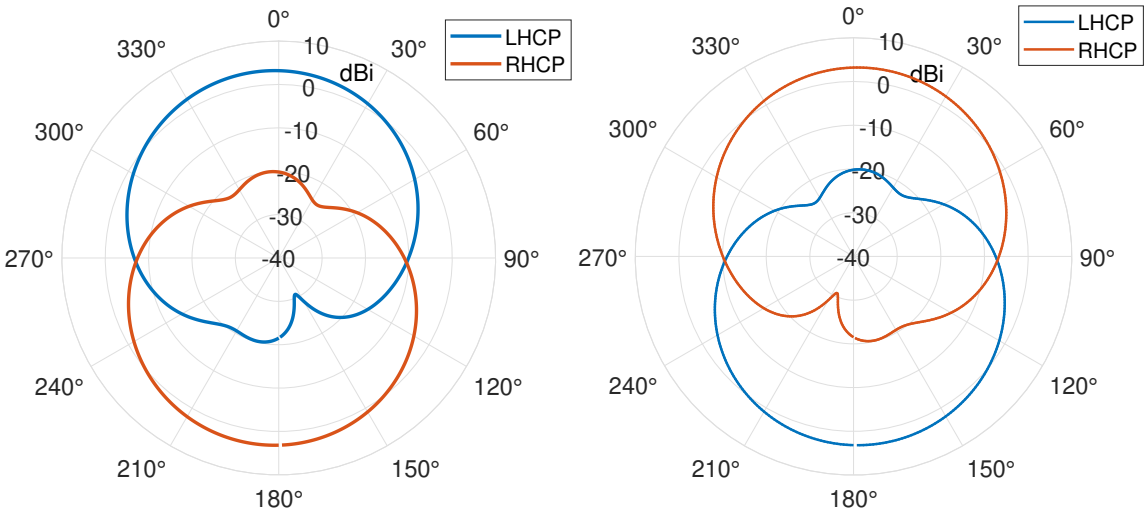

(a) Port 1 (b) Port 2

Figure 5.11: Radiation Pattern at 1.176 GHz. Port 1 (left) and Port 2 (right) exhibit LHCP and RHCP as co-polarized radiated patterns, respectively.

After the antenna is designed and fabricated, it is connected with the SDR receiver in order to receive the GNSS-RF signal and perform the signal acquisition. The received signal is analysed in MATLAB and it has been observed that the signal power is significantly low and it was not possible to detect the visible satellites. In order to improve the signal strength two LNAs are used to amplify the weak GNSS signal. The BGA125N6 ultra-low current low noise amplifier for L2/L5 GNSS application by Infineon is used. Each of the LNA used have a frequency range of 1.164 GHz to 1.3 GHz and a gain of 20 dB.

5.4.2 Mixed-Signal Segment

The mixed-signal segment comprises a BladeRF SDR. The Nuand BladeRF x115 SDR works in the frequency range of 300 MHz to 3.8 GHz and, hence, is suitable for all the GNSS/RNSS frequency bands (L1 (1575.42 MHz), L2 (1227.6 MHz) and L5 (1176.45 MHz)). The BladeRF x115 is paired with a Nuand XB-300 amplifier that has a typical gain of 21 dB at 2.0 GHz. The BladeRF SDR is used as a reprogrammable digital front-end device to receive the GNSS RF signals and down-convert the received GNSS signal to the baseband signal. The BladeRF SDR is programmed to receive 20ms of both the NavIC-L5 and GPS-L1 simultaneously and store it in two separate .bin files. The BladeRF digitized RF signal can be stored as a .csv or .bin file, which includes the In-phase and Quadrature phase (I/Q) GNSS signal. The BladeRF is further connected to the processing unit using a USB 3.0 SS cable.

5.4.3 Processing Unit

The single-board processing unit utilized in the receiver setup is a Raspberry Pi 4 model B (RPi-4B). The Ubuntu 20.04 is installed on RPi-4B to install and access the BladeRF SDR and process the received GNSS signal. The received GNSS signals are processed within a Python environment to perform satellite signal acquisition and DDM generation. The signal received through the field experiment is down-converted [151] and passed through a digital notch filter [206] in order to remove the DC component and mitigate unintentional narrowband interference. The unintentional narrowband interference can be due to improper shielding of the equipment due to, which can pick up unwanted signals from the environment. Also, the signals in adjacent bands will, at times, fall within the range of frequencies processed by GNSS receivers [138]. After notch filtering, the non-coherent integration technique is used to acquire satellite signals. The RPi-4B is connected to an on-board 5V-DC power supply, and the BladeRF is powered by the RPi-4B. The complete GNSS-R unit is 0.5kg in mass, and the board consisting of the Processing unit and the mixed-signal segment has a dimension of 200x170x60 mm. The proposed hardware has a small size and low power requirement; hence, the design is suitable to be used onboard a UAV or LEO satellite.

5.5 Comparison with Existing GNSS-R receivers

The already existing GNSS-R includes the UK's TechDemoSat (TDS)-1 and NASA's Cyclone Global Navigation Satellite System (CYGNSS). A detailed comparison of the capabilities of the proposed GNSS-R receiver is presented in Table 5.1.

Table 5.1: Comparison of proposed GNSS-R receiver with existing technologies

Characteristics	**Proposed GNSS-R**	**TechDemoSat (TDS)-1**	**CYGNSS**
Frequency Capability	GPS-L1, NavIC-L5	L1 and L2C	L1 GPS
Antenna Port (Zenith/Nadir)	1 Nadir, 1 Zenith	1 Nadir, 1 Zenith	2 Nadir, 1 Zenith
Sampling Rate	12/16 MHz, I, Q Both	16.367 MHz, I only	16.3602 MHz, I only
Size, Mass	200x170x60mm, 0.5kg	300x200x50mm, 2kg	300x200x50mm, 2kg
Power Consumption	5W	4W and 9W	4W and 9W

5.6 Field-Experiment

A series of field experiments is conducted on 29th February 2024, 12:30 pm, at IIIT-Delhi, New Delhi, India. The latitude and longitude of IIIT-Delhi are 28.5459° N, 77.2732° E. The designed antenna is characterised for receiving the NavIC-L5 signals. However, the receiver is able to receive both the GPS-L1 signals and NavIC-L5. The field experiments are conducted to collect the reflected GPS-L1 and NavIC-L5 signals, which can further be used for reflectometry applications. The GNSS antenna is placed on a tripod and is connected to the BladeRF SDR using a SMA cable. The direct RHCP GNSS signals are collected by facing the antenna upwards to the open

sky. Whereas the antenna is faced towards the ground to collect the reflected LHCP GNSS signals. First, the direct (RHCP) signal is collected using port 2 while terminating port 1 with a match load (50Ω). Subsequently, the reflected (LHCP) signal is collected using port 1, while terminating port 2 with the match load. The SDR is programmed to collect both the GPS-L1 and NavIC-L5 signals with a centre frequency of 1575.42 MHz and 1176.45 MHz, respectively. The GNSS signals are collected in real-time at a sampling frequency of 12 MHz and bandwidth of 5 MHz. The field experimentation setup (left) and the receiver hardware (right) unit consisting of BladeRF SDR and RPi are shown in Fig. 5.12.

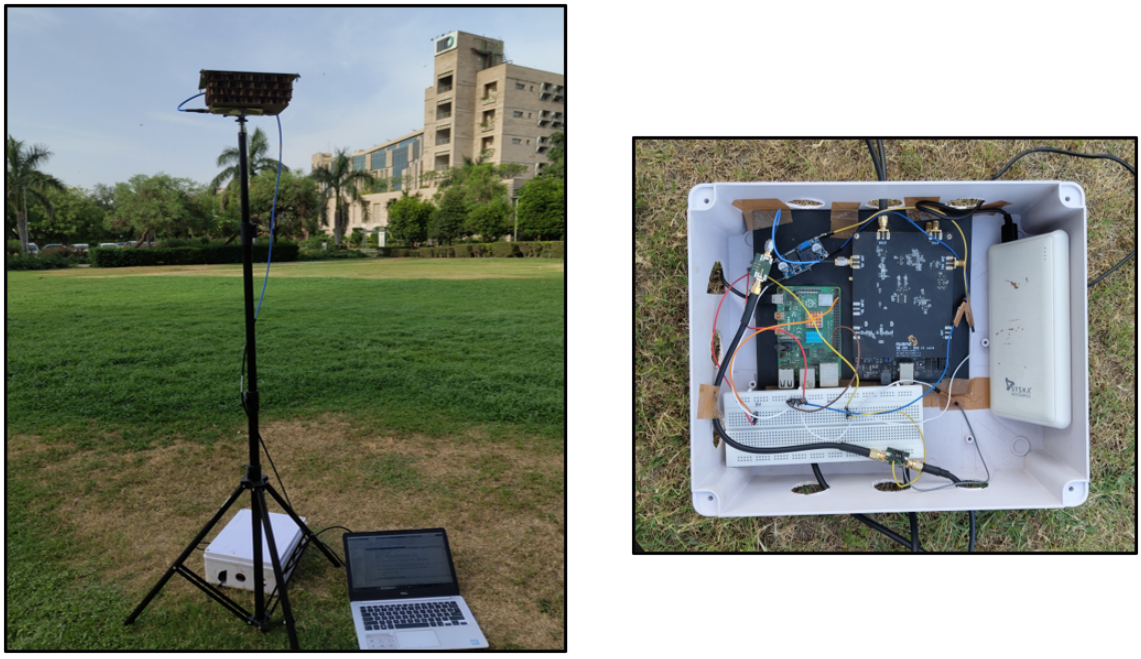

Figure 5.12: Field Experiment Setup (left) and Receiver setup (right)

The direct and reflected signals are obtained in sequence, and the DDM are basically the correlation of the PRN code with the direct and reflected signals. The reflected signal is collected within 1 minute just after the direct signal is recorded. The change in the angle after 1 minute is very small and is denoted as δ. Considering the geometry given in Fig.5.13

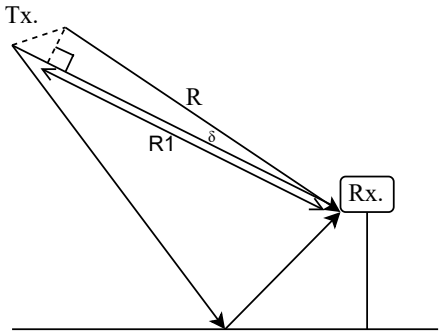

Figure 5.13: Signal reception geometry

$$cos\delta = \frac{R1}{R}$$

$$R1 = Rcos\delta$$

$$R - R1 = R(1 - cos\delta)$$

$$\text{if } \delta \text{ is small}, cos\delta \approx 1$$

$$R - R1 \approx 0 \tag{5.4}$$

Therefore, we have compared the results of the direct and reflected signals, as the change in satellite distance is very small compared to the distance of the satellite from the receiver.

The direct and reflected signals received during the field experiments are processed into DDMs. The DDMs for the NavIC-L5 direct and reflected signal are shown in Fig. 5.14. Satellite PRN 4 is detected in the direct and the reflected NavIC-L5 signal, respectively.

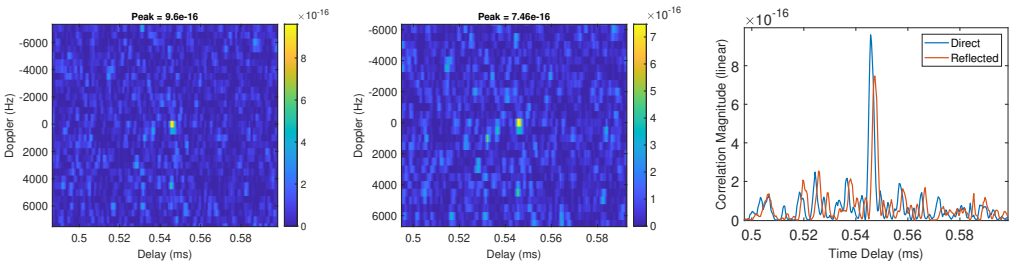

(a) Direct signal DDM (b) Reflected signal DDM (c) Peak waveform

Figure 5.14: DDMs for NavIC-L5 direct (left) and reflected (middle) signal and the peak waveform (right) for both the signals.

Similarly, the DDMs for GPS-L1 direct and reflected signals are shown in Fig. 5.15. After satellite acquisition, PRN 28 is detected both in direct and reflected GPS-L1 signals.

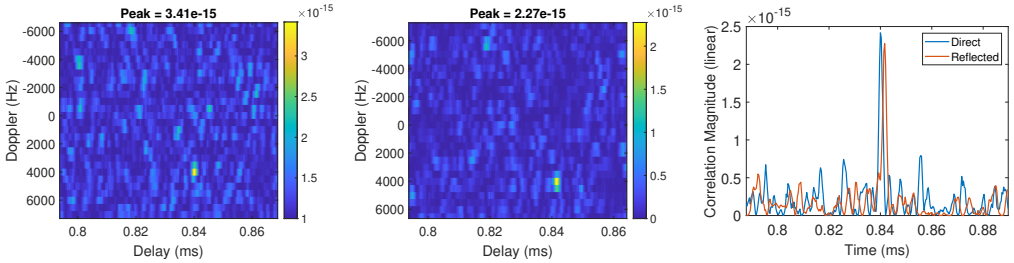

(a) Direct signal DDM (b) Reflected signal DDM (c) Peak waveform

Figure 5.15: DDMs for GPS-L1 direct (left) and reflected (middle) signal and the peak waveform (right) for both the signals.

It is evident from the above DDMs shown in Fig. 5.14 and Fig. 5.15 that the delay in the direct signal is slightly less as compared to the delay in the reflected signal. Also, the correlation peak is less for the reflected signal as compared to the direct signal, which is due to multipath reflections and attenuation. The peak waveform for both the direct and the reflected signal is also shown in Fig. 5.14 and Fig. 5.15, which depicts the difference in the peak values of both the direct and reflected signals.

5.7 Results and Analysis

The verification of numerical simulations and HIL testbed used for estimating DDM and deriving the DDM peak power is performed by comparing their results together. The numerical simulation is verified by comparing the generated DDM with the DDM obtained from the HIL simulation for the same scenario. The DDM comparison for the numerical simulation and the HIL simulation is shown in Fig. 5.16. The DDMs shown in Fig. 5.16 are in agreement with each other. Hence it validates the numerical simulation as well as the HIL testbed developed for reflectometry application.

After verification of the numerical simulation and the HIL simulator testbed results, the field experiments are carried out. The DDMs generated using the GNSS signals obtained from the field experiments are also compared with the HIL and numerically generated DDMs. The field experiments are carried out using the proposed receiver to collect the real-time GNSS RF signals and generate the DDM. The comparison of DDMs obtained using numerical simulation,

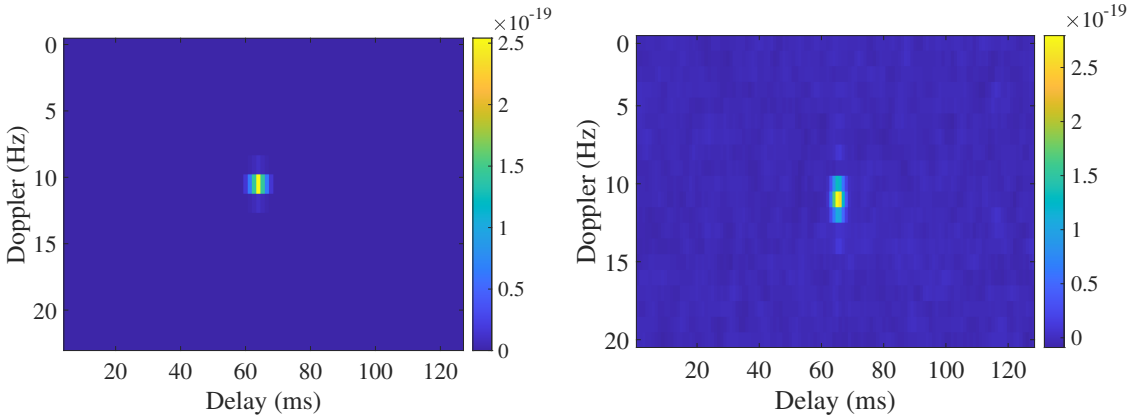

(a) Port 1 (b) Port 2

Figure 5.16: Comparison of numerically obtained DDM (left) and HIL simulation DDM (right)

HIL simulator and field-experiment obtained NavIC-L5 signals are presented in Fig. 5.17. The NavIC satellite PRN 7 is detected in the received signal.

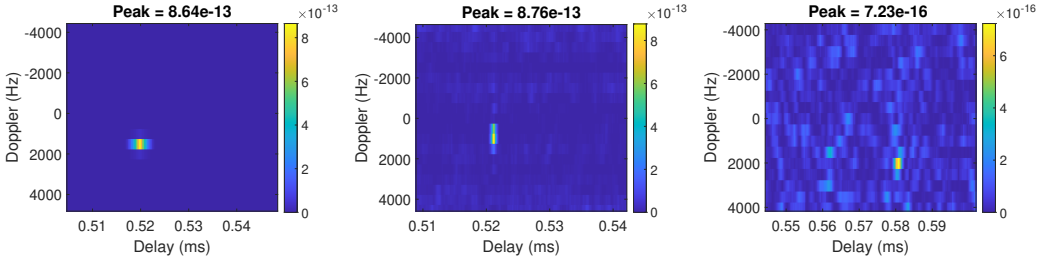

(a) Numerical Simulation DDM (b) HIL DDM (c) Field-Experiment DDM

Figure 5.17: Comparison of numerical simulated (left), HIL (middle) and Field-Experiment (right) DDM for NavIC-L5 signal

The numerical simulation and the HIL DDM are in agreement with each other. Whereas the received peak power levels of field-experiment obtained DDM is lower than the other two. The power levels obtained from the field experiments are less because of the additional noise, which is not present in the simulation. The field-experiment results have a slightly different Doppler as well, which can be due to additional signal processing, which includes notch filtering and a non-coherent integration technique. The delay is also higher in the field experiments, which is the result of ionospheric and tropospheric effects which are not considered in the simulation. Similarly, the comparison for the DDMs obtained using numerical simulation, HIL simulator and real-time GPS-L1 signals are present in Fig. 5.18. The GPS satellite PRN 7 is detected in the received signal. The DDMs for the three cases are in agreement with each other. However, the field-experiment obtained DDM for GPS-L1 has lower peak power levels which is the result of additional noises and higher multipath attenuation in the received signal. The delay in the field experiment is higher

because of the ionospheric and tropospheric effects.

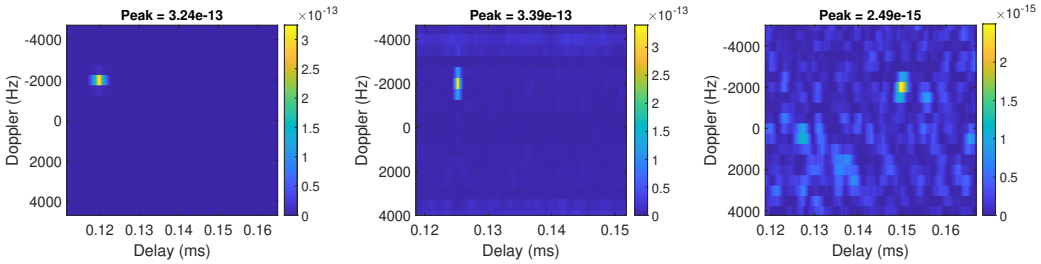

(a) Numerical Simulation DDM (b) HIL DDM (c) Field-Experiment DDM

Figure 5.18: Comparison of numerical simulated (left), HIL (middle) and Field-Experiment (right) DDM for GPS-L1 signal

The results presented in this section shows the feasibility of using the proposed antenna along with BladeRF SDR and RaspberryPi for reflectometry applications. The field experiments results are verified with the numerical and HIL simulation results. While the designed receiver has demonstrated successful signal acquisition and DDM observable generation, the BladeRF SDR has certain limitations. The sample rate should be adjusted according to the maximum achievable sample rate related to the USB driver and system specifications. If the sample rate is not selected correctly, the acquired samples will drop while receiving the signal. Also, the BladeRF doesn't support active antennas, hence, a passive antenna is required for receiving the satellite signals. The BladeRF hardware used for the study is not radiation hardened, therefore it can't be used on a low-earth satellite platform, whereas it is suitable for drone/UAV based applications. The power consumption requirement of BladeRF is 4.5W, hence it can be easily used for drone based GNSS-R applications. In future, we plan to make proposed GNSS-R payload radiation hardened for satellite missions. Further research is necessary to explore the capability of NavIC-R in a wide range of applications such as sea state estimation, snow depth estimation, drought and flood monitoring and many more.

5.8 Conclusion

This research introduces an innovative Software-Defined Radio (SDR)-based multi-constellation GNSS-Reflectometry (GNSS-R) receiver designed specifically for acquiring and processing reflected NavIC-L5 and GPS-L1 signals. The primary objective of this work is to demonstrate the poten-

tial of such a receiver for remote sensing applications, with a particular emphasis on the unique capabilities of NavIC-L5 signals. This study serves as a proof-of-concept, marking one of the first attempts to utilize NavIC-L5 signals for GNSS-Reflectometry, thereby broadening the scope of GNSS-R applications beyond the traditional reliance on GPS signals. The proposed receiver was developed with a focus on versatility, compactness, and efficiency, enabling it to operate effectively as a multi-constellation GNSS-R platform. Its performance was demonstrated through a combination of numerical simulations, hardware-in-the-loop (HIL) simulator testbed validations, and real-world field experiments. The integration of these methodologies ensured a comprehensive evaluation of the receiver's capabilities in both controlled and practical environments.

Field experiments were conducted to validate the receiver's ability to acquire and process GNSS signals for reflectometry purposes. These experiments successfully demonstrated that the receiver is capable of receiving both the direct (Right-Hand Circularly Polarized, RHCP) and reflected (Left-Hand Circularly Polarized, LHCP) RF signals from GPS-L1 and NavIC-L5. The collected data was further processed to generate Delay-Doppler Maps (DDMs), a critical output for GNSS-R applications. The results confirmed the receiver's ability to accurately generate DDMs, thereby enabling the measurement of key reflectometry parameters such as bistatic delay, Doppler shifts, and signal coherence. One of the notable advantages of the proposed receiver is its compact size and low power consumption, making it highly suitable for deployment in resource-constrained platforms such as airborne or spaceborne systems. Its design aligns well with the growing demand for lightweight, energy-efficient, and scalable GNSS-R receivers for environmental monitoring and climate studies. Furthermore, with appropriate radiation hardening, the receiver can be adapted for use in spaceborne missions, extending its applicability to global remote sensing operations.

Future work will focus on enhancing the receiver's capabilities to enable real-time processing and analysis of GNSS-R data. This includes the development of advanced retrieval algorithms for estimating Essential Climate Variables (ECVs) such as soil moisture, sea surface height, and vegetation biomass. Real-time retrieval capabilities will allow the receiver to provide actionable insights for climate monitoring, disaster management, and environmental assessments. Additional efforts will also explore the integration of machine learning techniques to improve signal processing efficiency and refine reflectometry parameter estimation. In conclusion, this work presents

a significant step forward in the field of GNSS-Reflectometry by introducing a novel SDR-based multi-constellation receiver with demonstrated capabilities for acquiring and processing reflected NavIC-L5 and GPS-L1 signals. The receiver's successful validation through simulations and field experiments underscores its potential for diverse remote sensing applications. Its compact design, low power requirements, and adaptability for airborne and spaceborne deployments make it a promising tool for advancing GNSS-R research and addressing critical challenges in environmental and climate studies.

Chapter 6

Conclusion and Future Work

Contents

6.1 A summary of Thesis

Satellite-based remote sensing comprises a variety of techniques that collect data and provide information about the Earth's land surface, oceans and atmosphere by using the sensors on board the satellite platform. The traditional techniques include optical remote sensing, microwave remote sensing and Lidar-based remote sensing. These conventional RF-based approaches necessitate dedicated transmitters and receivers to measure and analyse Earth's geophysical parameters accurately. Recent advancements in GNSS research have introduced a passive remote sensing technique, termed GNSS-Reflectometry (GNSS-R). This technique leverages GNSS signals in bistatic or multi-static configurations, capitalizing on the availability of freely accessible GNSS signals to observe various Earth-surface characteristics. Current GNSS-Reflectometry (GNSS-R) research primarily concentrates on signals from GPS, Galileo, and GLONASS satellite constellations. Expanding upon this foundation, the present research aims to utilize signals from the Indian Regional Navigation Satellite System (NavIC) alongside GPS-L1 signals to advance remote sensing applica-

tions. This PhD thesis offers a comprehensive theoretical and experimental investigation into the design and development of a multi-frequency GNSS receiver for Earth observation. The chapter provides an overview of the contributions of this research, alongside a summary of potential future research directions in this evolving field.

The primary contributions of this thesis are structured into three main sections:

- Firstly, this thesis addresses the compression of large GNSS-Reflectometry (GNSS-R) datasets, a critical step to minimize the onboard storage resources required by the payload. Effective data compression is essential for efficient handling and storage of extensive GNSS-R datasets, enabling more sustainable use of computational and memory resources in satellite platforms.

- Secondly, this thesis involves target localisation using GNSS-R and the calculation of Doppler frequency bounds for NavIC-L5 multipath signals. These calculations are fundamental for signal acquisition as the processing time is reduced by using the correct Doppler bound while performing GNSS-R analysis.

- Lastly, this thesis includes the design of an antenna tailored for GNSS-R applications, as well as the development of a Software-Defined Radio (SDR)-based receiver for GNSS-R reflectometry. The antenna design is optimized for signal reception across the required frequency bands, while the SDR-based receiver offers flexible and efficient processing of reflected GNSS signals, advancing the applicability and accuracy of GNSS-R techniques for Earth observation. The contributions of this thesis are structured into three main sections.

The above-mentioned contributions are explained in chapters 3, 4 and 5. Chapter 3 discusses the compression of GNSS-R data for on-board processing and transmission to a local server. In this work, the BPDN convex optimisation algorithm of compressive sensing theory is applied to the GNSS signal. The performance of different sparsifying and measurement matrices on GNSS RF signals is compared. The proposed algorithm is applicable to noisy signals as well. It is verified by adding noise to the original signal and then reconstructing it using the proposed algorithm. Additionally, the acquisition of satellites after the reconstruction of the data is performed using the frequency-domain correlation technique. The same satellite PRN is detected for the reconstructed

signal as found in the original direct signal. Additionally, it is feasible to differentiate between two surface properties (i.e. dielectric constant) from the DDMs generated from the reconstructed data. However, further research is required to validate and generalize this algorithm for more variations in surface properties.

Further, in Chapter 4, the target localisation using the GNSS-R technique and Doppler frequency bound calculation for the NavIC-L5 signal is explained. The GNSS signals can be used for target tracking and localization by receiving the GNSS signals in a multi-static or bi-static radar configuration. The target tracking and localization using GNSS-R can be realized by obtaining signals from multiple transmitting satellites and receiving them using a single receiver. In this work, we have examined the utility of GNSS-R based observations for target localisation, using the difference between the direct path length and the multipath range obtained from the multiple GNSS transmitters and a single receiver as a set of key observations. The obtained bistatic ranges are optimised using the Least square estimation technique for target localisation. Further, Doppler frequency bound calculation is necessary as it is required during the signal acquisition for target localisation applications. The theoretically calculated Doppler frequency search range for GPS satellite signal acquisition is ±5KHz, and ±10KHz [138], for the static and moving GPS receiver scenarios. This range for GPS signals is already defined in the literature. However, the Doppler frequency bound for the NavIC-L5 signal is not explicitly reported in the literature. In this work, the maximum and minimum Doppler frequency bound is defined based on the Doppler frequencies calculated at various surface target points. Using the calculated maximum and minimum Doppler frequency bound, the NavIC multipath signal acquisition is performed. The Doppler frequency bound is calculated for static as well as moving receiver scenarios. The Doppler bound for the static receiver is ±0.55 KHz and for the moving receiver case with a receiver on-board, an LEO satellite is ±3.7 KHz with the receiver velocity of 7.78 Km/s. The Doppler bound calculation presented in this work can be used to define the Doppler search range while performing the signal acquisition. It also helps to reduce the processing time for NavIC multipath signal acquisition during the GNSS-R analysis.

Finally, chapter 5 discusses the novel SDR-based multi-constellation reflectometry receiver to acquire reflected NavIC-L5 and GPS-L1 signals and demonstrate its potential for remote sensing

applications. This work is also a proof-of-concept of using NavIC-L5 signals for reflectometry. The proposed receiver's functionality is demonstrated through field experiments and verified using numerical simulation and a HIL simulator testbed. The field experiments are performed using the designed receiver to obtain the DDM using the GPS-L1 and NavIC-L5 signals. The field experiment results show that the proposed receiver is capable of receiving both direct (RHCP) and reflected (LHCP) GPS-L1 and NavIC-L5 RF signals and processing them into DDMs for performing reflectometry. The proposed receiver has a compact size and low power requirement and hence is suitable for performing remote sensing by using it as an air-borne or spaceborne GNSS-R receiver if radiation hardened.

6.2 Future Work

The research contributions presented in this thesis have addressed significant gaps in the existing studies while introducing innovative methodologies and advancements in the field of GNSS-Reflectometry (GNSS-R). By leveraging the unique capabilities of multi-constellation GNSS signals, including NavIC-L5 and GPS-L1, this work has expanded the potential applications of GNSS-R and laid the foundation for future developments in this research domain. Through the design and implementation of a novel SDR-based multi-constellation receiver, this research has demonstrated the feasibility of acquiring and processing reflected signals for remote sensing applications, offering compactness, efficiency, and scalability. The proposed methodologies and experimental results have opened doors for exploring new avenues, particularly in the context of environmental monitoring, agricultural applications, and climate studies. The work presented in this thesis can be further extended to the following research areas as mentioned below:

- **Testing and On-edge implementation of compression algorithms for GNSS RF signal:** In this thesis work, the compression of GNSS-RF signal is performed on simulated NavIC-L5 and TDS-1 GPS signals. While the current work has demonstrated the feasibility of signal compression in simulated environments, future research will focus on extending these algorithms to process NavIC-L5 signals obtained from field experiments. This step is crucial

for validating the performance of the algorithms under real-world conditions, where factors such as noise, interference, and multipath effects come into play. Furthermore, the integration of these compression algorithms directly onto satellite payloads represents a significant area of future exploration.

In satellite-based GNSS systems, efficient data transmission and storage are critical for optimizing bandwidth usage and preserving valuable onboard memory. By embedding these algorithms on the satellite itself, GNSS data can be processed in real-time at the satellite level, thereby reducing the need for transmitting raw data back to Earth. This approach not only conserves downlink bandwidth but also enables more autonomous and efficient satellite operations. Additionally, real-time onboard processing can enhance the responsiveness of GNSS-based applications, facilitating quicker decision-making for Earth observation, disaster management, and other critical uses. The implementation of such onboard compression techniques will involve addressing challenges related to computational constraints, energy efficiency, and system integration, paving the way for more robust and versatile GNSS-R systems in the future.

- **Experimental analysis of GNSS-R based moving target localisation:** As part of the future scope of this research, the focus will shift towards the experimental analysis of GNSS-R-based moving target localization, building on the foundation established through static target localization. The static localization technique developed in this work utilizes bistatic range optimization from multiple satellite signals. Specifically, four sets of measurements from four transmitting GNSS satellites received at a single receiver are analyzed to accurately determine the position of static targets.

  Extending this approach, future research will aim to enhance these techniques for the tracking and localization of moving targets. This will involve addressing the dynamic nature of moving targets and the associated challenges, such as varying reflection geometries, Doppler effects, and temporal signal variations. The future work will also focus on integrating theoretical advancements with experimental validations by employing a multi-frequency and multi-static radar configuration. The use of multiple frequencies and transmitter-receiver pairs will provide improved resolution, enabling robust tracking capabilities. Such advancements will be

particularly beneficial in maritime applications, where the detection and localization of moving targets, such as ships and other vessels, are critical for navigation, safety, and surveillance. This proposed extension of the work aims to contribute to the growing field of GNSS-R, pushing its boundaries towards dynamic target monitoring and enhancing its utility in real-world scenarios.

- **Development of a space-grade multi-constellation (GPS-L1 and NavIC-L5) reflectometry receiver:** The next phase of this research focuses on the development of a space-grade, multi-constellation GNSS-Reflectometry (GNSS-R) receiver capable of processing GPS-L1 and NavIC-L5 signals for deployment on satellite and airborne platforms. This phase involves the transformation of the proposed receiver into a space-grade payload, requiring meticulous adaptation to meet the stringent environmental, thermal, and radiation conditions of space. To ensure durability and reliability in such extreme environments, the receiver's components must undergo rigorous testing, including thermal vacuum testing, vibration analysis, and radiation hardening. Additionally, the design and characterization of a space-grade, multi-frequency antenna will be integral to this development. This antenna must support the simultaneous reception of both direct and reflected signals from multiple constellations, ensuring high sensitivity and robustness.

  A critical aspect of this next phase is the integration of the Software-Defined Radio (SDR) receiver and Raspberry Pi (RPI)-based processing system onto a single Field-Programmable Gate Array (FPGA) platform. This compact design will significantly enhance the system's efficiency by reducing hardware complexity and streamlining the simultaneous processing of NavIC-L5 and GPS-L1 signals. The FPGA platform will facilitate high-speed signal acquisition and real-time processing of direct and reflected signals, enabling the generation of Delay-Doppler Maps (DDMs) with greater precision. The proposed integration will also reduce power consumption and improve the overall payload's suitability for deployment on resource-constrained platforms, such as small satellites or UAVs.

  Alongside the hardware development, this phase will involve an extensive exploration of potential applications for the space-grade receiver. One primary application is soil moisture estimation, a critical parameter for agricultural monitoring and environmental studies. Soil

moisture data derived from GNSS-R signals can provide valuable insights for optimizing irrigation practices, assessing drought conditions, and enhancing crop yield predictions. Furthermore, the spaceborne GNSS-R receiver will have the capability to contribute to a wide range of Earth observation studies, including ocean altimetry, wetland mapping, and ice sheet monitoring, further advancing our understanding of global climate dynamics. By addressing both the technical and application-oriented challenges, this phase aims to establish the receiver as a versatile, reliable, and impactful tool for GNSS-Reflectometry in spaceborne and airborne remote sensing missions.

Bibliography

[1] J. Park, J. T. Johnson, A. O'Brien, and S. T. Lowe, "Studies of TDS-1 GNSS-R ocean altimetry using a 'full DDM' retrieval approach," in *International Geoscience and Remote Sensing Symposium (IGARSS)*, 2016.

[2] K. Yu, C. Rizos, D. Burrage, A. G. Dempster, K. Zhang, and M. Markgraf, "An overview of GNSS remote sensing," *Eurasip Journal on Advances in Signal Processing*, vol. 2014, no. 1, pp. 1–14, 2014.

[3] J. Wickert, G. Dick, T. Schmidt, M. Asgarimehr, N. Antonoglou, C. Arras, A. Brack, M. Ge, A. Kepkar, B. Männel, C. Nguyen, O. Seun, H. Schuh, M. Semmling, T. Simeonov, S. Vey, K. Wilgan, and F. Zus, "GNSS Remote Sensing at GFZ: Overview and Recent Results," *ZFV - Zeitschrift fur Geodasie, Geoinformation und Landmanagement*, vol. 145, pp. 266–278, 9 2020.

[4] S. Gleason, S. Hodgart, Y. Sun, C. Gommenginger, S. Mackin, M. Adjrad, and M. Unwin, "Detection and processing of bistatically reflected GPS signals from low earth orbit for the purpose of ocean remote sensing," *IEEE Transactions on Geoscience and Remote Sensing*, vol. 43, no. 6, pp. 1229–1241, 6 2005.

[5] P. T. Setti and S. Tabibi, "Evaluation of Spire GNSS-R reflectivity from multiple GNSS constellations for soil moisture estimation," *International Journal of Remote Sensing*, vol. 44, no. 20, pp. 6422–6441, 2023.

[6] Y. Zhu, F. Gao, Y. Kong, X. Li, H. Sun, N. Wang, M. Wang, C. Qian, L. Wang, and T. Xu, "Analysis of Drone-Based GNSS-R Soil Moisture Retrieval From QZSS GEO L5-Band Signal," *IEEE Geoscience and Remote Sensing Letters*, 2024.

[7] R. Imam, M. Pini, G. Marucco, F. Dominici, and F. Dovis, "UAV-based GNSS-R for water detection as a support to flood monitoring operations: A feasibility study," *Applied Sciences*, vol. 10, no. 1, p. 210, 2019.

[8] C.-a. Liu, Z.-X. Chen, S. Yun, J.-s. Chen, T. Hasi, and H.-z. PAN, "Research advances of SAR remote sensing for agriculture applications: A review," *Journal of integrative agriculture*, vol. 18, no. 3, pp. 506–525, 2019.

[9] F. Van der Meer, "Remote-sensing image analysis and geostatistics," *International Journal of Remote Sensing*, vol. 33, no. 18, pp. 5644–5676, 2012.

[10] M. Antoniou and M. Cherniakov, "GNSS-based bistatic SAR: a signal processing view," *EURASIP Journal on Advances in Signal Processing*, vol. 2013, no. 1, p. 98, 2013. [Online]. Available: https://doi.org/10.1186/1687-6180-2013-98

[11] M. Cherniakov and T. Zeng, "Passive Bistatic SAR with GNSS Transmitters," in *Bistatic Radar*, 2 2008, pp. 339–361. [Online]. Available: https://doi.org/10.1002/9780470985755.ch9

[12] R. N. Treuhaft, S. T. Lowe, C. Zuffada, and Y. Chao, "2-cm GPS altimetry over Crater lake," *Geophysical Research Letters*, 2001.

[13] M. Martin-Neira, "A passive reflectometry and interferometry system (PARIS): Application to ocean altimetry," *ESA journal*, vol. 17, no. 4, pp. 331–355, 1993.

[14] E. D. Gutmann, K. M. Larson, M. W. Williams, F. G. Nievinski, and V. Zavorotny, "Snow measurement by GPS interferometric reflectometry: an evaluation at Niwot Ridge, Colorado," *Hydrological Processes*, vol. 26, no. 19, pp. 2951–2961, 2012.

[15] W. Zhou, L. Liu, L. Huang, Y. Yao, J. Chen, and S. Li, "A New GPS SNR-based Combination Approach for Land Surface Snow Depth Monitoring," *Scientific Reports*, vol. 9, no. 1, 12 2019.

[16] K. M. Larson, J. J. Braun, E. E. Small, V. U. Zavorotny, E. D. Gutmann, and A. L. Bilich, "GPS Multipath and Its Relation to Near-Surface Soil Moisture Content," *IEEE Journal of Selected Topics in Applied Earth Observations and Remote Sensing*, 2010.

[17] M. P. Clarizia, N. Pierdicca, F. Costantini, and N. Floury, "Analysis of cygnss data for soil moisture retrieval," *IEEE Journal of Selected Topics in Applied Earth Observations and Remote Sensing*, vol. 12, no. 7, pp. 2227–2235, 7 2019.

[18] Z. Li, F. Guo, F. Chen, Z. Zhang, and X. Zhang, "Wind speed retrieval using GNSS-R technique with geographic partitioning," *Satellite Navigation*, vol. 4, no. 1, p. 4, 2023. [Online]. Available: https://doi.org/10.1186/s43020-022-00093-z

[19] C. Zuffada, C. Chew, and S. V. Nghiem, "Global Navigation Satellite System Reflectometry (GNSS-R) algorithms for wetland observations," in *International Geoscience and Remote Sensing Symposium (IGARSS)*, 2017.

[20] A. Di Simone, A. Iodice, D. Riccio, A. Camps, and H. Park, "GNSS-R: A useful tool for sea target detection in near real-Time," in *RTSI 2017 - IEEE 3rd International Forum on Research and Technologies for Society and Industry, Conference Proceedings*, 2017.

[21] B. J. Southwell, J. W. Cheong, and A. G. Dempster, "A Matched Filter for Spaceborne GNSS-R Based Sea-Target Detection," *IEEE Transactions on Geoscience and Remote Sensing*, vol. 58, no. 8, pp. 5922–5931, 2020.

[22] D. Moller, C. Ruf, R. Linnabary, A. O'Brien, and S. Musko, "Operational airborne gnss-r aboard air new zealand domestic aircraft," in *2021 IEEE International Geoscience and Remote Sensing Symposium IGARSS*. IEEE, 2021, pp. 1284–1287.

[23] M. P. Clarizia, C. P. Gommenginger, S. T. Gleason, M. A. Srokosz, C. Galdi, and M. Di Bisceglie, "Analysis of GNSS-R delay-Doppler maps from the UK-DMC satellite over the ocean," *Geophysical Research Letters*, vol. 36, no. 2, 1 2009.

[24] K. M. Larson, E. E. Small, E. D. Gutmann, A. L. Bilich, J. J. Braun, and V. U. Zavorotny, "Use of GPS receivers as a soil moisture network for water cycle studies," *Geophysical Research Letters*, 2008.

[25] N. Rodríguez Álvarez, "Contributions to earth observation using gnss-r opportunity signals," 2011.

[26] L. Zhu, J. Suomalainen, J. Liu, J. Hyyppä, Harri
}Kaartinen, and H. Haggren, "A Review: Remote Sensing Sensors," in *Multi-purposeful Application of Geospatial Data*, R. B. Rustamov, S. Hasanova, and M. H. Zeynalova, Eds. Rijeka: IntechOpen, 2017, p. Ch. 2. [Online]. Available: https://doi.org/10.5772/intechopen.71049

[27] X. Wang, "Remote Sensing Applications to Climate Change," 2 2023.

[28] B. Thies and J. Bendix, "Satellite based remote sensing of weather and climate: Recent achievements and future perspectives," pp. 262–295, 2011.

[29] J. Yang, P. Gong, R. Fu, M. Zhang, J. Chen, S. Liang, B. Xu, J. Shi, and R. Dickinson, "The role of satellite remote sensing in climate change studies," *Nature Climate Change*, vol. 3, no. 10, pp. 875–883, 2013. [Online]. Available: https://doi.org/10.1038/nclimate1908

[30] K. E. Joyce, S. E. Belliss, S. V. Samsonov, S. J. McNeill, and P. J. Glassey, "A review of the status of satellite remote sensing and image processing techniques for mapping natural hazards and disasters," *Progress in Physical Geography: Earth and Environment*, vol. 33, no. 2, pp. 183–207, 4 2009. [Online]. Available: https://doi.org/10.1177/0309133309339563

[31] A. Dielacher, H. Fragner, O. Koudelka, P. Beck, J. Wickert, E. Cardellach, and P. Høeg, "The ESA passive reflectometry and dosimetry (PRETTY) mission," in *IGARSS 2019-2019 IEEE International Geoscience and Remote Sensing Symposium*. IEEE, 2019, pp. 5173–5176.

[32] H. Carreno-Luengo, S. Lowe, C. Zuffada, S. Esterhuizen, and S. Oveisgharan, "Spaceborne GNSS-R from the SMAP mission: First assessment of polarimetric scatterometry over land and cryosphere," *Remote Sensing*, vol. 9, no. 4, p. 362, 2017.

[33] M. J. Unwin, N. Pierdicca, E. Cardellach, K. Rautiainen, G. Foti, P. Blunt, L. Guerriero, E. Santi, and M. Tossaint, "An introduction to the HydroGNSS GNSS reflectometry remote sensing mission," *IEEE Journal of Selected Topics in Applied Earth Observations and Remote Sensing*, vol. 14, pp. 6987–6999, 2021.

[34] E. Chuvieco, *Fundamentals of satellite remote sensing: An environmental approach*. CRC press, 2020.

[35] R. Stosius, G. Beyerle, M. Semmling, A. Helm, A. Hoechner, J. Wickert, and J. Lauterjung, "Tsunami detection from space using GNSS Reflections: Results and activities from GFZ," in *2010 IEEE International Geoscience and Remote Sensing Symposium*, 2010, pp. 3047–3050.

[36] C. S. Ruf, S. Gleason, Z. Jelenak, S. Katzberg, A. Ridley, R. Rose, J. Scherrer, and V. Zavorotny, "The CYGNSS nanosatellite constellation hurricane mission," in *2012 IEEE international geoscience and remote sensing symposium*. IEEE, 2012, pp. 214–216.

[37] A. A. Thompson*, "Overview of the RADARSAT constellation mission," *Canadian Journal of Remote Sensing*, vol. 41, no. 5, pp. 401–407, 2015.

[38] O. Lang, P. Lumsdon, D. Walter, J. Anderssohn, W. Koppe, J. Janoth, T. Koban, and C. Stahl, "Development of operational applications for TerraSAR-X," *Remote Sensing*, vol. 10, no. 10, 10 2018.

[39] F. Spoto, O. Sy, P. Laberinti, P. Martimort, V. Fernandez, O. Colin, B. Hoersch, and A. Meygret, "Overview of sentinel-2," in *2012 IEEE international geoscience and remote sensing symposium*. IEEE, 2012, pp. 1707–1710.

[40] D. L. Williams, S. Goward, and T. Arvidson, "Landsat," *Photogrammetric Engineering & Remote Sensing*, vol. 72, no. 10, pp. 1171–1178, 2006.

[41] F. T. Ulaby, R. K. Moore, and A. K. Fung, "Microwave remote sensing: Active and passive. volume 1-microwave remote sensing fundamentals and radiometry," 1981.

[42] D. S. Masters, *Surface remote sensing applications of GNSS bistatic radar: Soil moisture and aircraft altimetry*. University of Colorado at Boulder, 2004.

[43] D. Masters, P. Axelrad, and S. Katzberg, "Initial results of land-reflected GPS bistatic radar measurements in SMEX02," *Remote sensing of environment*, vol. 92, no. 4, pp. 507–520, 2004.

[44] V. U. Zavorotny and A. G. Voronovich, "Scattering of GPS signals from the ocean with wind remote sensing application," *IEEE Transactions on Geoscience and Remote Sensing*, vol. 38, no. 2, pp. 951–964, 2000.

[45] L. Guerriero, N. Pierdicca, L. Pulvirenti, and P. Ferrazzoli, "Use of satellite radar bistatic measurements for crop monitoring: A simulation study on corn fields," *Remote Sensing*, vol. 5, no. 2, pp. 864–890, 2013.

[46] K. Yu, S. Han, J. Bu, Y. An, Z. Zhou, C. Wang, S. Tabibi, and J. W. Cheong, "Spaceborne GNSS Reflectometry," 4 2022.

[47] M. Unwin, S. Gleason, and M. Brennan, "The space GPS reflectometry experiment on the UK disaster monitoring constellation satellite," in *Proceedings of the 16th International Technical Meeting of the Satellite Division of The Institute of Navigation (ION GPS/GNSS 2003)*, 2003, pp. 2656–2663.

[48] M. P. Clarizia, C. Ruf, P. Cipollini, and C. Zuffada, "First spaceborne observation of sea surface height using GPS-Reflectometry," *Geophysical Research Letters*, vol. 43, no. 2, pp. 767–774, 2016.

[49] T. Peres, R. Castro, J. Carola, T. Mendes, R. Capote, J. Bandeiras, J. Silva, N. Catarino, and P. F. Silva, "GNSS-Reflectometry Observables with Galileo E5 Signals," in *Proceedings of the 28th International Technical Meeting of the Satellite Division of The Institute of Navigation (ION GNSS+ 2015)*, 2015, pp. 3869–3874.

[50] P. J. Jales, R. M. Weiler, C. Underwood, and M. Unwin, "First spaceborne demonstration of Galileo signals for GNSS reflectometry," in *Proceedings of the 21st International Technical Meeting of the Satellite Division of The Institute of Navigation (ION GNSS 2008)*, 2008, pp. 736–745.

[51] T. Hobiger, R. Haas, and J. S. Löfgren, "GLONASS-R: GNSS reflectometry with a Frequency Division Multiple Access-based satellite navigation system," *Radio Science*, vol. 49, no. 4, pp. 271–282, 2014.

[52] S. Jin, X. Qian, and X. Wu, "Sea level change from BeiDou Navigation Satellite System-Reflectometry (BDS-R): first results and evaluation," *Global and planetary change*, vol. 149, pp. 20–25, 2017.

[53] L. I. Weiqiang, E. Cardellach, R. Serni, R. Antonio, and Z. Bo, "First spaceborne demonstration of BeiDou-3 signals for GNSS reflectometry from CYGNSS constellation," *Chinese Journal of Aeronautics*, vol. 34, no. 9, pp. 1–10, 2021.

[54] V. Chamoli, R. Prakash, A. Vidyarthi, and A. Ray, "Sensitivity of NavIC Signal for Soil moisture variation," Tech. Rep.

[55] C. D. Hall and R. A. Cordey, "Multistatic scatterometry," in *International Geoscience and Remote Sensing Symposium,'Remote Sensing: Moving Toward the 21st Century'.*, vol. 1. IEEE, 1988, pp. 561–562.

[56] J. Strandberg, T. Hobiger, and R. Haas, "Improving GNSS-R sea level determination through inverse modeling of SNR data," *Radio science*, vol. 51, no. 8, pp. 1286–1296, 2016.

[57] A. Rius, O. Nogués-Correig, S. Ribó, E. Cardellach, S. Oliveras, E. Valencia, H. Park, J. M. Tarongí, A. Camps, and H. van der Marel, "Altimetry with GNSS-R interferometry: First proof of concept experiment," *GPS solutions*, vol. 16, pp. 231–241, 2012.

[58] W. Li, E. Cardellach, F. Fabra, A. Rius, S. Ribó, and M. Martín-Neira, "First spaceborne phase altimetry over sea ice using TechDemoSat-1 GNSS-R signals," *Geophysical Research Letters*, vol. 44, no. 16, pp. 8369–8376, 2017.

[59] J. L. Garrison and S. J. Katzberg, "Detection of ocean reflected GPS signals: Theory and experiment," in *Proceedings IEEE SOUTHEASTCON'97.'Engineering the New Century'.* IEEE, 1997, pp. 290–294.

[60] N. Rodriguez-Alvarez, D. M. Akos, V. U. Zavorotny, J. A. Smith, A. Camps, and C. W. Fairall, "Airborne GNSS-R wind retrievals using delay–Doppler maps," *IEEE transactions on geoscience and remote sensing*, vol. 51, no. 1, pp. 626–641, 2012.

[61] Y. Jia, P. Savi, Y. Pei, and R. Notarpietro, "GNSS reflectometry for remote sensing of soil moisture," in *2015 IEEE 1st International Forum on Research and Technologies for Society and Industry, RTSI 2015 - Proceedings.* Institute of Electrical and Electronics Engineers Inc., 11 2015, pp. 498–501.

[62] N. Rodriguez-Alvarez, X. Bosch-Lluis, A. Camps, M. Vall-Llossera, E. Valencia, J. F. Marchan-Hernandez, and I. Ramos-Perez, "Soil moisture retrieval using GNSS-R techniques: Experimental results over a bare soil field," *IEEE transactions on geoscience and remote sensing*, vol. 47, no. 11, pp. 3616–3624, 2009.

[63] F. Wang, D. Yang, B. Zhang, and W. Li, "Waveform-based spaceborne GNSS-R wind speed observation: Demonstration and analysis using UK TechDemoSat-1 data," *Advances in Space Research*, vol. 61, no. 6, pp. 1573–1587, 2018.

[64] V. U. Zavorotny, S. Gleason, E. Cardellach, and A. Camps, "Tutorial on remote sensing using GNSS bistatic radar of opportunity," *IEEE Geoscience and Remote Sensing Magazine*, vol. 2, no. 4, pp. 8–45, 2014.

[65] N. Rodriguez-Alvarez, A. Aguasca, E. Valencia, X. Bosch-Lluis, I. Ramos-Pérez, H. Park, A. Camps, and M. Vall-Llossera, "Snow monitoring using GNSS-R techniques," in *2011 IEEE International Geoscience and Remote Sensing Symposium*. IEEE, 2011, pp. 4375–4378.

[66] J. S. Lfgren, R. Haas, H. G. Scherneck, and M. S. Bos, "Three months of local sea level derived from reflected GNSS signals," *Radio Science*, vol. 46, no. 6, 2011.

[67] F. Soulat, M. Caparrini, O. Germain, P. Lopez-Dekker, M. Taani, and G. Ruffini, "Sea state monitoring using coastal GNSS-R," *Geophysical research letters*, vol. 31, no. 21, 2004.

[68] C. C. Chew, E. E. Small, K. M. Larson, and V. U. Zavorotny, "Vegetation sensing using GPS-interferometric reflectometry: Theoretical effects of canopy parameters on signal-to-noise ratio data," *IEEE Transactions on Geoscience and Remote Sensing*, vol. 53, no. 5, 2015.

[69] X. Wu, P. Guo, Y. Sun, H. Liang, X. Zhang, and W. Bai, "Recent progress on vegetation remote sensing using spaceborne GNSS-reflectometry," *Remote Sensing*, vol. 13, no. 21, p. 4244, 2021.

[70] M. P. Clarizia, C. Gommenginger, S. Gleason, C. Galdi, and M. Unwin, "Global navigation satellite system-reflectometry (GNSS-R) from the UK-DMC satellite for remote sensing of the ocean surface," in *IGARSS 2008-2008 IEEE International Geoscience and Remote Sensing Symposium*, vol. 1. IEEE, 2008, pp. I–276.

[71] J. Park, J. T. Johnson, A. O'brien, and S. T. Lowe, "A Study of Ocean Altimetry Performance for the CYGNSS Mission," Tech. Rep., 2015.

[72] F. Saïd, S. Soisuvarn, Z. Jelenak, and P. S. Chang, "Performance Assessment of Simulated CYGNSS Measurements in the Tropical Cyclone Environment," *IEEE Journal of Selected Topics in Applied Earth Observations and Remote Sensing*, vol. 9, no. 10, pp. 4709–4719, 2016.

[73] C. S. Ruf, R. Atlas, P. S. Chang, M. P. Clarizia, J. L. Garrison, S. Gleason, S. J. Katzberg, Z. Jelenak, J. T. Johnson, and S. J. Majumdar, "New ocean winds satellite mission to probe hurricanes and tropical convection," *Bulletin of the American Meteorological Society*, vol. 97, no. 3, pp. 385–395, 2016.

[74] C. Ruf, S. Gleason, A. Ridley, R. Rose, and J. Scherrer, "The nasa cygnss mission: Overview and status update," in *2017 IEEE International Geoscience and Remote Sensing Symposium (IGARSS)*, 2017, pp. 2641–2643.

[75] P. Jales, J. Cartwright, M. Talpe, J. Mashburn, T. Yuasa, O. Nogues-Correig, V. Nguyen, and V. Freeman, "Spire Global's Operational GNSS-Reflectometry Constellation for Earth Surface Observations," in *IGARSS 2023 - 2023 IEEE International Geoscience and Remote Sensing Symposium*, 2023, pp. 884–887.

[76] J. F. Munoz-Martin, L. F. Capon, J. A. Ruiz-de Azua, and A. Camps, "The Flexible Microwave Payload-2: A SDR-Based GNSS-Reflectometer and L-Band Radiometer for CubeSats," *IEEE Journal of Selected Topics in Applied Earth Observations and Remote Sensing*, vol. 13, pp. 1298–1311, 2020.

[77] H. Fragner, A. Dielacher, M. Moritsch, J. Wickert, O. Koudelka, P. Høeg, E. Cardellach, M. Martín-Neira, M. Semmling, and R. Walker, "Status of the ESA Pretty mission," in *IGARSS 2020-2020 IEEE International Geoscience and Remote Sensing Symposium*. IEEE, 2020, pp. 3345–3348.

[78] D. Comite, E. Cardellach, L. Dente, L. Guerriero, W. Li, N. Pierdicca, K. Rautiainen, E. Santi, M. Unwin, M. P. Clarizia, M. Pastena, and J. P. Lejault, "GNSS-R for Sustainable Development: A Review of the Geophysical Variables Addressed by the Hydrognss Mission," in *IGARSS 2022 - 2022 IEEE International Geoscience and Remote Sensing Symposium*, 2022, pp. 4216–4219.

[79] M. Unwin, P. Jales, J. Tye, C. Gommenginger, G. Foti, and J. Rosello, "Spaceborne GNSS-reflectometry on TechDemoSat-1: Early mission operations and exploitation," *IEEE Journal of Selected Topics in Applied Earth Observations and Remote Sensing*, vol. 9, no. 10, pp. 4525–4539, 2016.

[80] D. Masters, "Design and planning for the first spire GNSS-R missions of 2019," in *Proc. IEEE GRSS, Spec. Meeting Reflectometry Using GNSS Other Signals Opportunity*, 2019.

[81] S. Jin, A. Camps, Y. Jia, F. Wang, M. Martin-Neira, F. Huang, Q. Yan, S. Zhang, Z. Li, K. Edokossi, D. Yang, Z. Xiao, Z. Ma, and W. Bai, "Remote sensing and its applications using GNSS reflected signals: advances and prospects," 12 2024.

[82] M. Song, X. He, X. Wang, D. Jia, R. Xiao, H. Shi, and Y. Wu, "Study on the Exploration of Spaceborne GNSS-R Raw Data Focusing on Altimetry," *IEEE Journal of Selected Topics in Applied Earth Observations and Remote Sensing*, vol. 13, pp. 6142–6154, 2020.

[83] H. Park, E. Valencia, A. Camps, A. Rius, S. Ribo, and M. Martin-Neira, "Delay Tracking in Spaceborne GNSS-R Ocean Altimetry," *IEEE Geoscience and Remote Sensing Letters*, vol. 10, no. 1, pp. 57–61, 2013.

[84] E. Cardellach, W. Li, A. Rius, M. Semmling, J. Wickert, F. Zus, C. S. Ruf, and C. Buontempo, "First Precise Spaceborne Sea Surface Altimetry With GNSS Reflected Signals," *IEEE Journal of Selected Topics in Applied Earth Observations and Remote Sensing*, vol. 13, pp. 102–112, 2020.

[85] N. Rodriguez-Alvarez, R. Acevo, A. Aguasca, E. Valencia, A. Camps, M. Vall-llossera, X. Bosch-Lluis, and I. Ramos-Perez, "Altimetry study performed using an airborne GNSS-Reflectometer," in *2010 IEEE International Geoscience and Remote Sensing Symposium*, 2010, pp. 3833–3836.

[86] H. Carreno-Luengo, H. Park, A. Camps, F. Fabra, and A. Rius, "GNSS-R Derived Centimetric Sea Topography: An Airborne Experiment Demonstration," *IEEE Journal of Selected Topics in Applied Earth Observations and Remote Sensing*, vol. 6, no. 3, pp. 1468–1478, 2013.

[87] Y. Zhang, F. Liu, Q. Gu, W. Meng, Z. Hong, and Y. Han, "Study of accurate ocean-altimetry with GNSS-R," in *2013 IEEE International Geoscience and Remote Sensing Symposium - IGARSS*, 2013, pp. 1410–1413.

[88] M. Martm-Neira, M. Caparrini, J. Font-Rossello, S. Lannelongue, and C. S. Vallmitjana, "The paris concept: an experimental demonstration of sea surface altimetry using gps reflected signals," *IEEE Transactions on Geoscience and Remote Sensing*, vol. 39, no. 1, pp. 142–150, 2001.

[89] K. M. Larson, E. E. Small, E. Gutmann, A. Bilich, P. Axelrad, and J. Braun, "Using GPS multipath to measure soil moisture fluctuations: Initial results," *GPS Solutions*, 2008.

[90] A. Camps, H. Park, M. Pablos, G. Foti, C. Gommenginger, P. W. Liu, and J. Judge, "Soil moisture and vegetation impact in GNSS-R TechDemosat-1 observations," in *International Geoscience and Remote Sensing Symposium (IGARSS)*, 2016.

[91] A. Camps, H. Park, M. Pablos, G. Foti, C. P. Gommenginger, P. W. Liu, and J. Judge, "Sensitivity of GNSS-R Spaceborne Observations to Soil Moisture and Vegetation," *IEEE Journal of Selected Topics in Applied Earth Observations and Remote Sensing*, vol. 9, no. 10, pp. 4730–4742, 2016.

[92] N. Wang, F. Gao, Y. Kong, T. Xu, L. Jing, L. Yang, Y. He, W. Yang, X. Meng, and B. Ning, "Soil Moisture Estimation Based on GNSS-R Using L5 Signals From a Quasi-Zenith Satellite System," *IEEE Geoscience and Remote Sensing Letters*, vol. 19, pp. 1–5, 2022.

[93] A. Bilich, K. M. Larson, and P. Axelrad, "Modeling GPS phase multipath with SNR: Case study from the Salar de Uyuni, Boliva," *Journal of Geophysical Research: Solid Earth*, vol. 113, no. 4, 4 2008.

[94] E. G. Njoku and D. Entekhabi, "Passive microwave remote sensing of soil moisture," *Journal of Hydrology*, vol. 184, no. 1, pp. 101–129, 1996. [Online]. Available: https://www.sciencedirect.com/science/article/pii/0022169495029702

[95] X. Wu, W. Ma, J. Xia, W. Bai, S. Jin, and A. Calabia, "Spaceborne GNSS-R Soil Moisture Retrieval: Status, Development Opportunities, and Challenges," *Remote Sensing*, vol. 13, no. 1, 2021. [Online]. Available: https://www.mdpi.com/2072-4292/13/1/45

[96] J. Mashburn, P. Axelrad, S. T. Lowe, and K. M. Larson, "Global Ocean Altimetry With GNSS Reflections From TechDemoSat-1," *IEEE Transactions on Geoscience and Remote Sensing*, vol. 56, no. 7, pp. 4088–4097, 2018.

[97] W. Li, E. Cardellach, F. Fabra, S. Ribó, and A. Rius, "Assessment of Spaceborne GNSS-R Ocean Altimetry Performance Using CYGNSS Mission Raw Data," *IEEE Transactions on Geoscience and Remote Sensing*, vol. 58, no. 1, pp. 238–250, 2020.

[98] C. Ruf, M. Unwin, J. Dickinson, R. Rose, D. Rose, M. Vincent, and A. Lyons, "CYGNSS: Enabling the Future of Hurricane Prediction [Remote Sensing Satellites]," *IEEE Geoscience and Remote Sensing Magazine*, vol. 1, no. 2, pp. 52–67, 2013.

[99] M. P. Clarizia and C. S. Ruf, "Wind Speed Retrieval Algorithm for the Cyclone Global Navigation Satellite System (CYGNSS) Mission," *IEEE Transactions on Geoscience and Remote Sensing*, vol. 54, no. 8, pp. 4419–4432, 2016.

[100] C. Chew, R. Shah, C. Zuffada, G. Hajj, D. Masters, and A. J. Mannucci, "Demonstrating soil moisture remote sensing with observations from the UK TechDemoSat-1 satellite mission," *Geophysical Research Letters*, vol. 43, no. 7, pp. 3317–3324, 4 2016.

[101] M. Rahmani, J. Asgari, and M. Asgarimehr, "Soil moisture retrieval using spaceborne GNSS reflectometry: a comprehensive review," *International Journal of Remote Sensing*, vol. 43, no. 14, pp. 5173–5203, 7 2022. [Online]. Available: https://doi.org/10.1080/01431161.2022.2128927

[102] M. M. Al-Khaldi, J. T. Johnson, A. J. O'Brien, A. Balenzano, and F. Mattia, "Time-Series Retrieval of Soil Moisture Using CYGNSS," *IEEE Transactions on Geoscience and Remote Sensing*, vol. 57, no. 7, pp. 4322–4331, 7 2019.

[103] M. K. Rohil and S. Mathur, "CYGNSS-derived soil moisture: Status, challenges and future," *Ecological Informatics*, vol. 69, p. 101621, 2022. [Online]. Available: https://www.sciencedirect.com/science/article/pii/S157495412200070X

[104] Z. Dong, S. Jin, L. Li, and P. Wang, "Validation of CYGNSS soil moisture products using in situ measurements: a case study of Southern China," *Theoretical and Applied Climatology*, vol. 153, no. 3, pp. 1085–1103, 2023. [Online]. Available: https://doi.org/10.1007/s00704-023-04531-z

[105] T. P. Barnett, J. C. Adam, and D. P. Lettenmaier, "Potential impacts of a warming climate on water availability in snow-dominated regions," *Nature*, vol. 438, no. 7066, pp. 303–309, 2005. [Online]. Available: https://doi.org/10.1038/nature04141

[106] K. M. Larson and E. E. Small, "Estimation of Snow Depth Using L1 GPS Signal-to-Noise Ratio Data," *IEEE Journal of Selected Topics in Applied Earth Observations and Remote Sensing*, vol. 9, no. 10, 2016.

[107] K. M. Larson, E. D. Gutmann, V. U. Zavorotny, J. J. Braun, M. W. Williams, and F. G. Nievinski, "Can we measure snow depth with GPS receivers?" *Geophysical Research Letters*, vol. 36, no. 17, 9 2009.

[108] S. Tabibi, F. Geremia-Nievinski, and T. v. Dam, "Statistical Comparison and Combination of GPS, GLONASS, and Multi-GNSS Multipath Reflectometry Applied to Snow Depth Retrieval," *IEEE Transactions on Geoscience and Remote Sensing*, vol. 55, no. 7, pp. 3773–3785, 2017.

[109] S. Vey, A. Guntner, J. Wickert, T. Blume, H. Thoss, and M. Ramatschi, "Monitoring Snow Depth by GNSS Reflectometry in Built-up Areas: A Case Study for Wettzell, Germany," *IEEE Journal of Selected Topics in Applied Earth Observations and Remote Sensing*, 2016.

[110] K. Yu, Y. Li, T. Jin, X. Chang, Q. Wang, and J. Li, "GNSS-R-Based Snow Water Equivalent Estimation with Empirical Modeling and Enhanced SNR-Based Snow Depth Estimation," *Remote Sensing*, vol. 12, no. 23, 2020. [Online]. Available: https://www.mdpi.com/2072-4292/12/23/3905

[111] W. Ban, K. Yu, and X. Zhang, "GEO-Satellite-Based Reflectometry for Soil Moisture Estimation: Signal Modeling and Algorithm Development," *IEEE Transactions on Geoscience and Remote Sensing*, vol. 56, no. 3, pp. 1829–1838, 3 2018.

[112] K. M. Larson and F. G. Nievinski, "GPS snow sensing: Results from the EarthScope Plate Boundary Observatory," *GPS Solutions*, vol. 17, no. 1, pp. 41–52, 1 2013.

[113] Q. Chen, D. Won, and D. M. Akos, "Snow depth sensing using the GPS L2C signal with a dipole antenna," *EURASIP Journal on Advances in Signal Processing*, vol. 2014, no. 1, p. 106, 2014. [Online]. Available: https://doi.org/10.1186/1687-6180-2014-106

[114] S. Zhang, J. Peng, C. Zhang, J. Zhang, L. Wang, T. Wang, and Q. Liu, "GiRsnow: an open-source software for snow depth retrievals using GNSS interferometric reflectometry," *GPS Solutions*, vol. 25, no. 2, p. 55, 2021. [Online]. Available: https://doi.org/10.1007/s10291-021-01096-0

[115] S. Jin, X. Qian, and H. Kutoglu, "Snow depth variations estimated from GPS-reflectometry: A case study in Alaska from L2P SNR data," *Remote Sensing*, 2016.

[116] F. Fabra, E. Cardellach, A. Rius, S. Ribo, S. Oliveras, O. Nogues-Correig, M. B. Rivas, M. Semmling, and S. D'Addio, "Phase Altimetry With Dual Polarization GNSS-R Over Sea Ice," *IEEE Transactions on Geoscience and Remote Sensing*, vol. 50, no. 6, pp. 2112–2121, 2012.

[117] W. Yang, F. Guo, X. Zhang, T. Xu, N. Wang, and L. Jing, "Daily landscape freeze/thaw state detection using spaceborne GNSS-R data in Qinghai-Tibet Plateau," *IEEE Transactions on Geoscience and Remote Sensing*, 2023.

[118] Z. Zhang, F. Guo, X. Zhang, Z. Li, and H. Liu, "Physical modeling and compensation for systematic negative errors in GNSS-R snow depth retrieval," *IEEE transactions on geoscience and remote sensing*, vol. 61, pp. 1–12, 2023.

[119] E. Pinat, P. Defraigne, N. Bergeot, J.-M. Chevalier, and B. Bertrand, "Long-Term Snow Height Variations in Antarctica from GNSS Interferometric Reflectometry," *Remote Sensing*, vol. 13, no. 6, 2021. [Online]. Available: https://www.mdpi.com/2072-4292/13/6/1164

[120] C. C. Chew, R. Shah, C. Zuffada, and A. J. Mannucci, "Wetland mapping and measurement of flood inundated area using ground-reflected GNSS signals in a bistatic radar system," in *2016 IEEE International Geoscience and Remote Sensing Symposium (IGARSS)*, 2016, pp. 7184–7187.

[121] S. V. Nghiem, C. Zuffada, R. Shah, C. Chew, S. T. Lowe, A. J. Mannucci, E. Cardellach, G. R. Brakenridge, G. Geller, and A. Rosenqvist, "Wetland monitoring with global navigation satellite system reflectometry," *Earth and Space Science*, vol. 4, no. 1, pp. 16–39, 2017.

[122] E. Cardellach, F. Fabra, O. Nogués-Correig, S. Oliveras, S. Ribó, and A. Rius, "GNSS-R ground-based and airborne campaigns for ocean, land, ice, and snow techniques: Application to the GOLD-RTR data sets," *Radio Science*, vol. 46, no. 5, 2011.

[123] J. F. Marchan-Hernandez, E. Valencia, N. Rodriguez-Alvarez, I. Ramos-Pérez, X. Bosch-Lluis, A. Camps, F. Eugenio, and J. Marcello, "Sea-state determination using GNSS-R data," *IEEE Geoscience and Remote Sensing Letters*, vol. 7, no. 4, pp. 621–625, 2010.

[124] E. Valencia, A. Camps, N. Rodriguez-Alvarez, I. Ramos-Perez, X. Bosch-Lluis, and H. Park, "Improving the accuracy of sea surface salinity retrieval using GNSS-R data to correct the sea state effect," *Radio Science*, vol. 46, no. 06, pp. 1–11, 2011.

[125] B. Liu, W. Wan, and Y. Hong, "Can the accuracy of sea surface salinity measurement be improved by incorporating spaceborne GNSS-reflectometry?" *IEEE Geoscience and Remote Sensing Letters*, vol. 18, no. 1, pp. 3–7, 2020.

[126] E. Valencia, A. Camps, N. Rodriguez-Alvarez, H. Park, and I. Ramos-Perez, "Using GNSS-R imaging of the ocean surface for oil slick detection," *IEEE journal of selected topics in applied earth observations and remote sensing*, vol. 6, no. 1, pp. 217–223, 2012.

[127] C. Li, W. Huang, and S. Gleason, "Dual antenna space-based GNSS-R ocean surface mapping: Oil slick and tropical cyclone sensing," *IEEE Journal of Selected Topics in Applied Earth Observations and Remote Sensing*, vol. 8, no. 1, pp. 425–435, 2014.

[128] M. Unwin, S. Gao, R. De Vos Van Steenwijk, P. Jales, M. Maqsood, C. Gommenginger, J. Rose, C. Mitchell, and K. Partington, "Development of low-cost spaceborne multi-frequency GNSS receiver for navigation and GNSS remote sensing," *International Journal of Space Science and Engineering*, vol. 1, no. 1, pp. 20–50, 2013.

[129] S. Jin, Q. Wang, and G. Dardanelli, "A review on multi-GNSS for earth observation and emerging applications," *Remote Sensing*, vol. 14, no. 16, p. 3930, 2022.

[130] M. Unwin, P. Garner, L. Rose, R. D. V. V. Steenwijk, J. Rawlinson, T. Norris, N. Pierdicca, E. Cardellach, J. Peng, L. Guerriero, G. Foti, D. Robinson, E. Santi, P. Blunt, K. Rautiainen, J. P. Lejault, M. P. Clarizia, and M. Pastena, "ESA Hydrognss Scout GNSS-R Land Sensing Mission Preparation," in *IGARSS 2024 - 2024 IEEE International Geoscience and Remote Sensing Symposium*, 2024, pp. 6729–6731.

[131] F. Santi, F. Pieralice, and D. Pastina, "Multistatic GNSS-based passive radar for maritime surveillance with long integration times: Experimental results," in *2018 IEEE Radar Conference (RadarConf18)*. IEEE, 2018, pp. 1260–1265.

[132] F. Santi, D. Pastina, and M. Bucciarelli, "Maritime moving target detection technique for passive bistatic radar with GNSS transmitters," in *2017 18th International Radar Symposium (IRS)*. IEEE, 2017, pp. 1–10.

[133] H. Ma, M. Antoniou, A. G. Stove, J. Winkel, and M. Cherniakov, "Maritime moving target localization using passive GNSS-based multistatic radar," *IEEE Transactions on Geoscience and Remote Sensing*, vol. 56, no. 8, pp. 4808–4819, 2018.

[134] M. I. Skolnik, *Introduction to radar systems*. McGraw-hill New York, 1980, vol. 3.

[135] R. U. I. ZUO, "Bistatic Synthetic Aperture Radar using GNSS as Transmitters of Opportunity," 2011.

[136] V. Zavorotny and A. Voronovich, "GNSS-R modeling results obtained with improved bistatic radar equation," in *2018 International conference on electromagnetics in advanced applications (ICEAA)*. IEEE, 2018, pp. 35–38.

[137] R. D. De Roo and F. T. Ulaby, "Bistatic Specular Scattering from Rough Dielectric Surfaces," Tech. Rep. 2, 1994.

[138] E. Kaplan and C. Hegarty, *Understanding GPS: Principles and Applications*, ser. Artech House mobile communications series. Artech House, 2005.

[139] J. B.-Y. Tsui, *Fundamentals of global positioning system receivers: a software approach*. John Wiley & Sons, 2005.

[140] J. F. Marchan-Hernandez, A. Camps, N. Rodriguez-Alvarez, E. Valencia, X. Bosch-Lluis, and I. Ramos-Perez, "An Efficient Algorithm to the Simulation of Delay–Doppler Maps of Reflected Global Navigation Satellite System Signals," *IEEE Transactions on Geoscience and Remote Sensing*, vol. 47, no. 8, pp. 2733–2740, 2009.

[141] A. Camps, "Spatial resolution in GNSS-R under coherent scattering," *IEEE Geoscience and Remote Sensing Letters*, vol. 17, no. 1, pp. 32–36, 2019.

[142] E. Loria, A. O'Brien, and I. J. Gupta, "Detection & separation of coherent reflections in GNSS-R measurements using CYGNSS data," in *IGARSS 2018-2018 IEEE International Geoscience and Remote Sensing Symposium*. IEEE, 2018, pp. 3995–3998.

[143] H. Park, D. Pascual, A. Camps, F. Martin, A. Alonso-Arroyo, and H. Carreno-Luengo, "Analysis of spaceborne GNSS-R delay-Doppler tracking," *IEEE Journal of Selected Topics in Applied Earth Observations and Remote Sensing*, vol. 7, no. 5, pp. 1481–1492, 2014.

[144] Z. Dong and S. Jin, "Evaluation of the Land GNSS-Reflected DDM Coherence on Soil Moisture Estimation from CYGNSS Data," *Remote Sensing*, vol. 13, no. 4, p. 570, 2021.

[145] A. Alonso-Arroyo, A. Camps, A. Monerris, C. Rüdiger, J. P. Walker, R. Onrubia, J. Querol, H. Park, and D. Pascual, "On the Correlation Between GNSS-R Reflectivity and L-Band Microwave Radiometry," *IEEE Journal of Selected Topics in Applied Earth Observations and Remote Sensing*, vol. 9, no. 12, pp. 5862–5879, 2016.

[146] J. O. Winkel, "Modeling and simulating GNSS signal structures and receivers," *PhD manuscript*, 2000.

[147] J. Wu and Y. Hu, "The study on GPS signal acquisition algorithm in time domain," in *2008 4th International Conference on Wireless Communications, Networking and Mobile Computing*. IEEE, 2008, pp. 1–3.

[148] Y. Zheng, "A software-based frequency domain parallel acquisition algorithm for GPS signal," in *2010 International Conference on Anti-Counterfeiting, Security and Identification*. IEEE, 2010, pp. 298–301.

[149] W. Zhang, S. Ruan, Z. Dou, and J. Hu, "Application of FFT parallel code phase search algorithm in GNSS software," in *2016 IEEE 13th International Conference on Signal Processing (ICSP)*. IEEE, 2016, pp. 1165–1170.

[150] D. Borio, C. O'Driscoll, and G. Lachapelle, "Coherent, Noncoherent, and Differentially Coherent Combining Techniques for Acquisition of New Composite GNSS Signals," *IEEE Transactions on Aerospace and Electronic Systems*, vol. 45, no. 3, pp. 1227–1240, 2009.

[151] K. Mollaiyan, R. Santerre, and R. J. Landry, "Acquisition of Weak Signals in Multi-Constellation Frequency Domain Receivers," *Positioning*, vol. 04, no. 02, pp. 144–152, 2013.

[152] K. Borre, D. M. Akos, N. Bertelsen, P. Rinder, and S. H. Jensen, *A software-defined GPS and Galileo receiver: a single-frequency approach*. Springer Science & Business Media, 2007.

[153] S. H. Kong, "A deterministic compressed GNSS acquisition technique," *IEEE Transactions on Vehicular Technology*, vol. 62, no. 2, pp. 511–521, 2013.

[154] X. Li, A. Rueetschi, Y. C. Eldar, and A. Scaglione, "GPS signal acquisition via compressive multichannel sampling," *Physical Communication*, vol. 5, no. 2, pp. 173–184, 6 2012.

[155] L. R. Weill, "Theory and applications of signal compression in GNSS receivers," in *Proceedings of the 20th International Technical Meeting of the Satellite Division of The Institute of Navigation (ION GNSS 2007)*, 2007, pp. 708–719.

[156] J. C. Bermudez Ordonez, R. M. Arnaldo Valdes, and F. Gomez Comendador, "Energy efficient GNSS signal acquisition using singular value decomposition (SVD)," *Sensors*, vol. 18, no. 5, p. 1586, 2018.

[157] S.-H. Kong, "A Compressed Sensing Technique for GPS Signal Acquisition," in *Proceedings of the 2012 International Technical Meeting of The Institute of Navigation*, 2012, pp. 356–361.

[158] A. Draganic, I. Orovic, and S. Stankovic, "On some common compressive sensing recovery algorithms and applications," *Facta universitatis - series: Electronics and Energetics*, vol. 30, no. 4, pp. 477–510, 7 2017.

[159] L. Jacques, "A short note on compressed sensing with partially known signal support," *Signal Processing*, vol. 90, no. 12, pp. 3308–3312, 2010.

[160] B. Ansari, V. Kaushik, and S. K. Biswas, "Raw GNSS Data Compression using Compressive Sensing for Reflectometry Applications," in *2020 XXXIIIrd General Assembly and Scientific Symposium of the International Union of Radio Science*. IEEE, 2020, pp. 1–4.

[161] J. S. Löfgren and R. Haas, "Sea level measurements using multi-frequency GPS and GLONASS observations," *EURASIP Journal on Advances in Signal Processing*, vol. 2014, no. 1, p. 50, 2014.

[162] W. Ji, C. Xiu, W. Li, and L. Wang, "Ocean surface target detection and positioning using the spaceborne GNSS-R delay-Doppler maps," in *2014 IEEE Geoscience and Remote Sensing Symposium*. IEEE, 2014, pp. 3806–3809.

[163] B. Ansari, D. Kundu, and S. K. Biswas, "A multi-frequency GPS and NavIC reflectometry receiver using commercially off-the-shelf SDR," *GPS Solutions*, vol. 29, no. 1, p. 29, 2024. [Online]. Available: https://doi.org/10.1007/s10291-024-01783-8

[164] B. Ansari and S. K. Biswas, "Multi-Frequency GNSS-R Receiver using BladeRF SDR and Single-Board Computer," in *2024 4th URSI Atlantic Radio Science Meeting (AT-RASC)*, 2024, pp. 1–4.

[165] ——, "A Hardware-In-Loop simulation Test-bed for NavIC Reflectometry Experiments," in *2021 XXXIVth General Assembly and Scientific Symposium of the International Union of Radio Science (URSI GASS)*, 2021, pp. 1–3.

[166] X. Ma, C. Tang, and X. Wang, "The evaluation of IRNSS/NavIC system's performance in its primary and secondary service areas–data quality, usability and single point positioning," *Acta Geodaetica et Geophysica*, vol. 54, pp. 55–70, 2019.

[167] A. Santra, S. Mahato, S. Dan, and A. Bose, "Precision of satellite based navigation position solution: a review using NavIC data," *Journal of Information and Optimization Sciences*, vol. 40, no. 8, pp. 1683–1691, 2019.

[168] X. Meng, F. Gao, T. Xu, Y. He, N. Wang, and B. Ning, "Design of real-time GNSS-R software-defined receiver for coastal altimetry using GPS/BDS/QZSS signals," *GPS Solutions*, vol. 28, no. 1, p. 20, 2024.

[169] N. Wang, K. He, F. Gao, T. Chu, J. Hou, and T. Xu, "Analysis of GNSS-R Code-Level Altimetry using QZSS C/A, L1C, and BDS B1C signals and their Combinations in a Coastal Experiment," *IEEE Journal of Selected Topics in Applied Earth Observations and Remote Sensing*, vol. 16, pp. 4549–4564, 2023.

[170] N. Rodríguez Álvarez, "Contributions to earth observation using gnss-r opportunity signals," 2011.

[171] S. Jin, A. Camps, Y. Jia, F. Wang, M. Martin-Neira, F. Huang, Q. Yan, S. Zhang, Z. Li, and K. Edokossi, "Remote sensing and its applications using GNSS reflected signals: advances and prospects," *Satellite Navigation*, vol. 5, no. 1, p. 19, 2024.

[172] Y. Jia, P. Savi, D. Canone, and R. Notarpietro, "Estimation of Surface Characteristics Using GNSS LH-Reflected Signals: Land Versus Water," *IEEE Journal of Selected Topics in Applied Earth Observations and Remote Sensing*, vol. 9, no. 10, pp. 4752–4758, 10 2016.

[173] N. Pierdicca, L. Guerriero, M. Brogioni, and A. Egido, "On the coherent and non coherent components of bare and vegetated terrain bistatic scattering: Modelling the GNSS-R signal over land," in *International Geoscience and Remote Sensing Symposium (IGARSS)*, 2012.

[174] F. Gao, T. Xu, N. Wang, C. Jiang, Y. Du, W. Nie, and G. Xu, "Spatiotemporal evaluation of GNSS-R based on future fully operational global multi-GNSS and eight-LEO constellations," *Remote sensing*, vol. 10, no. 1, p. 67, 2018.

[175] J.-C. Juang, S.-H. Ma, and C.-T. Lin, "Study of GNSS-R techniques for FORMOSAT mission," *IEEE Journal of Selected Topics in Applied Earth Observations and Remote Sensing*, vol. 9, no. 10, pp. 4582–4592, 2016.

[176] P. Jales, S. Esterhuizen, D. Masters, V. Nguyen, O. N. Correig, T. Yuasa, and J. Cartwright, "The new Spire GNSS-R satellite missions and products," in *Image and signal processing for remote sensing XXVI*, vol. 11533. SPIE, 2020, p. 1153316.

[177] S. Talebi, "Design, development and verification of a UAV-based GNSS payload for reflectometry," 2024.

[178] S. Ugazio, M. T. Gamba, Y. Pei, G. Marucco, P. Savi, and L. L. Presti, "GPS-Reflectometry prototype for UAVs and in flight data error analysis," in *Proceedings of the 28th International Technical Meeting of the Satellite Division of The Institute of Navigation (ION GNSS+ 2015)*, 2015, pp. 3945–3952.

[179] C. Jing, X. Niu, C. Duan, F. Lu, G. Di, and X. Yang, "Sea surface wind speed retrieval from the first Chinese GNSS-R mission: Technique and preliminary results," *Remote Sensing*, vol. 11, no. 24, p. 3013, 2019.

[180] W. Wan, B. Liu, Z. Guo, F. Lu, X. Niu, H. Li, R. Ji, J. Cheng, W. Li, and X. Chen, "Initial evaluation of the first Chinese GNSS-R mission BuFeng-1 A/B for soil moisture estimation," *IEEE Geoscience and Remote Sensing Letters*, vol. 19, pp. 1–5, 2021.

[181] C. Chew, A. Colliander, R. Shah, C. Zuffada, and M. Burgin, "The sensitivity of ground-reflected GNSS signals to near-surface soil moisture, as recorded by spaceborne receivers," in *2017 IEEE International Geoscience and Remote Sensing Symposium (IGARSS)*. IEEE, 2017, pp. 2661–2663.

[182] M. Asgarimehr, C. Arnold, T. Weigel, C. Ruf, and J. Wickert, "GNSS reflectometry global ocean wind speed using deep learning: Development and assessment of CyGNSSnet," *Remote Sensing of Environment*, vol. 269, p. 112801, 2022.

[183] P. T. Setti and S. Tabibi, "Comprehensive Analysis of CYGNSS GNSS-R data for Enhanced Soil Moisture Retrieval," *IEEE Journal of Selected Topics in Applied Earth Observations and Remote Sensing*, 2024.

[184] Y. Pei, R. Notarpietro, P. Savi, and M. Pini, "A fully software GNSS-R receiver for soil dielectric constant monitoring," in *Proceedings of the 2013 International Conference on Electromagnetics in Advanced Applications, ICEAA 2013*, 2013, pp. 1228–1231.

[185] L. Guerriero, F. Martín, A. Mollfulleda, S. Paloscia, N. Pierdicca, E. Santi, and N. Floury, "Ground-Based Remote Sensing of Forests Exploiting GNSS Signals," *IEEE Transactions on Geoscience and Remote Sensing*, vol. 58, no. 10, pp. 6844–6860, 10 2020.

[186] K. Yu, S. Wang, Y. Li, X. Chang, and J. Li, "Snow depth estimation with GNSS-R dual receiver observation," *Remote Sensing*, vol. 11, no. 17, p. 2056, 2019.

[187] W. Wan, L. Zhao, J. Zhang, H. Liang, Z. Guo, B. Liu, and R. Ji, "Toward terrain effects on GNSS interferometric reflectometry snow depth retrievals: Geometries, modeling, and applications," *IEEE Transactions on Geoscience and Remote Sensing*, vol. 60, pp. 1–14, 2022.

[188] H. Park, A. Camps, D. Pascual, Y. Kang, R. Onrubia, J. Querol, and A. Alonso-Arroyo, "A Generic Level 1 Simulator for Spaceborne GNSS-R Missions and Application to GEROS-ISS Ocean Reflectometry," *IEEE Journal of Selected Topics in Applied Earth Observations and Remote Sensing*, vol. 10, no. 10, pp. 4645–4659, 10 2017.

[189] C. S. Ruf, C. Chew, T. Lang, M. G. Morris, K. Nave, A. Ridley, and R. Balasubramaniam, "A New Paradigm in Earth Environmental Monitoring with the CYGNSS Small Satellite Constellation," *Scientific Reports*, vol. 8, no. 1, 12 2018.

[190] H. Carreno-Luengo, A. Camps, P. Via, J. F. Munoz, A. Cortiella, D. Vidal, J. Jané, N. Catarino, M. Hagenfeldt, and P. Palomo, "3Cat-2—An experimental nanosatellite for GNSS-R earth observation: Mission concept and analysis," *IEEE Journal of Selected Topics in Applied Earth Observations and Remote Sensing*, vol. 9, no. 10, pp. 4540–4551, 2016.

[191] C. Ruf, R. Backhus, T. Butler, C.-C. Chen, S. Gleason, E. Loria, D. McKague, R. Miller, A. O'Brien, and L. van Nieuwstadt, "Next generation GNSS-R instrument," in *IGARSS 2020-2020 IEEE International Geoscience and Remote Sensing Symposium*. IEEE, 2020, pp. 3353–3356.

[192] H. Carreno-Luengo, A. Camps, I. Ramos-Perez, and A. Rius, "Experimental evaluation of GNSS-reflectometry altimetric precision using the P (Y) and C/A signals," *IEEE Journal of Selected Topics in Applied Earth Observations and Remote Sensing*, vol. 7, no. 5, pp. 1493–1500, 2014.

[193] A. Alonso-Arroyo, S. Torrecilla, J. Querol, A. Camps, D. Pascual, H. Park, and R. Onrubia, "Two dedicated soil moisture experiments using the scatterometric properties of GNSS-reflectometry," in *2015 IEEE International Geoscience and Remote Sensing Symposium (IGARSS)*, 2015, pp. 3921–3924.

[194] A. Perez-Portero, J. F. Munoz-Martin, H. Park, and A. Camps, "Airborne gnss-r: A key enabling technology for environmental monitoring," *IEEE Journal of Selected Topics in Applied Earth Observations and Remote Sensing*, vol. 14, pp. 6652–6661, 2021.

[195] S. Shekhar, R. Prakash, D. K. Pandey, A. Vidyarthi, S. Tyagi, D. Putrevu, and A. Misra, "Development of Soil Moisture Inversion Model for Bare Soil Using Navigation With Indian Constellation (NavIC)," *IEEE Geoscience and Remote Sensing Letters*, pp. 1–5, 2021.

[196] Y. Zhu, J. Wickert, T. Tao, K. Yu, Z. Li, X. Qu, Z. Ye, J. Geng, J. Zou, and M. Semmling, "Sensing Sea Ice Based on Doppler Spread Analysis of Spaceborne GNSS-R Data," *IEEE Journal of Selected Topics in Applied Earth Observations and Remote Sensing*, vol. 13, pp. 217–226, 2020.

[197] S. Jin and A. Komjathy, "GNSS reflectometry and remote sensing: New objectives and results," *Advances in Space Research*, vol. 46, no. 2, pp. 111–117, 2010.

[198] F. Huang, J. Xia, C. Yin, X. Zhai, G. Yang, W. Bai, Y. Sun, Q. Du, X. Wang, and T. Qiu, "Spaceborne GNSS reflectometry with Galileo signals on FY-3E/GNOS-II: measurements, calibration, and wind speed retrieval," *IEEE Geoscience and Remote Sensing Letters*, vol. 20, pp. 1–5, 2023.

[199] L. I. Weiqiang, E. Cardellach, R. Serni, R. Antonio, and Z. Bo, "First spaceborne demonstration of BeiDou-3 signals for GNSS reflectometry from CYGNSS constellation," *Chinese Journal of Aeronautics*, vol. 34, no. 9, pp. 1–10, 2021.

[200] V. Chamoli, R. Prakash, A. Vidyarthi, and A. Ray, "Sensitivity of NavIC signal for soil moisture variation," in *2017 International Conference on Emerging Trends in Computing and Communication Technologies (ICETCCT)*, 2017, pp. 1–4.

[201] H. Park, A. Camps, J. Castellvi, M. Vall-llossera, G. Portal, and L. Rossato, "Sensitivity to Soil Moisture and Observation Geometry of Spaceborne GNSS-R Delay-Doppler Maps," in *IGARSS 2019 - 2019 IEEE International Geoscience and Remote Sensing Symposium*, 2019, pp. 8358–8361.

[202] A. Egido Egido, "GNSS reflectometry for land remote sensing applications," Ph.D. dissertation, 2013.

[203] S. ISRO, "Indian Regional Navigation Satellite System: Signal in Space ICD for Standard Positioning Service," 2014.

[204] X. Wang, S. Zhang, L. Wang, X. He, and Q. Zhang, "Analysis and combination of multi-GNSS snow depth retrievals in multipath reflectometry," *GPS Solutions*, vol. 24, no. 3, 7 2020.

[205] R. Xu, J. Y. Li, J. J. Yang, K. Wei, and Y. X. Qi, "A design of u-shaped slot antenna with broadband dual circularly polarized radiation," *IEEE Transactions on Antennas and Propagation*, vol. 65, no. 6, pp. 3217–3220, 2017.

[206] S. W. Arif, A. Coskun, and I. Kale, "Multi-Stage Complex Notch Filtering for Interference Detection and Mitigation to Improve the Acquisition Performance of GPS," in *PRIME 2018 - 14th Conference on Ph.D. Research in Microelectronics and Electronics*. Institute of Electrical and Electronics Engineers Inc., 8 2018, pp. 165–168.